DISSERTATION

TRANSIENT ABSORPTION IMAGING OF HEMEPROTEIN IN FRESH MUSCLE FIBERS

Submitted by

Erkang Wang

Department of Electrical and Computer Engineering

In partial fulfillment of the requirements

For the Degree of Doctor of Philosophy

Colorado State University

Fort Collins, Colorado

Summer 2022

Doctoral Committee:

Advisor: Jesse Wilson

Randy Bartels
Diego Krapf
Stuart Tobet

ABSTRACT

TRANSIENT ABSORPTION IMAGING OF HEMEPROTEIN IN FRESH MUSCLE FIBERS

Mitochondrial diseases affect 1 in 4000 individuals in the U.S. among adults and children of all races and genders. Nevertheless, these diseases are hard to diagnose because they affect each person differently. Meanwhile the gold standard diagnosis methods are usually invasive and time-consuming. Therefore, a non-invasive and in-vivo diagnosis method is highly demanded in this area. Our goal is to develop a non-invasive diagnosis method based on the endogenous nonlinear optical effect of the live tissues.

Mitochondrial disease is frequently the result of a defective electron transport chain (ETC). Our goal is to develop a non-invasive way to measure redox within the ETC, specifically, of cytochromes. Cytochromes are iron porphyrins that are essential to the ETC. Their redox states can indicate cellular oxygen consumption and mitochondrial ATP production. So being able to differentiate the redox states of cytochromes will offer us a method to characterize mitochondrial function. Meanwhile, Chergui's group found out that the two redox states of cytochrome *c* have different pump-probe spectroscopic responses, meaning that the transient absorption (TA) decay lifetime can be a potential molecular contrast for cytochrome redox state discrimination. Their research leads us to utilize the pump-probe spectroscopic idea to develop a time-resolved optical microscopic method to differentiate not only cytochromes from other chemical compounds but also reduced cytochromes from oxidized ones. This dissertation describes groundbreaking experiments where transient absorption is used to reveal excited-state lifetime differences between

healthy controls and an animal model of mitochondrial disease, in addition to differences between reduced and oxidized ETC in isolated mitochondria and fresh preparations of muscle fibers.

For our initial experiments, we built a pump-probe microscopic system with a fiber laser source, producing 530nm pump and 490nm probe using a 3.5kHz laser scanning rate. The pulse durations of pump and probe are both 800fs. For the preliminary results, we have successfully achieved TA decay contrast between reduced and oxidized cytochromes in solution form. Then we have achieved SNR enhanced pump-probe image of BGO crystal particles with the help of the software-based adaptive filter noise canceling method. We also have installed a FPGA-based adaptive filter to enhance the pump-probe signals of the electrophoresis gels that contain different mitochondrial respiratory chain supercomplexes.

However, because the noise floor was still 30 dB higher than shot noise limit, cytochrome imaging in live tissues was still problematic. We then built another pump-probe microscope with a solid-state ultrafast laser source. In that way, we do not need to worry about laser relative intensity noise (RIN) anymore, since the noise floor of the solid-state laser source can reach the shot noise limit at MHz region. One other advantage of the new laser source is that it can provide one tunable laser output that can be directly converted to the probe pulse with tunable center wavelength. Its tunability can cover the entire visible spectrum. We realized a pump-probe microscopy with a 520nm pump pulse and a tunable probe pulse. The tunability on the probe arm allows us to explore better pump-probe contrast between two redox states.

What's more, I will introduce my preliminary results of utilizing supercontinuum generation in a photonic crystal fiber (PCF) to realize tunability on pump wavelength. In that way, more possibilities will be unlocked. And the hyperspectral pump-probe microscope will be able to distinguish more molecules.

TABLE OF CONTENTS

LIST OF FIGURES

Chapter 1. Introduction

1.1 Overview of transient absorption microscopy

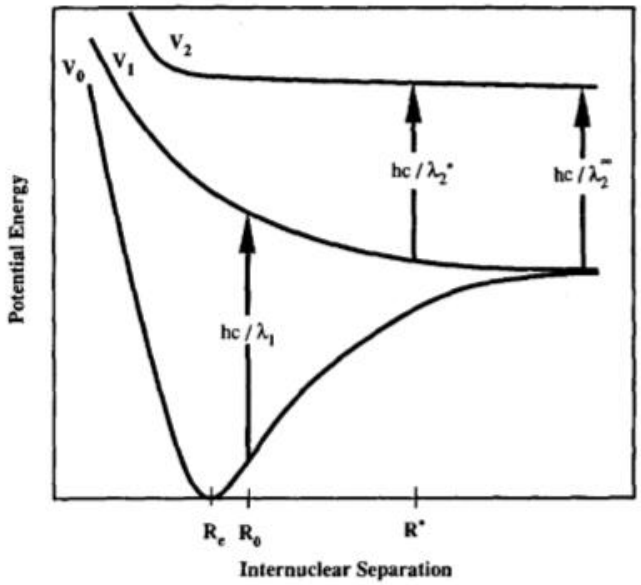

Figure 1.1: Transient absorption illustrative figure. At time zero, two nucleus starts to separate after absorbing the pump photon with wavelength of λ_1. The excited state energy level changes accordingly over time which lead to absorbance change of probe photon with wavelength of λ_2.[1].

Transient absorption microscopy (TAM) is an imaging modality that can trace the relaxation of optically-excited states in molecules. In absorptive (non-fluorescent) pigments, these excited states decay very rapidly, on the order of a few picoseconds. Therefore, a microscopic technique with fs or sub-picosecond time resolution is required to record such dynamics in real-time. As the state of a molecule evolves over the course of femtoseconds and picosecond, so does its optical absorption spectrum. However, directly observing these short-lived excited states with electronic photodetectors like PMTs or photodiodes, which typically have slow ~nanosecond response times, is impossible. TAM overcomes the temporal resolution problem. It utilizes the ultrafast pump laser

pulse to place the molecules in an excited state, followed by a probe pulse, that arrives several picoseconds after the pump pulse, to detect the evolving transient molecular states.

The pump-probe arrival time difference or the pump-probe time delay can be accurately controlled by varying the pump's optical path length (OPL) through a mechanical translation stage. One hundred fs time difference is equivalent to 0.3 μm pump-probe OPL difference. easily controlled by a motorized delay stage. A pump-dependent perturbation to probe transmissivity can be detected as long as the pump-probe delay is less than the relaxation time of the excited state.

1.2 The evolution of ultrafast laser

The laser pulse duration limits transient absorption's ability to observe the intermediate, short-lived excited states. It determines the fastest transient states we can resolve throughout the entire molecular relaxation process. Since the invention of the first Q-switched nanosecond laser in 1960[2,3], scientists have developed better pulse generation methods. From these efforts, Q-switching and modelocking are the primary techniques that generate short pulses. A Q-switch increases the laser cavity loss to allow for a buildup of population inversion, which results in a short, intense burst of stimulated emission when the Q-switch is shut off. Q-switching can only generate nanosecond pulses. It is limited by the fact that the pulse width of a Q-switching laser is proportional to the cavity transit round trip time, as well as the initial, final and threshold population inversion densities (Chapter 8, equation 8.7 in ref[4]). To generate shorter, ps or fs pulses requires a more recent technique known as mode-locking. Whereas Q-switching increases cavity losses to build up a large population inversion, resulting in a burst of amplification when the cavity is switched back to a low-loss configuration, modelocking synchronizes the phase of longitudinal modes (of different wavelengths) so that constructive interference between these modes results in a short pulse.

Modelocking mechanisms can be classified into either active or passive mechanisms[5]. Active modelocking makes use of an electronically-driven modulator (electro-optic or acousto-optic) to periodically modulate cavity losses. Shorter pulse duration requires a faster loss modulation[6]. However, the loss modulation speed provided by an electronic signal is not fast enough to produce sub-ps or fs laser pulses. The pulse widths of an active modelocking laser are on the order of 10-20ps (Chapter 9 in ref [4]). On the other hand, passive modelocking, in which the cavity loss is modulated by the intensity of the laser pulse itself [7], can generate laser pulses as short as several fs, reaching even a regime where the pulse consists of one or two cycles of the optical frequency[8]. Passive modelocking works by making intra-cavity losses lower at high intensity, thus favoring the buildup of short duration pulses.

From Figure 1.2, we can see the development of mode-locking techniques leading to shorter laser pulse durations.

Figure 1.2: Ultrafast laser pulse duration decreases with Mode-locking technique development.

In 1970, D.J.Kuizenga and A.E.Siegman published a complete theoretical analysis of active mode-locking and also experimentally proved that 40ps pulse duration can be achieved by using a periodically-driven LiNbO3 phase modulator [9,10].

Almost at the same time, Ippen and his colleagues implemented passive modelocking using a dye saturable absorber (SA), producing 1.5ps laser pulses. However, the slow recovery time and high loss of the dye SA led to instabilities arising spontaneous emission known as Q-switching instability [5,11,12].The problem persisted until 1991 when Sibbett group discovered Kerr-lens modelocking (KLM)[13–16]. KLM generates stable laser pulses with durations as short as a few fs. Unlike the slow dye SA, the Kerr effect is instantaneous and independent of wavelength. KLM works by forming an intensity-dependent graded-index lens in the laser gain medium. On one resonator mirror, KLM makes high intensity portion of a laser to have a smaller beam waist than lower intensity portion. Therefore, closing an aperture can reject the low intensity mode and the high intensity portion is selectively built up in the cavity. Figure 1.3 shows a KLM laser cavity layout. The two focusing lenses usually have the same focal length, but the distance between the two lenses must be carefully adjusted to maximize sensitivity to the Kerr effect. The Kerr medium with length of l is right in the center of the resonator. A hard aperture right in front of M_1 is used to reject lower intensity CW laser, so that only high peak intensity pulses laser can build up in the laser cavity.

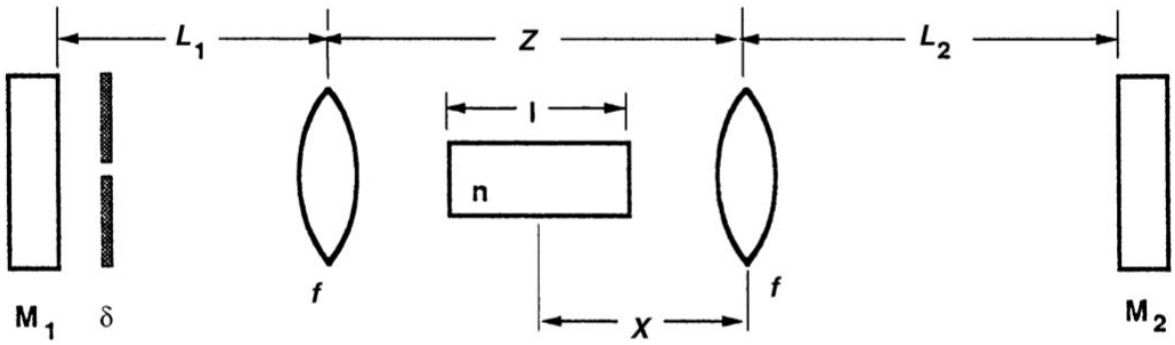

Figure 1.3: Equivalent resonator of Kerr lens mode locking laser. nonlinear gain material length is l. δ is a circular aperture that can select the most intensive beam center to propagate inside the resonator. M1 and M2 are mirrors. [4]

Sensitivity s is one crucial parameter for KLM laser design. The parameter s describes the spot size variation of the laser beam at the aperture with respect to the intracavity power, and thus the

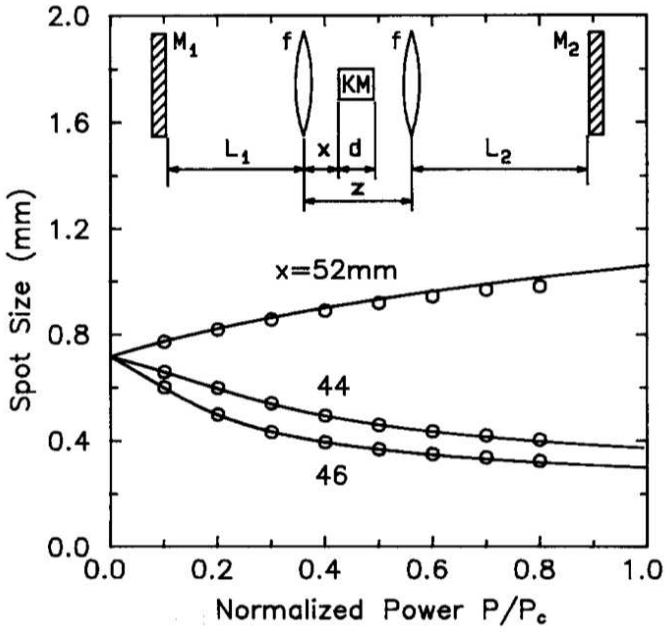

Figure 1.4. Spot size on mirror M1 VS normalized laser power inside a laser resonator with nonlinear Kerr medium. x is the kerr medium position relative to the first lens. The resonator parameters are: L_1 = 700 mm, L_2= 900 mm, f= 50 ram, z= 107.1 mm, and d=10 mm; KM is the Kerr medium. Figure credit: [18]

aperture's ability to select for high-intensity pulses. One can discover the relationship between the spot size at the aperture and laser power by treating the Kerr medium as a thin, intensity-dependent lens with focal length $f = \frac{w^2}{4\gamma I_0 l}$, sandwiched between two linear slabs [4,17,18]. As shown in Fig. 1.4, the sensitivity is highly dependent on placement of the Kerr medium (KM) [4,17,18]. When the distance between the lens and Kerr medium, x is 52mm, the spot size at M_1 increases with power, but when x is 44 or 46 mm, the spot size decreases with laser power. This trend makes it possible to reject the low-power beam and select for high-intensity pulses by closing down an aperture at M_1[18].

The sensitivity, s, of beam spot size to the cavity geometry can be quantified from the ABCD matrix calculation,

$$|s|_{max} = \frac{1}{\sqrt[4]{g_1 g_2 (1 - g_1 g_2)}}$$

Where $g_1$and g_2 are functions of x.

$$g_1 = 1 - \frac{z - \left(x + \frac{d}{2}\right)}{f_{kerr}} - \frac{L_0}{f}$$

$$g_1 = 1 - \frac{\left(x + \frac{d}{2}\right)}{f_{kerr}} - \frac{L_0}{f}$$

Where $f_{kerr} = \frac{w^2}{4\gamma I_0 l}$ and $L_o = z - \frac{\left(x+\frac{d}{2}\right)[z-\left(x+\frac{d}{2}\right)]}{f_{kerr}}$. The product of the two also sets the laser resonator stability criterion: $0 < g_1\, g_2 < 1$. In other words, $g_1$and g_2 not only set the maximum sensitivity but also determine the laser resonator stable operation region. It turns out the maximum s is achieved when $g_1 g_2 = 0$ and $L_1 = L_2$, which means the laser resonator is set to the confocal configuration. For this configuration, 0.6mm tolerance along the z direction must be satisfied for stable operation[4]. The requirement reveals one of the major drawbacks of the KLM, it restricts to a very careful cavity designs and alignment. One other drawback is that KLM, while frequently used to generate femtosecond pulses, is not that stable when generating picosecond pulses because, in the picosecond regime, the Kerr lens effect tends to be weak.

To overcome these drawbacks, semiconductor saturable absorber mirror (SESAM) modelocking that generates 3 ps pulses was discovered in 1990s[19,20]. The SESAM mode-locking requires developments on both semiconductor technology and solid-state laser physics. The accuracy of the semiconductor deposition technology greatly enhances the solid-state laser performance in terms of repetition rates, pulse duration and pulse peak intensity. More precisely, sub-nm control on

semiconductor layer thickness allows the accurate control of recovery time, saturation intensity and working spectral range. What's more, SESAMs can be inexpensively mass-produced with existing silicon fabrication processes.

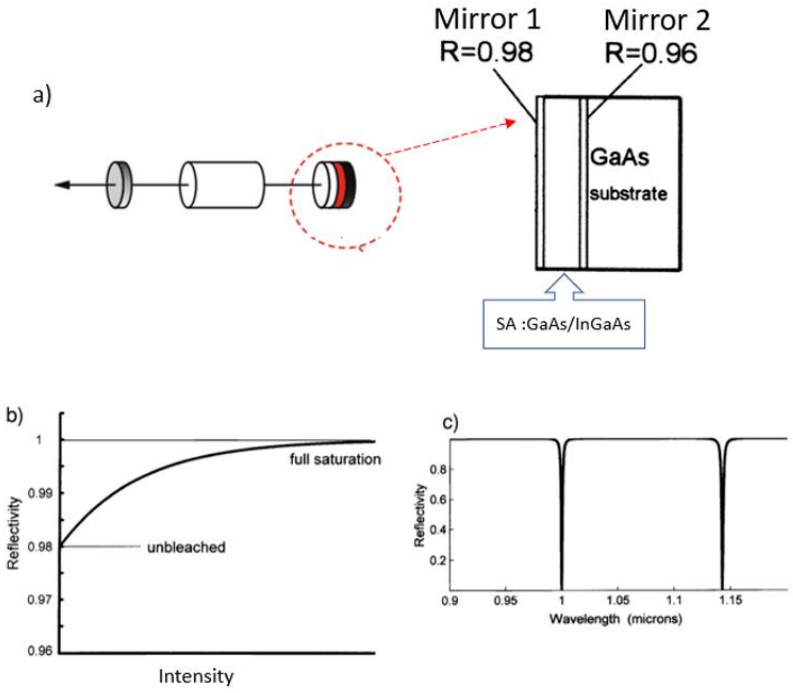

Figure 1.5: Schematic of SESAM laser. a)A laser resonator cavity with a intracavity GaAs/InGaAs saturable absorber (SA). The two mirrors on the SA forms a Fabry-Perot interferometer. [19,20], b) The reflectivity of SA varies with laser intensity in the cavity. The reflectivity tuning range is between 0.98 and 1. [6] c) The free spectral range is >100nm. The free spectral range describes the working wavelength rage of the SA. The >100nm rang is in excess of Nd:YLF gain bandwidth (~0.7nm). [4]

I will use an example device below to describe the SESAM principle. The arrangement of SESAM mode-locking laser is very simple, shown in Fig.1.5. The arrangement is very similar to a conventional laser resonant cavity. The only difference is that one end mirror is substituted by a SESAM device.

The device consists of a reflective coating[4] (R1=0.98), SA (50 layers), another reflective coating (R2=0.96) and a GaAs substrate. The structure forms a Fabry-Perot interferometer of 4 μm thickness. The thickness is chosen to use the interferometer in the antiresonant condition. It is

crucial to make the Fabry-Perot to operate at the antiresonance condition so that the intensity inside the device is lower than the incident intensity. Thereby higher damage threshold can be realized. The 'antiresonant' and 'resonant' is identified by whether the optical distance between two reflective coatings to be the integer or half-integer numbers of half-wavelengths. The condition for antiresonant operation is:

$$nd = m\frac{\lambda}{2}$$

Where nd is the optical thickness of the Fabry-Perot structure, which is 4 μm for the example design. When $m = 8$, reflectivity is at a minimum is 1 μm, shown in Fig. 1.5(c). The antiresonant condition is met when operating, rather, at a reflectivity maximum, e.g. 1.05 μm.. So this example is designed for mode-locking 1047nm output from a Nd:YLF laser. From Fig. 1.5 (c) we can clearly see that the free spectral range is >100nm which is in excess of Nd:YLF gain bandwidth (~0.7nm). Figure. 1.5 (b) shows the SESAM saturation response with respect to intracavity intensity. When the laser intensity is below the saturation intensity, the SESAM reflectivity is 0.98 which is just the top mirror reflectivity, resulting in cavity loss larger than the gain and population inversion buildup inside the gain medium. When the laser intensity is above the saturation intensity, the semiconductor SA sandwiched mirror 1 and 2 has the maximum reflectivity which makes the cavity loss is below the laser gain and rapid stimulated emission starts.

My research utilizes both solid-state and fiber-based lasers, so I will also give a brief introduction about the femtosecond fiber lasers. Fiber-based lasers, are prominent light source for portable microscope and optical devices, owing to their low-cost, compact size and permanent alignment. However, their relative intensity noise (RIN) is over 20 dB higher than that for solid state lasers, which is the major stumbling block for biological imaging.

The specific fiber-based laser we are using is called all-normal-dispersion (ANDi) femtosecond fiber laser. It utilizes nonlinear polarization evolution (NPE) as its modelocking mechanism. Briefly speaking, NPE achieves passive modelocking based on intensity-dependent polarization rotation. A typical ANDi schematic is shown in Figure.1.6. In this particular example, the ANDi consist of a 7 m length of single mode fiber (SMF), 20 cm of Yb-doped gain fiber, a 1 m SMF, and a free-space segment consisting of an NPE port and a birefringent plate working as a spectral filter. The grey shaded arrows and ovals represent linear and elliptical polarization states respectively. The magnitudes represent the corresponding light intensities. The NPE port has two quarter wave plates (QWP), one half wave plate (HWP) and one polarization beam splitter (PBS). The first QWP (QWP1) converts the input beam polarization state from linear to elliptical so that the Kerr effect inside the SMF and Yb fiber can rotate the orientation of the elliptically polarized light. The rotation strength is proportional to the intensity. So the light exiting the 2^{nd} collimator will have a heavily rotated state for intense component and a slightly rotated state for weaker component. The HWP and QWP2 adjust the polarization state to make sure the polarization state for lower intensity to be rejected and the polarization state for the high intensity to be transmitted by the PBS.

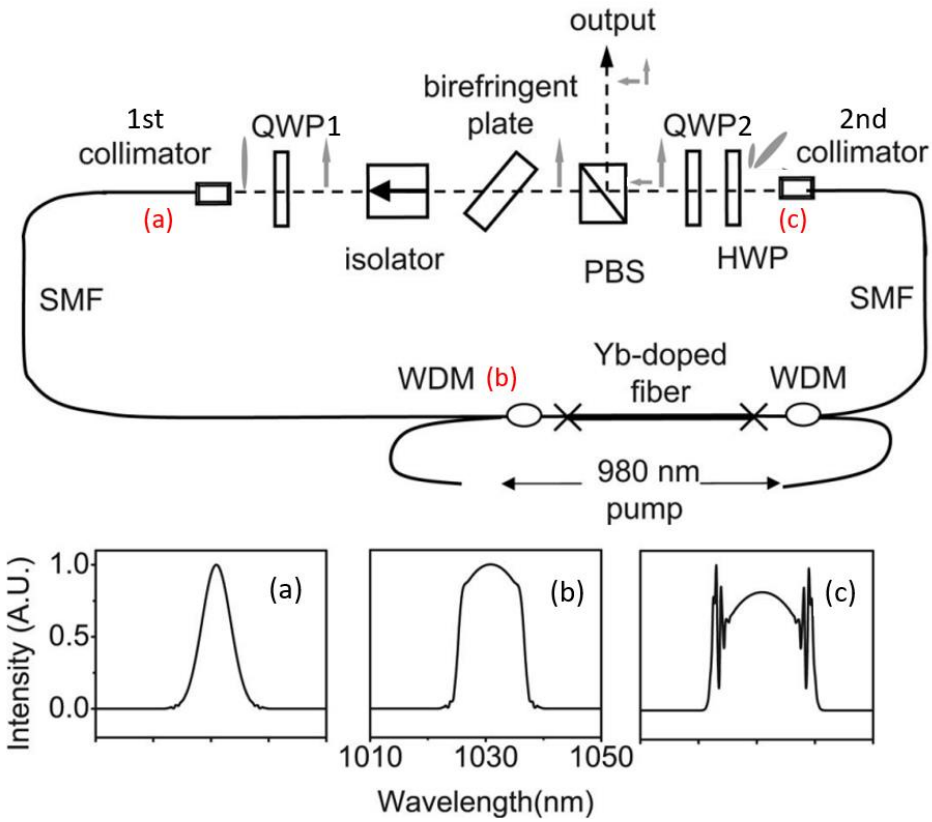

Figure 1.6: Schematic of ANDi laser. [21,22]QWP1 change the linear polarized beam to elliptical polarized. After the fiber Kerr effect rotating the polarization states, the intensive pulse portion rotates more than the less intensive portion at the input facet of HWP. Then HWP and QWP2 adjust the polarization angles and change elliptical back to linear polarization. The intensive portion meets the transmissive polarization state of the PBS and then keeps on propagating inside the cavity. The less intensive portion gets rejected by the PBS and become the output pulse which will recompressed by a out-of-cavity pulse compressor. The inset(a) (b) and (c) are pulse spectra measured at position (a) (b) and (c) marked in the upper panel. QWP: quarter-waveplate; HWP: half-waveplate; PBS: polarizing beam splitter; WDM: wavelength-division multiplexer; SMF: single mode fiber.

The inset Figure 1.6 (a), (b) and (c) represent the pulse spectra corresponding to that at the 1st collimator, gain fiber entrance and the 2nd collimator marked as (a), (b) and (c) respectively in the main laser schematic. The normal dispersion of the 1st segment of SMF adds quadratic spectral phase (linear chirp), elongating the pulse duration and changing the spectrum shape slowly from a pure Gaussian shape to a bell shape shown in Figure 1.6 (b). Then the gain medium fiber introduces a strong self-phase modulation (SPM) to the bell shaped spectrum that makes it develop the steep

and structured edges shown in Fig. 1.6 (c). The spectral edges always have lower intense wavelength components due to the destructive interference between newly generated frequency components.Meanwhile the spectral center usually has high intensity components because those experience less dispersion compared to the spectral edge components. Lastly, the NPE and the birefringent plate together reject the low-intensity components at the spectral edge and a small portion of spectral center as the laser output. Meanwhile most of the high intensity spectral center components re-circulate inside laser. The combined effect of NPE and birifringent plate ensures that the input pulse at collimator 1 always has a constant spectrum and polarization state after each round trip.

1.3 The evolution of transient absorption spectroscopy and microscopy

The most prominent personage in the transient absorption research field is the femtochemist Ahmed Hassan Zewail. He and his colleagues combined pump-probe techniques with the concept of molecular wavepackets to study the breaking and forming of chemical bonds at picosecond and femtosecond timescales This approach addresses the varying complexity of molecular systems from diatomic to protein and DNA.

Initially pump-probe techniques were widely used for spectroscopy. Consider for example, Zewail's experiments on the carbon-iodine photodissociation process[1] shown in Fig. 1.7. The

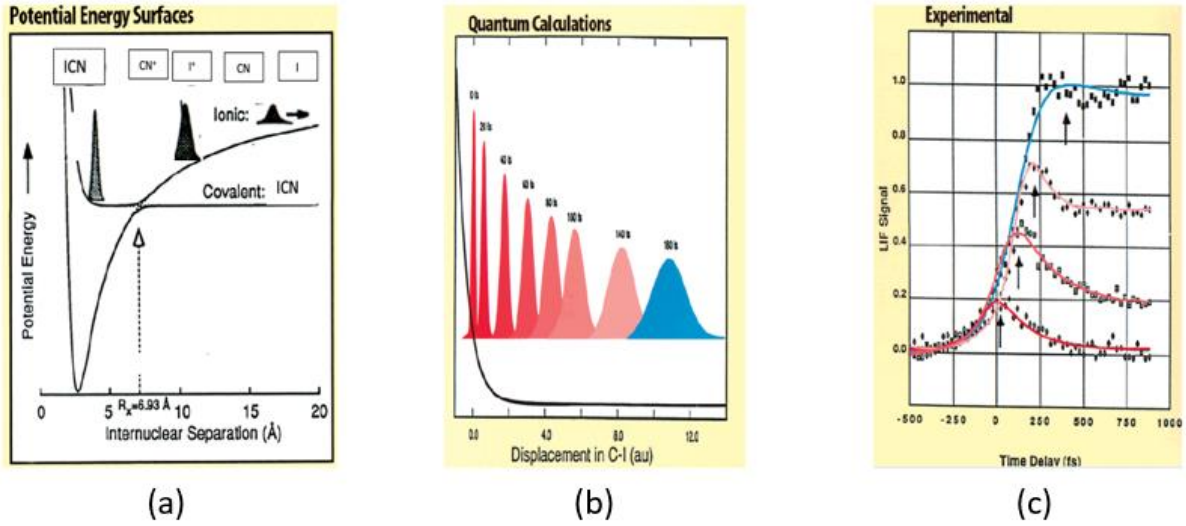

Figure 1.7: Femtochemistry of ICN reaction. (a) After the pump pulse breaks the I and CN bond, two nuclei start to separate over time. The system's energy level starts to change accordingly. (b) Wave packet that indicates the electron occupancy evolves over time. (c) Pump-probe spectroscopic measurements using four different probe wavelengths. It detects the time that required to break the I and CN bond. [23]

initial ultrafast pump pulse sets up a wave packet, consisting of a coherent superposition of vibrational wavefunctions. The concept of wave packet is conceptually similar to optical interference, which results from the superposition of a series of sinusoidal electric fields. In-phase superposition leads to constructive interference, whereas out of phase leads to destructive interference. Given the energy and boundary conditions that satisfy a specific potential well, (anharmonic potential well was used in Zewail's explanation), adding up all the waves results in constructive interference that peaks at a specific nuclear separation *R*. The initial wave packet can also be regarded as a nonstationary (nonequilibrium) state of a given nuclear structure and from there the system starts to evolve in time and the wave packet evolves accordingly. This evolving wave packet has a well-defined position with a localization accuracy of 0.05 angstrom at a specific time after the initial pump pulse. The evolving wave packet then can be probed by another laser pulse, probe pulse, that arrives after the pump pulse. The cross correlation between pump and probe pulse sets the "shutter speed". Because of the fs or sub-ps pulse width for both pump and

probe pulse, the experiments have sufficient temporal resolution to directly observe chemical bond breaking and formation, in addition to transient intermediate chemical species.

Professor Warren, who was a postdoc in Zewail's lab, extended fs transient state spectroscopy to an imaging modality by incorporating laser scanning microscopy (LSM). His work demonstrates the use of electronic and vibrational excited states such as Two-photon Absorption (TPA), Excited State Absorption (ESA), Stimulated Emission (SE), Ground State Depletion (GSD) and even Stimulated Raman Scattering (SRS), for imaging contrast[24]. Whereas most transient absorption spectroscopy experiments used low repetition-rate (~kHz) amplified lasers, Warren's approach [25] used high repetition-rate (~80MHz) unamplified laser pulses with a high frequency modulation scheme to overcome laser RIN. Their initial applications were to generate pump-probe images of melanin and hemoglobin with each pixel consisting of a transient absorption (TA) decay curve. Their results demonstrated the potential of using TA for analyzing chemical composition, based on the TA signal's dependence on pump and probe wavelengths and time delay.

For example, Fu [25], one of the PhD students in Warren's lab, was able to discern the oxygenation difference between deoxyhemoglobin and oxyhemoglobin based on the TA decay constants difference. The pump-probe imaging modality can also discern hemoglobin and melanin simultaneously[26], as shown in figure 1.8 (A) and (B). Fig.1.8 (C) shows the mouse a 3D TAM image of mouse dermal microvasculature at 0 fs interpulse delay.

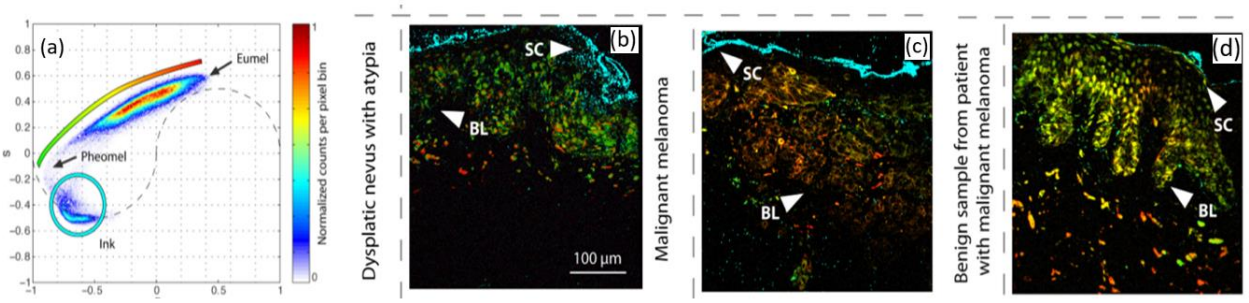

Figure 1.8: Transient absorption image of mouse dermal microvasculature (a)Representative TA delay curves using 810nm probe and 720nm pump for eumelanin, pheomelanin and hemoglobin. (c) 3D reconstruction of the microvasculature. Figure credit: [26].

When TAM is applied to melanoma imaging, Robles and his colleagues[27], under the guidance of Prof. Warren, used a novel data analysis method, phasor analysis, to characterize excited-state lifetimes at each pixel. They used TAM to acquire images from melanoma, dysplastic nevi, and benign nevi. Figure.1.9(b) (c) and (d) show example TAM images, color-coded based on the phasor analysis. From the phasor analysis (Figure.1.9(a)), one can notice the eumelanin, pheomelanin and surgical ink used to mark the samples occupy separate spaces on the phasor plot. Therefore, their achievement proves that even in an environment with highly mixed eumelanin and pheomelanin, incorporating TAM with the phasor analysis can separate melanoma from benign nevus.

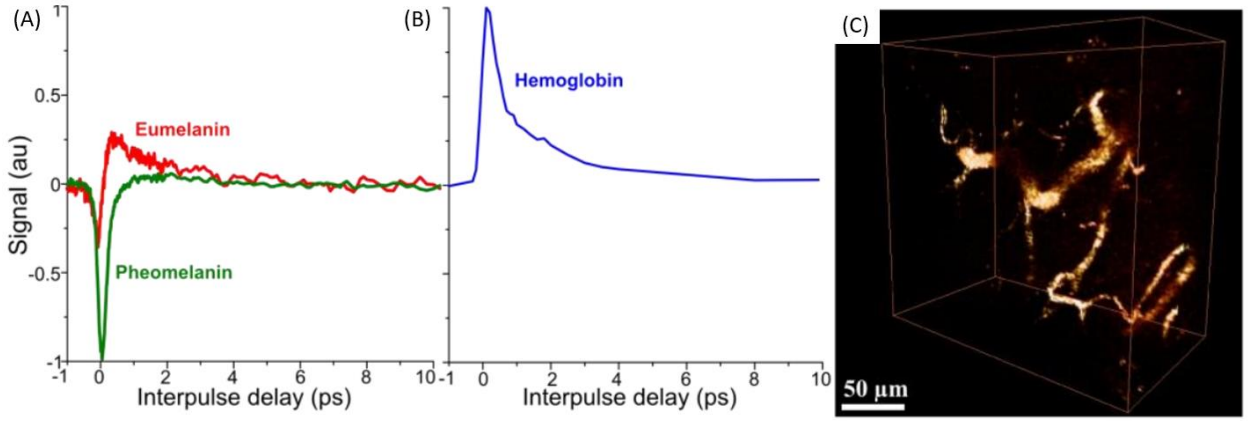

Figure 1.9: Phasor plots for the eumelanin, pheomelanin and surgical ink (a) and TA images of a dysplastic nevus with atypia(b), malignant melanoma(c), and benign nevus (d). SC: stratum corneum; BL: basal layer. Figure credit: [27].

Chapter 2. Nonlinear optics basics

2.1 Electromagnetic theory for nonlinear optics.

Maxwell's equations without free charges or magnetization take the form as follows[28]:

$$\nabla \times \vec{H}(\vec{r},t) = \frac{\partial \vec{D}}{\partial t} \quad (2.1)$$

$$\nabla \times \vec{E}(\vec{r},t) = \frac{\partial \vec{B}}{\partial t} \quad (2.2)$$

$$\nabla \cdot \vec{B}(\vec{r},t) = 0 \quad (2.3)$$

$$\nabla \cdot \vec{E}(\vec{r},t) = 0 \quad (2.4)$$

$$\vec{D}(\vec{r},t) = \varepsilon_0 \vec{E}(\vec{r},t) + \vec{P}(\vec{r},t) \quad (2.5)$$

$$\vec{B}(\vec{r},t) = \mu_0 \vec{H}(\vec{r},t) \quad (2.6)$$

The variables in the equations are the electric displacement D (Coulomb/m^2), electric field E (V/m), magnetic field B (Henry · Ampere/m^2), magnetic field H (Ampere/m), and polarization $\boldsymbol{P}$ (Coulomb/m^2). The constants ε_0 and μ_0 are free space permittivity (Farad/m) and permeability (Henry/m) respectively.

Equation 2.2 indicates that E and B are coupled, meaning a changing magnetic field produces an electric field. We can decouple them by applying curl to both sides of the equation:

$$\nabla \times \left(\nabla \times \vec{E}\right) = \nabla\left(\nabla \cdot \vec{E}\right) - \nabla^2\vec{E} = -\nabla \times \left(\frac{\partial \vec{B}}{\partial t}\right) = -\frac{\partial\left(\nabla \times \vec{B}\right)}{\partial t} = -\mu_0 \frac{\partial^2 \vec{D}}{\partial t^2} \quad (2.7)$$

Substituting Eq. (2.4) and Eq. (2.5) into Eq. (2.7), we can simplify the equation to:

$$\nabla^2\vec{E} = \mu_0\varepsilon_0 \frac{\partial^2}{\partial t^2}\, \vec{E}(\vec{r}, t) + \mu_0 \frac{\partial^2}{\partial t^2}[\vec{P}^L(\vec{r}, t) + \vec{P}^{NL}(\vec{r}, t)] \quad (2.8)$$

Equation 2.8 is the wave equation describing a medium with polarization. The polarization has linear and nonlinear contributions, namely $\vec{P}^L(\vec{r}, t)$ and $\vec{P}^{NL}(\vec{r}, t)$. For a medium that does not have polarizations, this reduces to a homogeneous differential equation with solutions of the form $A \cdot \exp\left[j\left(\vec{k} \cdot \vec{r} - \omega t + \phi_0\right)\right]$ (plane wave) or $\frac{A}{r} \cdot \exp\left[j\left(\vec{k} \cdot \vec{r} - \omega t + \phi_0\right)\right]$ (spherical wave)[29]. However, the polarization terms make it is hard to find the generic analytical solutions.

To solve the wave equation that considers polarization, we need to express complex forms of the electric field and nonlinear polarization as sums of discrete frequency components. The amplitude of linear polarization term for each frequency component is just linear proportional to the corresponding electric field amplitude (equation 2.11).

$$\vec{E}(\vec{r}, t) = \frac{1}{2}\sum_n E_n \exp\{i(\omega_n t - k_n z)\} + c.c \quad (2.9)$$

$$\vec{P}^{NL}(\vec{r}, t) = \frac{1}{2}\sum_n P_n^{NL} \exp\{i(\omega_n t - k_n z)\} + c.c \quad (2.10)$$

$$P_n^L = \varepsilon_0 \mathrm{X}^{(1)} E_n \quad (2.11)$$

Where wavenumber $k_n = \frac{\omega_n}{c}\sqrt{1+\chi^{(1)}} = n_n\omega_n/c$, n_n and ω_n are the medium refractive index and the angular frequency for the nth discrete frequency component. One thing to notice that the electric field amplitude E_n, linear and nonlinear polarization amplitude P_n^L and P_n^{NL} are all functions of space $\vec{r}$ and time t, which have been omitted in the equations above for brevity.

Substituting equation (2.9) (2.10) (2.11) into equation (2.8), we can reach a simplified formula that relates electric field amplitude and nonlinear polarization amplitude of n^{th} frequency component:

$$\frac{\partial E_n}{\partial z} = -\frac{i\omega_n}{2cn_n\varepsilon_0}P_n^{NL} \quad (2.12)$$

This ordinary differential equation describes nonlinear optical interactions where all frequency components can be treated as co-propagating plane waves. With it, we can solve for the newly generated field with prior knowledge of the nonlinear polarization, which depends on the incident electric fields and the material properties.

2.2 Third order process in transient absorption spectroscopy.

Transient Absorption Spectroscopy (TAS) resembles Stimulated Raman Scattering (SRS) in that both are based on 3rd order nonlinear interactions. TAS measures a signal elicited from three electric fields incident on the sample[30]. The first two E fields are from the pump laser pulse. The third is from the probe pulse[30–32]. The measured E field is also from the probe pulse. The nonlinear polarization that created by the first three E fields interact with the measured E field to modulate the measured E field intensity.

One crucial property that governs the third-order process is the third-order nonlinear susceptibility $\chi^{(3)}$ which is a complex variable, $\chi^{(3)} = \chi^{(3)'} + i\chi^{(3)''}$. In TAS, we detect changes in probe

amplitude, rather than phase, so we will focus on the imaginary part of $\chi^{(3)}$. Adapting Geoffery New's description of SRS[33], we can relate the nonlinear polarization amplitude and electric field amplitudes of the pump and probe laser pulses.

$$P^{(NL)} = \frac{3}{2}\varepsilon_0 i\chi^{(3)''}\left|E(\omega_{pump})\right|^2 E(\omega_{probe}) \quad (2.13)$$

Substituting (2.13) into (2.12)[34], and calculating the measurable time-averaged intensity of an electric field, $I = \frac{n\varepsilon_0}{2}|E|^2$, we reach the following equation that describes the probe laser intensity change with respect to the propagation length z inside the material.

$$\frac{\partial I_{\text{probe}}}{\partial z} = \frac{3\omega_{\text{probe}}\,\chi^{(3)''^2} I_{\text{pump}}}{c^2\varepsilon_0\, n_{\text{pump}}\, n_{\text{probe}}} I_{\text{probe}} = g\, I_{\text{probe}} \quad (2.14)$$

This has a simple, that of exponential gain/decay, depending on the sign of g

$$I_{probe}(z) = I_{probe}(0)e^{gz}, \quad (2.15)$$

where

$$g = \frac{3\omega_{\text{probe}}\chi^{(3)''^2} I_{\text{pump}}}{c^2\varepsilon_0 n_{\text{pump}} n_{\text{probe}}}. \quad (2.16)$$

This g factor is analogous to the laser gain factor. We can roughly account for relaxation of excited states by writing $\chi^{(3)''^2}$ as following:

$$\chi_{TA}^{(3)''^2} \propto \sigma_{pump} \times \exp\left(-\frac{\tau}{\tau_{\text{lifetime}}}\right) \times \sigma_{probe} \quad (2.17)$$

Where σ_{pump} and σ_{probe} are absorption cross-sections of the pump laser and probe laser, respectively. The exponential decay term describes the relaxation of the sample, after excitation by the pump, back to an equilibrium state.

The above discussion neglects polarization of the pump and probe and anisotropy of the material[35–38]. To account for this, $\chi_{TA}^{(3)}$ needs to be written as a tensor which has 3^4=81 elements [33]. The nonlinear polarization then becomes

$$P_i = \varepsilon_0 \sum_{jkl} \chi_{ijkl}^{(3)} E_j E_k E_l \quad (2.18)$$

Where $i, j, k, l = x, y, z$, the first two E fields on the RHS are from pump pulse, and the third E field is from the incident probe pulse. As before, the detected probe pulse can be solved through the Eqn. (2.12). The polarization dependence will not be discussed further in this dissertation; for more on this topic, we refer the reader to 2-dimensional spectroscopy works published by Dr. Martin Zanni's group[30] and Dr. Amber Krummel's group[39].

Chapter 3. Initial preparations

3.1 Modeling on photothermal buildup versus laser scanning velocity

Our previous transient absorption results showed little contrast between reduced and oxidized cytochrome *c*, due to severe heat accumulation from our high laser repetition rate. The goal here is to find a laser scanning speed that will limit heat buildup at the focal point to a several Kelvin increase in temperature.

The basic idea of the simulation is to use the finite element method (FEM) to solve partial differential equations (PDE) for heat transport in biological tissues. Our approach was first described in[40–42] . The heat deposited by the laser will be dissipated from the focus to the surrounding tissue area on the basis of the following equation:

$$k\nabla^2 T(y,z,t) = -\rho C\frac{\partial T}{\partial t} + Q(y,z,t), \quad (3.1)$$

where ρ is the tissue density, C is the heat capacity, k is the heat conductivity in the units of W/mK, and Q is the heat source term as a function of the molecule number density, tissue absorption cross-section, and focused laser properties. The constants used here are k=0.02576× 10^{-6}W/(m×K), ρ=911 kg/m^3 and C=1.005 J/K [43], parameters that are typical for brown adipose tissue, which has a high density of mitochondria. We also simplified this problem to a 2D model with respect to the optical axis z and one orthogonal axis y. Since, for convenience, the tissue is assumed to be homogeneous, the heat distribution along the x-axis should follow the same nature as it is along the y-axis.

Then, at the center of the tissue space, the heat source Q is proportional to the Gaussian beam intensity distribution, whose properties, such as beam waist and Rayleigh range, are determined by the objective lens (0.5 NA), input laser wavelength (530 nm) and average power (2mW). The heat source Q, along with the finite element mesh, is shown in figure 3.1 (a).

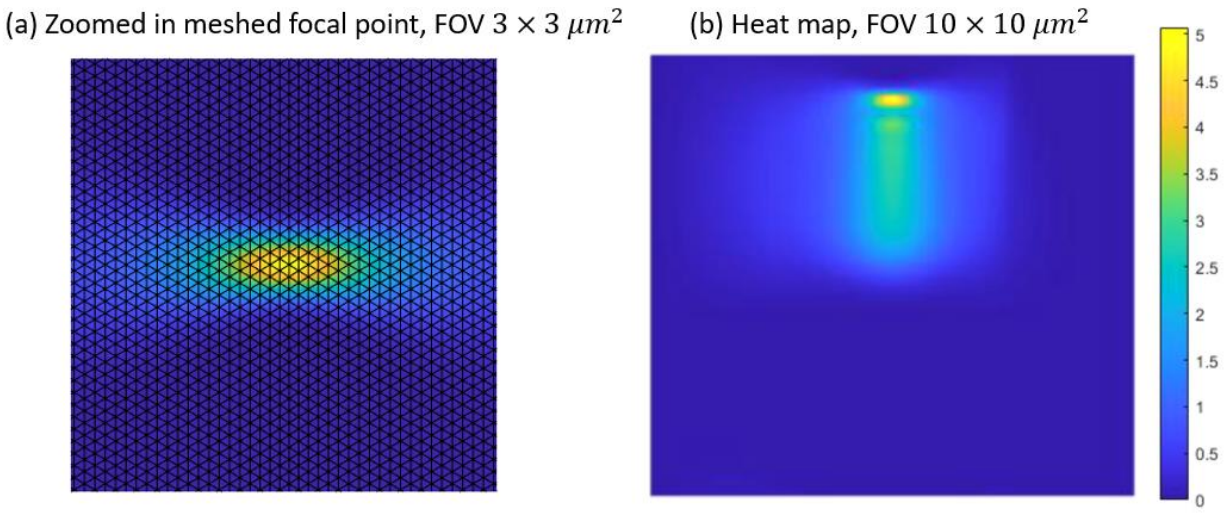

Figure 3.1: FEM results on local temperature rise caused by moving focused laser spot.

We used MATLAB Partial Differential Equation Toolbox to simulate the heat dissipation from a moving laser focus to the adjacent finite elements over time. We effectively modeled the motion of the laser by shifting the sample space downward along the vertical axis with a step size of 1.5 µm while always keeping the laser focus at the origin point. We assigned a 0.5 µs time window for each step which is equivalent to a focused laser traveling 1.5 µm in 0.5 µs. Inside each 0.5 µs time segment, we divide it to even finer time segments. The spacing between those finer time points is 0.025 µs which corresponds to ∂t in Equation 3.1. At the beginning of the first step, the temperature distribution is zero for every finite element. At the end of the first step, the PDE toolbox solves for the heat distribution after 0.5 µs of laser exposure. Then, the heat distribution is shifted downwards by 1.5 µm and serves as the initial condition for the next step. With the updated

initial condition, the PDE toolbox solves for the heat distribution after another 0.5 μs of laser exposure. This process is repeated until the tissue space moves downward by 9 μm. Figure 3.1(b) shows the result, after shifting the heat distribution back to show the effects of a moving beam through fixed tissue. The simulation result shows that a 3m/s scanning rate with 2 mW laser power leads to a less than 5 K temperature rise inside the biological tissue.

3.2 Zemax simulation of chromatic aberration in TAM

The signal measured in TAM is proportional to spatial overlap between pump and probe pulses, which are often centered at different wavelengths. Therefore, chromatic aberration is a major limiting factor in the illumination optics[44] . Owing to dispersion, conventional single-material lenses will lead to different wavelengths being focused at different locations along the optical axis. The resulting lack of spatial overlap drastically degrades the TA signal. This section describes the use of Zemax to choose the correct scanning and tube lenses to maximize spatial overlap between a 480nm pump and 530nm probe.

The Zemax simulation is set up with two achromatic doublet lenses from Thorlabs as the scanning and tube lenses (AC508-075-A-ML AC508-100-A-ML AC508-150-A-ML) and two paraxial lenses with 10mm focal length as the objective and condenser lens and (Zemax lacks specifications for the actual objective and condenser lenses; we assume the actual objective and condenser lenses to have a similar performance as the ideal paraxial lenses). Figure 3.2 shows the resulting distribution of 480nm and 530nm rays at the sample plane for on-axis (upper-left plot) and off-axis (upper-right and lower plots) ray bundles. The main point here is not the exact focal spot size (4 μm), which can be modeled more accurately with a better model of the objective, but the close overlap between different wavelengths, owing to chromatic aberration compensation of the achromatic doublet lenses.

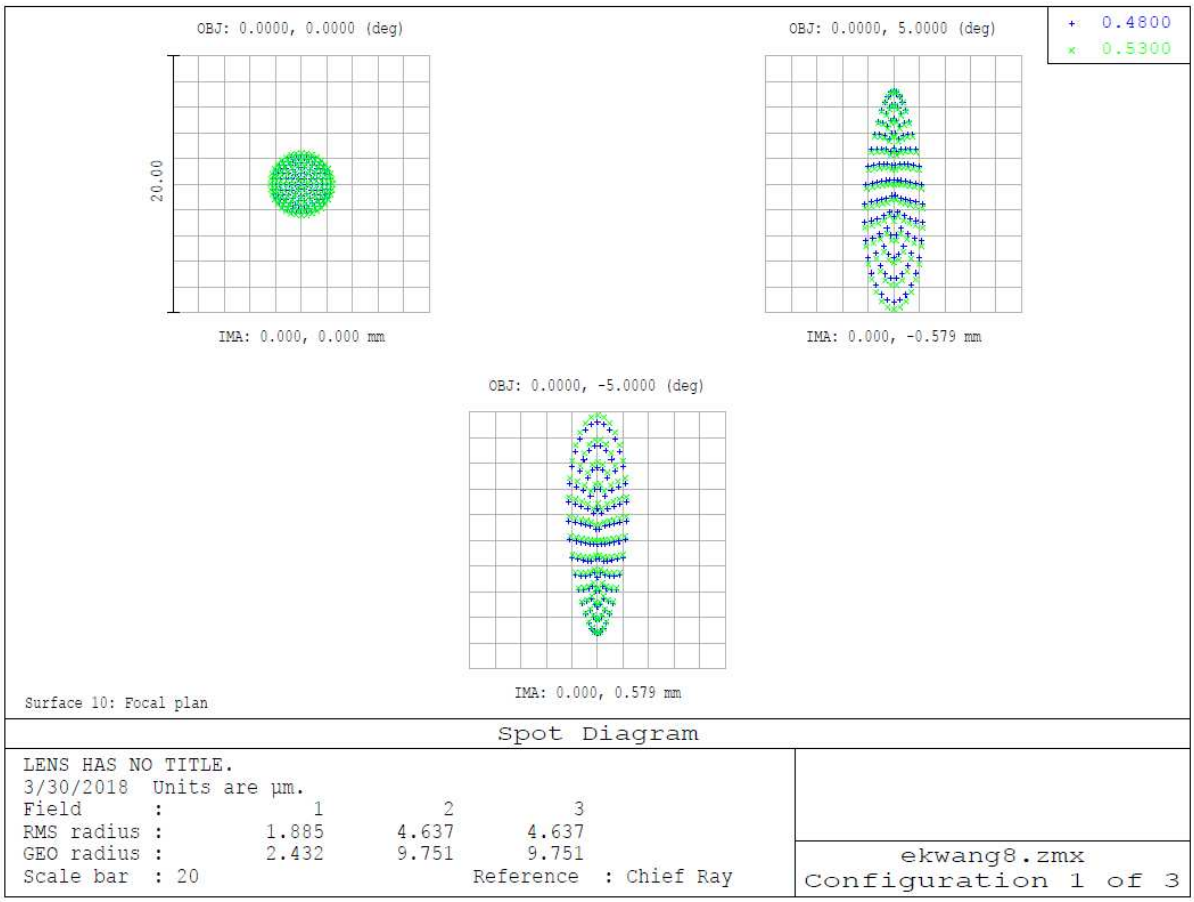

Figure 3.2: Zemax simulation on spatial overlap between 530nm and 490nm using chromatic doublet scan and tube lenses. Grid size 2 µm.

For comparison, Fig. 3.3 shows a simulation using two plano-convex lenses as scanning and tube lens instead of the achromatic doublets. A clear walk-off between two beams can be observed. Even with a relatively small scanning angle equal to +/-2 degrees, we can observe an apparent offset between the intense centroids of the two beams. Even at a scanning angle of 0 degrees, the 530 nm beam forms a much larger spot than the 490 nm beam.

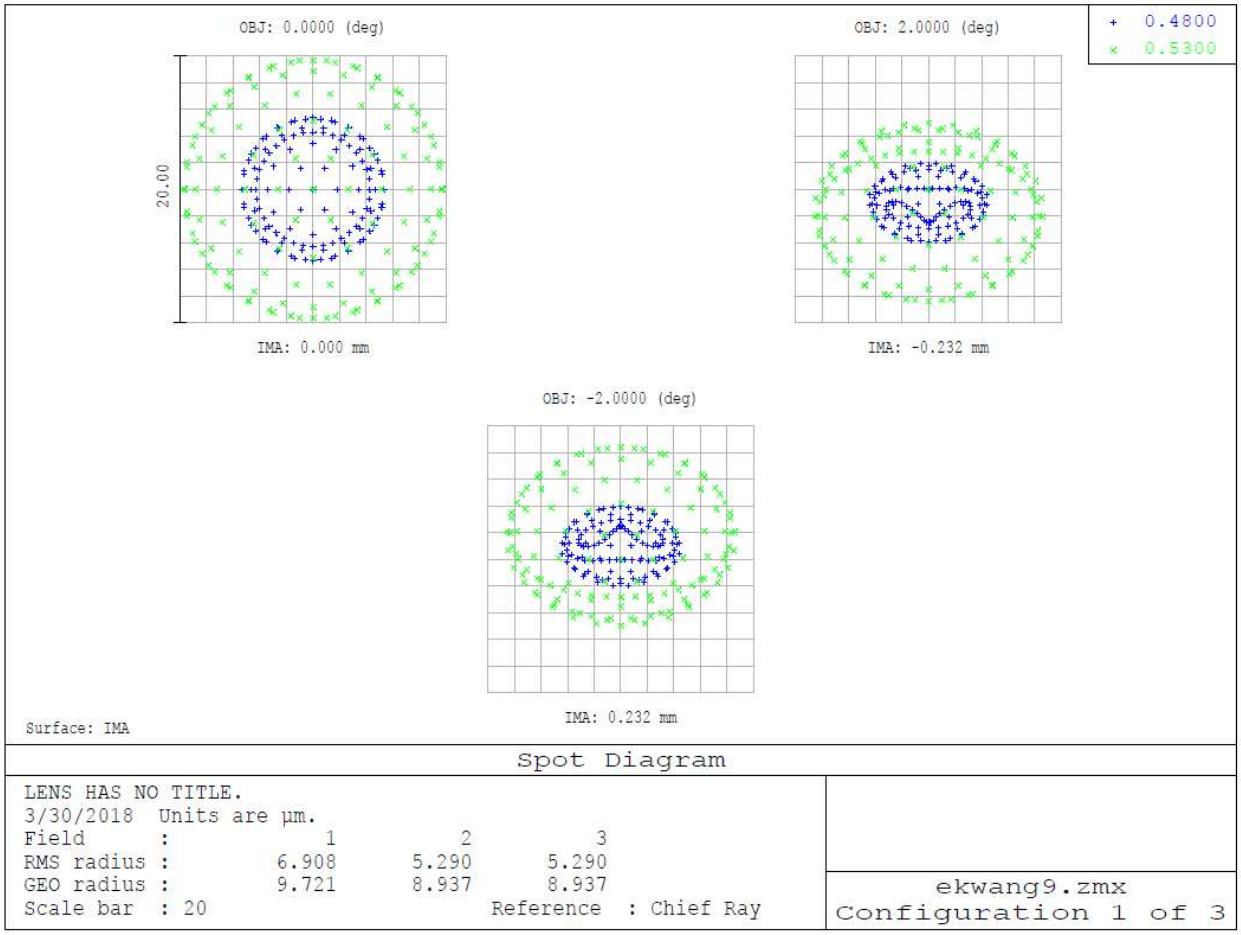

Figure 3.3: Zemax simulation on spatial overlap between 530nm and 490nm using plano-convex scan and tube lenses

Finally, Fig. 3.4 shows results using ideal paraxial lenses for all the lenses in the system. This is the theoretical limit if all aberrations could be compensated perfectly. Not only is the spatial overlap maintained, but also the elongated distortion disappears when the scanning angle is large.

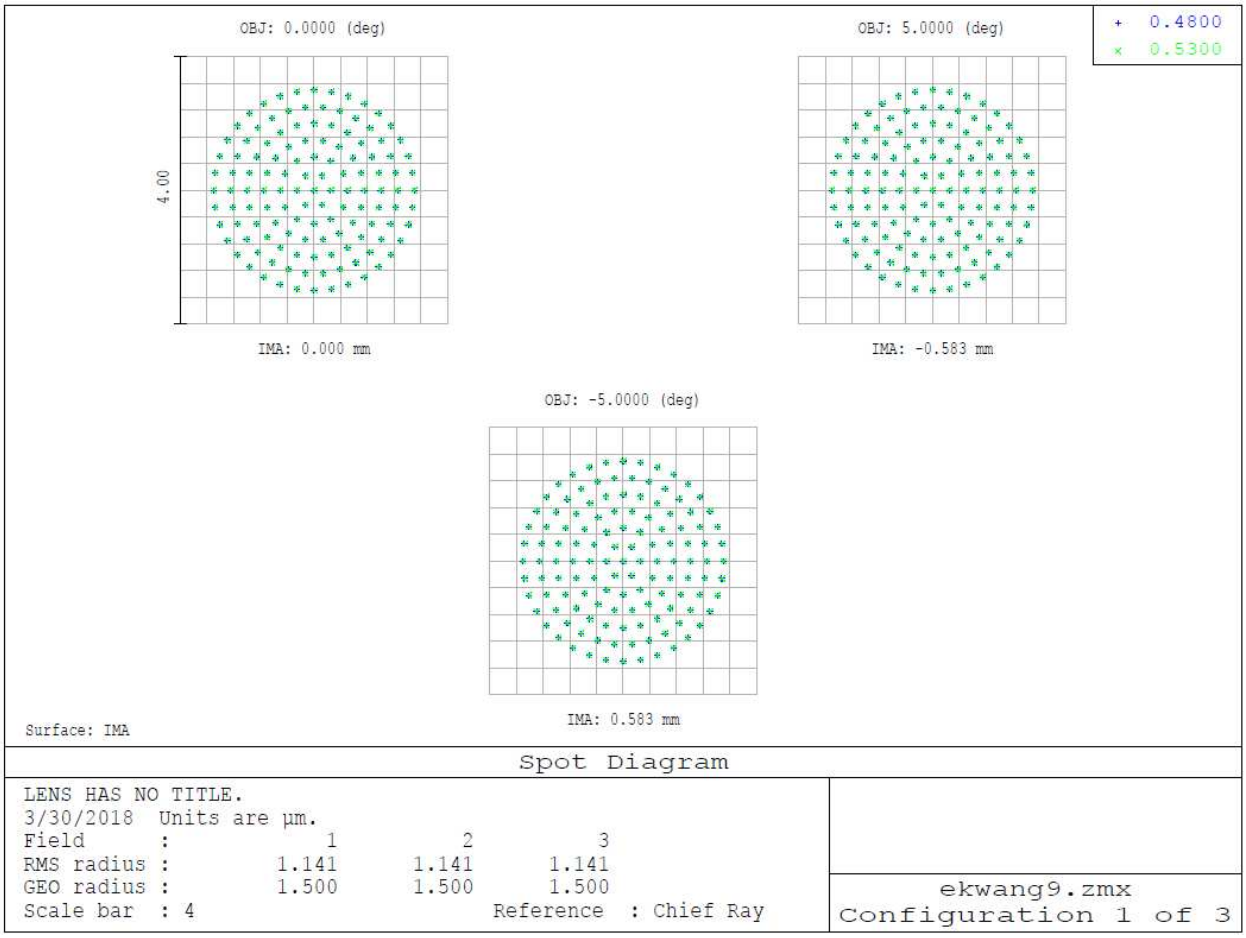

Figure 3.4: Zemax simulation on spatial overlap between 530nm and 490nm using paraxial scan and tube lenses.

Chapter 4. Spectroscopy, excited states, and relaxation processes in cytochromes.

4.1 Introduction

Mitochondria generate most of the ATP that supplies energy for life. They utilize an electrochemical proton gradient across their inner membranes, maintained by the respiratory chain, to produce ATP. Inside the respiratory chain, electrons pass through molecules with varying redox potential, including cytochromes, ending up in Complex IV where they react with oxygen and protons to form water. At each step of electron transport, potential energy from the electrons is used to pump protons into the intermembrane space, providing the electrochemical gradient for ATP production in Respiratory Complex V. Therefore, the redox state of the electron transport molecules is an essential indicator of cell metabolism and associated diseases like cancer, diabetes, aging, and neurodegenerative and mitochondrial disorders.

Established techniques for mitochondrial redox imaging use fluorescence of FAD^+ and NADH[45–47]. This is sensitive to redox at the *input* to the respiratory chain, but not the respiratory chain itself. An increase in oxidation indicated by FAD^+/NADH fluorescence could equally indicate increased ATP consumption in the cell due to normal metabolic demands, or increased electron leakage along the respiratory chain and production of reactive oxygen species (ROS), with no way to tell the difference.

Therefore cytochromes, which mediate electron transport *within* the respiratory chain, could provide more information about mitochondrial functioning and health. Our approach is to

differentiate cytochrome redox states based on transient excited states and associated relaxation times. In this chapter, I will briefly describe the optical absorption spectra and excited states of cytochromes from a quantum chemistry perspective, following Gouterman's four-orbital theory[48,49], the processes involved in relaxation from an excited state, and the underlying reasons for redox differences in both static and transient absorption spectra.

4.2 Electronic structure of cytochrome *c*

Fig. 4.1(a) shows the proposed energy level diagram of cytochrome *c*. From left to right shows tryptophan's ground state (S_0) and excited state (S_3), the porphyrin ground state (S_0) and excited state (S_1) and Fe d-orbital energy levels. The green dashed line indicates the pump photon absorption at time zero, which promotes electrons to porphyrin excited state. The blue dashed line indicates the probe photon absorption if the pump probe delay is smaller than porphyrin's excited state lifetime. The purple, orange and black solid lines indicate multiple relaxation pathways which closely relate to time constants extracted from TA curves.

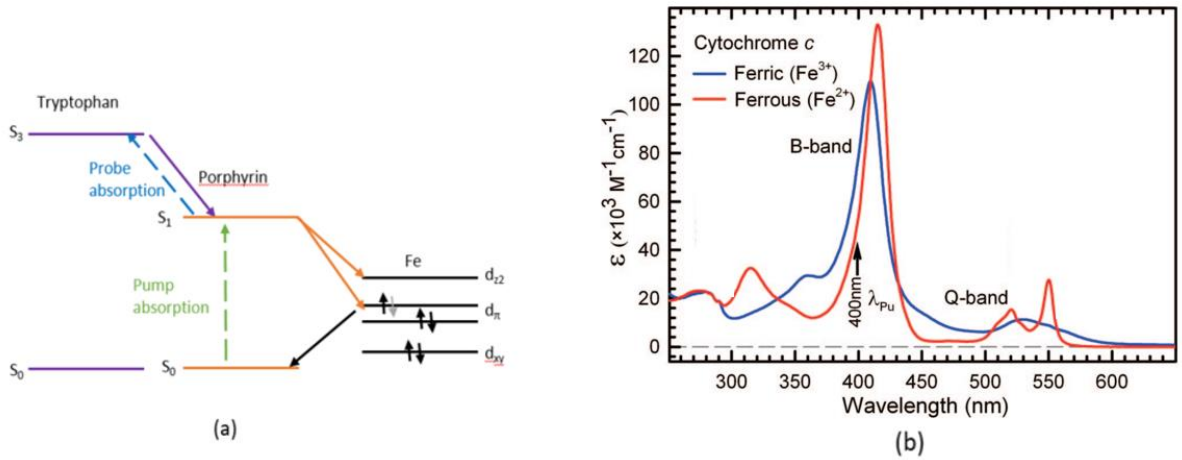

Figure 4.1a) Cytochrome c energy levels. (b) Static absorption spectrum, reproduced from [50].

From the static absorption spectrum, Fig. 4.1(b), three distinct absorption bands are presented. The UV absorption band at 280nm corresponds to tryptophan excited state, B-band and Q-band are

derived from configuration interaction between HOMO (a_{2u}, a_{1u}) and LUMO (e_g) of the porphyrin ring. However, the excited Fe states cannot be observed from static absorption spectrum. But those states are important in explaining ultrafast relaxation. How to relate these excited Fe states to the transient absorption response will be discussed in more detail in Section 4.3. Our experiment focuses on the visible-wavelength pulses, so this section is constrained on the origin of visible (B and Q) absorption bands. The two major aspects that determine the B and Q absorption bands are electronic and vibrionic in origin. In general, purely electronic contributions determines Q_0 and B_0 bands, vibronic Frank-Condon broadening accounts for the widths of the B and Q bands, and vibronic Herzberg-Teller coupling accounts for the emergence of the Q_v band in between the Q and B bands.

Electronic contribution: The prominent B (~400nm) and Q (~550nm) absorption bands have been long understood in the framework of Gouterman's analysis of the highest occupied and lowest unoccupied molecular orbitals (HOMO, LUMO) of porphyrins and the interactions (e.g. Coulomb repulsion) between their excited-state configurations [51]. Gouterman's model was based on adding configuration interaction (i.e. electron-electron repulsion) considerations to the molecular orbitals previously formulated by a linear combination of $2p_z$ atomic orbitals, labeled by their symmetry species by Longuet-Higgins[52]. With the assumption of D_{4h} symmetry for porphyrin structure, Longuet-Higgins calculated molecular orbitals (MOs) with multiple possible symmetry species, such as $a_{2u}, b_{2u} a_{1u}, b_{1u}$, and e_g[49]. It turns out that porphyrins have two degenerate (equal energy) HOMOs of a_{2u} anda_{1u} symmetry, and two degenerate LUMOs of e_g symmetry. These LCAO-MOs are illustrated in Fig. 4.2.

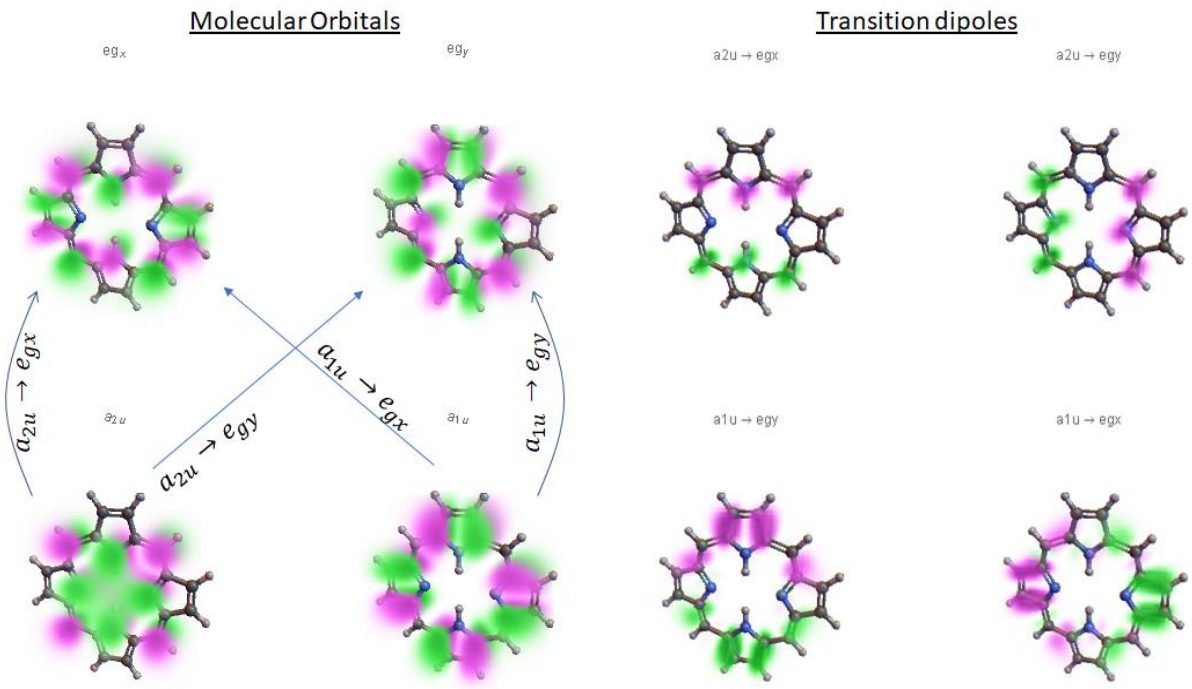

Figure 4.2: Rendering of molecular orbital and transition dipoles. Figure credit: Jesse Wilson.

Based on Higgins' identification of four HOMO and LUMO orbitals, Gouterman used configuration interaction to describe the origin of B_0 and Q_0 bands. These MOs are mixed into possible configurations, ($a_{1u}e_{gy}$) ($a_{1u}e_{gx}$) ($a_{2u}e_{gy}$) ($a_{2u}e_{gx}$), to calculate the excited electronic states corresponding to B and Q band.

For porphyrins, the ground state has two electrons in each of the HOMO orbitals,

$$|g\rangle = |A_{1u}(1)\rangle|A_{1u}(2)\rangle|A_{2u}(3)\rangle|A_{2u}(4)\rangle \quad (4.1)$$

A single-photon transition can move one of these electrons to a LUMO. Possible excited *configurations* include

$$\left|E_{gy}(1)\right\rangle|A_{1u}(2)\rangle|A_{2u}(3)\rangle|A_{2u}(4)\rangle \equiv \left|E_{gy}A_{1u}\right\rangle, (4.2)$$

$$\left|E_{gx}(1)\right\rangle|A_{1u}(2)\rangle|A_{2u}(3)\rangle|A_{2u}(4)\rangle \equiv |E_{gx}A_{1u}\rangle, (4.3)$$

$$|A_{1u}(1)\rangle|A_{1u}(2)\rangle\left|E_{gy}(3)\right\rangle|A_{2u}(4)\rangle \equiv \left|E_{gy}A_{2u}\right\rangle, (4.4)$$

$$|A_{1u}(1)\rangle|A_{1u}(2)\rangle\left|E_{gx}(3)\right\rangle|A_{2u}(4)\rangle \equiv |E_{gx}A_{2u}\rangle, (4.5)$$

And their permutations. There are therefore four one-electron dipole transition moments to consider (Fig 4.2(b)): $\langle E_{gx}|\mu_y|A_{2u}\rangle, \langle E_{gy}|\mu_y|A_{1u}\rangle, \langle E_{gy}|\mu_x|A_{2u}\rangle$, and $\langle E_{gx}|\mu_x|A_{1u}\rangle$. Because of the near degeneracy of the HOMOs (i.e. $H|A_{1u}\rangle \approx H|A_{2u}\rangle$) and the degeneracy of the LUMOs (i.e. $H\left|E_{gx}\right\rangle = H|E_{gy}\rangle$), an optical interaction μ_y that promotes $A_{2u} \rightarrow E_{gx}$ will simultaneously promote $A_{1u} \rightarrow E_{gy}$. Likewise, an optical interaction μ_x that promotes $A_{2u} \rightarrow E_{gy}$ will simultaneously promote $A_{1u} \rightarrow E_{gx}$. Therefore, a complete description comprises a dipole transition from the ground state into a linear superposition of excited configurations. These are known as the Q and Soret transitions:

$$S_y: \langle A_{2u}E_{gx} + A_{1u}E_{gy}|\mu_y|g\rangle, (4.6)$$

$$S_x: \langle A_{2u}E_{gy} + A_{1u}E_{gx}|\mu_x|g\rangle, (4.7)$$

$$Q_y: \langle A_{2u}E_{gx} - A_{1u}E_{gy}|\mu_y|g\rangle, (4.8)$$

$$Q_x: \langle A_{2u}E_{gy} - A_{1u}E_{gx}|\mu_x|g\rangle, (4.9)$$

In the Soret transition, the two dipoles add constructively, while in the Q transition, the two dipoles partially cancel each other. That explains why typically the Soret bands are intense, whereas the Q bands are comparatively weak.

$$Q_y: |S_{1y}\rangle = |A_{2u}E_{gx} - A_{1u}E_{gy}\rangle, (4.10)$$

The excited states are known as the Q (S_{1x}, S_{1y}) and Soret (S_{2x}, S_{2y}) states.

$$Q_x: |S_{1x}\rangle = |A_{2u}E_{gy} - A_{1u}E_{gx}\rangle, (4.11)$$

$$S_y: |S_{2y}\rangle = |A_{2u}E_{gx} + A_{1u}E_{gy}\rangle, (4.12)$$

The energy levels of these excited states are calculated as usual through the Hamiltonian, e.g.

$$S_x: |S_{2x}\rangle = |A_{2u}E_{gy} + A_{1u}E_{gy}\rangle. \quad (4.13)$$

$$\begin{aligned} E_{Qy} &= \langle A_{2u}E_{gx} - A_{1u}E_{gy}|H|A_{2u}E_{gx} - A_{1u}E_{gy}\rangle \\ &= \langle A_{2u}E_{gx}|H|A_{2u}E_{gx}\rangle + \langle A_{1u}E_{gy}|H|A_{1u}E_{gy}\rangle \\ &\quad - 2\langle A_{2u}E_{gx}|H|A_{1u}E_{gy}\rangle \quad (4.14) \end{aligned}$$

$$\begin{aligned} E_{Sy} &= \langle A_{2u}E_{gx} + A_{1u}E_{gy}|H|A_{2u}E_{gx} + A_{1u}E_{gy}\rangle \\ &= \langle A_{2u}E_{gx}|H|A_{2u}E_{gx}\rangle + \langle A_{1u}E_{gy}|H|A_{1u}E_{gy}\rangle \\ &\quad + 2\langle A_{2u}E_{gx}|H|A_{1u}E_{gy}\rangle \quad (4.15) \end{aligned}$$

The above equations differ only in sign of the third term, which explains the energy splitting between the Q and Soret bands. This term accounts for Coulomb repulsion between electrons in the excited configurations.

In sum, Gouterman's four-orbital theory uses configuration interaction between combinations of single-electron $2p_z$ orbitals to explain the positions and relative strengths of the S_{00} and Q_{00} (zero-phonon) absorption bands. It does not account for the broadening of these bands, the emergence of the 520nm Q_v band in reduced cytochrome *c*, or the shift in peak position of oxidized cytochrome *c*'s Q band to 530 nm.

Vibronic perturbation: From the absorption spectrum of cytochrome *c*, especially in the reduced Fe^{2+} state, we can clearly observe a distinct Q_v peak on the blue side of Q_0. The formation of this side band arises from vibronic coupling between Q_0 and S_0 transitions. Vibronic effects includes Franck-Condon (F-C) coupling, which considers coupling between vibrational states of grounds state and vibrational states of displaced excited state, and Herzberg-Teller (H-T) coupling, which considers coupling between vibrational states of two excited states (B and Q states in our case). It has been claimed that over 80% of Q_v band absorbance arises from H-T coupling[53]. Schweitzer-

Stenner expressed a given vibronic state as $|Q_{\rho'}v_j^Q\rangle$ as a mixture of adiabatic Q and B states defined in Equation 15 in Ref [54] (to write out this equation, Born-Oppenheimer approximation[55] has been utilized to treat the vibronic wavefunction as the product of an electronic wavefunction and a vibrational wavefunction). After taking H-T and F-C vibronic perturbation into consideration, the electronic dipole transition from the ground state to a vibrationally-excited B state can be expressed as[54]:

$$\left\langle g, 0_j^g \middle| \hat{R}_{\rho'} \middle| B_{\rho'} v_j^B \right\rangle = c_1 \langle g | \hat{R}_{\rho'} | Q_\sigma \rangle \left\langle 0_j^g \middle| v_j^Q - 1 \right\rangle + c_2 \langle g | \hat{R}_{\rho'} | Q_\sigma \rangle \left\langle 0_j^g \middle| v_j^Q + 1 \right\rangle + c_3 \langle g | \hat{R}_{\rho'} | B_\rho \rangle \left\langle 0_j^g \middle| v_j^B \right\rangle \quad (4.16)$$

Likewise, a transition for the Q state can be written:

$$\left\langle g, 0_j^g \middle| \hat{R}_{\rho'} \middle| Q_{\rho'} v_j^Q \right\rangle = d_1 \langle g | \hat{R}_{\rho'} | B_\sigma \rangle \left\langle 0_j^g \middle| v_j^B - 1 \right\rangle + d_2 \langle g | \hat{R}_{\rho'} | B_\sigma \rangle \left\langle 0_j^g \middle| v_j^B + 1 \right\rangle + d_3 \langle g | \hat{R}_{\rho'} | Q_\rho \rangle \left\langle 0_j^g \middle| v_j^Q \right\rangle \quad (4.17)$$

Where $\rho, \sigma = x, y$, j indicates the j^{th} vibrational mode, and g represents the electronic ground state. The existence of the extra variable ρ' indicates that due to the possible mixture of x and y components by vibronic coupling the coordinate system may rotate for the new basis set[54]. Then the above two equations can be achieved. On the right hand sides of both equations above, the first and second terms govern H-T coupling, while the third term accounts for the electronic transition

dipole and the F-C perturbation. The coefficients c_1, c_2, c_3 and d_1, d_2, d_3 indicate the relative strengths between all the possible perturbing mechanisms.

4.3 Transient absorption spectroscopy and dynamics in cytochrome *c*

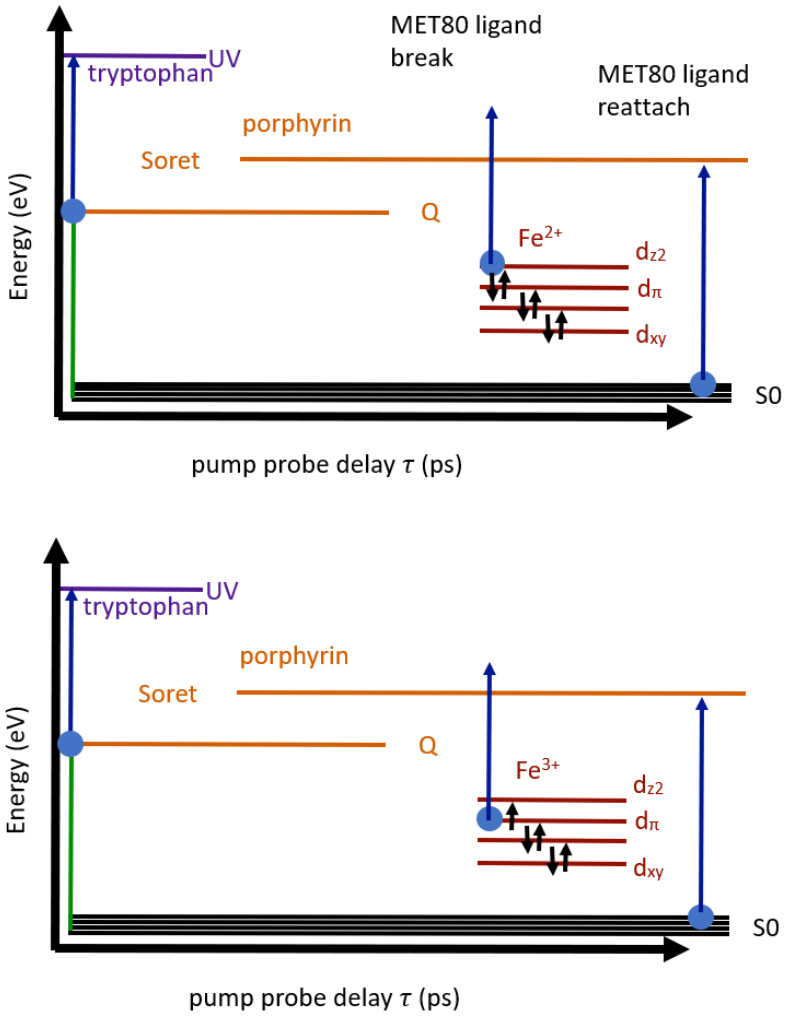

Figure 4.3: ultrafast dynamics breakdown of reduced and oxidized cytochrome c.

As discussed above, the moieties that contribute to the cytochrome *c* excited-state evolution are the tryptophan amino acid, the porphyrin ring, the methionine amino acid (Met80) that is axially ligated to the central iron ion, and the iron ion itself. In our experiment, the electrons are excited by the 530 nm pump to the porphyrin S_1 state (Q-band). That short-lived excited state holds electrons for either 100fs or <40fs for ferrous and ferric form respectively[56]. If a 490 nm probe

pulse arrives within that time, these electrons can be further promoted to tryptophan excited state S_3. This sequential photon absorption is called excited state absorption (ESA). However, if the pump and probe time delay is larger than 100fs, the electrons will have decayed rapidly through either the Fe ion's d_{z^2} or d_π orbitals[39,56], depending on redox state, to a vibrationally-hot ground state. Lastly, the temperature of ground state will steadily decrease which will bring the electrons back to a low vibrational state in electronic ground state. Further details are discussed below.

In the case of probe pulse arriving several ps after the pump pulse, the excited electrons will decay from the Q band to lower energy levels. In reduced cytochrome c, the excited electrons will firstly decay to the d_{z^2} atomic orbital of ferrous ion, causing the Met80 ligand to detach from the iron center. However, the ligand dissociation is not permanent, as it is held in place by the protein structure and reattaches to the ferrous ion after several ps. This ligand dissociation and reattachment contributes a characteristic 5 ps decay time constant to the TA response. In oxidized cytochrome *c*, the excited electron will decay to d_π orbital, which does not give rise to ligand dissociation. Therefore, this axial ligand reattachment time constant is redox-specific.

Finally, the electrons decay from the Fe d orbitals to a highly vibrationally-excited porphyrin ground state. Through internal vibrational redistribution (IVR), the excess energy deposited by pump photon rapidly drives a Maxwell-Boltzman distribution of vibrational energy levels, effectively causing molecular local temperature to increase to 500-700 K[39].This heat rapidly dissipates through surrounding protein and water over the course of about 5 to 10 ps through additional IVR.

Chapter 5. Visible-wavelength TAM based on an ultrafast fiber laser source

5.1 TAM working principles

Our goal is to distinguish different types of cytochromes and their redox states based on measurements of ultrafast transient absorption and make use of this technique for imaging contrast in a laser-scanning microscope.

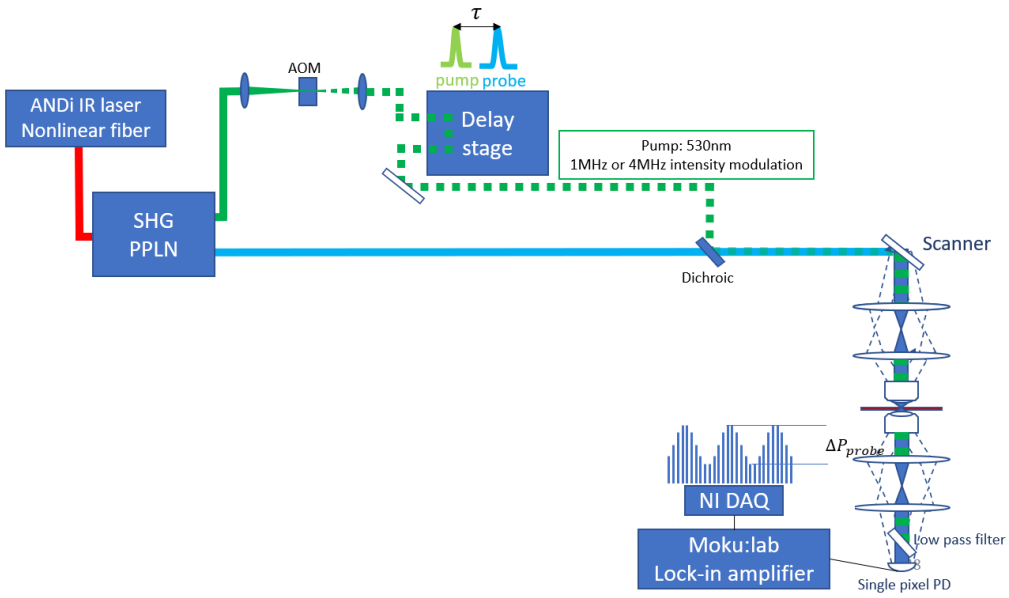

Figure 5.1. TAM with ultrafast fiber laser experiment setup. ANDi IR: all normal dispersion infrared; SHG: second harmonic generation; PPLN: Periodically Poled Lithium Niobate; AOM: acoustic optic modulator; PD: photodetector; τ: pump -probe delay.

Fig. 5.1 shows the optical layout of our two-color ultrafast transient absorption microscope (named TuCo by Scott Domingue, who developed the fiber laser source). We use a fiber-based fs IR laser source to generate two trains of laser pulses, with a center wavelength of 530 nm and 490nm, as pump and probe[57]. The pump and probe are synchronized, and both have 65MHz repetition rates

and ~800 fs pulse widths. The acoustic optical modulator (AOM) exerts an intensity modulation onto the pump pulse train. The modulated pump beam is sent to a motorized delay stage that can vary the pump OPL with the accuracy of 0.1 micrometers. That OPL difference then translates into a pump-probe arrival time difference at the focus inside the sample. We refer this tunable arrival time difference as the pump-probe delay τ. Both beams are combined by a dichroic mirror and then go through a home-built resonant laser scanning microscope (LSM). The LSM consists of a 3.5 kHz resonant scanner along the x axis and a 2.5 Hz rate along the y axis, two 4-*f* imaging systems, one objective lens and one condenser lens. This resonant scan rate, over a 425 μm field of view, translates to a line scanning speed of 3 m/s to limit heating to a few Kelvin at the focal spot as outlined in Chapter 3.[54]A 4-*f* system relays the scanner plane to the back aperture of the objective lens (Olympus UPlanFL N 20X/0.50). Then the collinear scanning pump and probe beams are focused onto the sample, resulting in a scan pattern covering a 425μm× 700μm field of view (FOV). Transmitted light is collected by a condenser lens (Nikon Plan APO 20X/0.75). Lastly, a pump-rejecting filter (FES0500 Thorlabs) only allows the probe to pass through and another 4-*f* system relays the back aperture of the condenser lens to a photodetector (PDA35A). The high numerical aperture of the condenser and the second 4-*f* system, which shrinks the probe beam diameter to the size of the photodetector's active area, mitigate photothermal lensing on the probe.

The pump laser pulse train is intensity modulated at a fixed frequency, for instance, 10 MHz, by an acoustic optical modulator (AOM, TEM-100-25, Brimrose). This frequency is selected to ensure several on/off pump modulation cycles per pixel (the 3.5 kHz line rate, at 516-pixels per line, results in a pixel dwell time of 277 ns). Perturbations to the probe transmissivity caused by pump-induced transient states show up at the same modulation frequency as the pump intensity modulation and are extracted from the probe by a lock-in amplifier (LIA). The decay

characteristics of pump-induced transient states can be measured by increasing τ step by step, forming the basis for molecule-specific nonlinear optical contrast.

5.2 Spectroscopic contrast between reduced and oxidized cytochrome c

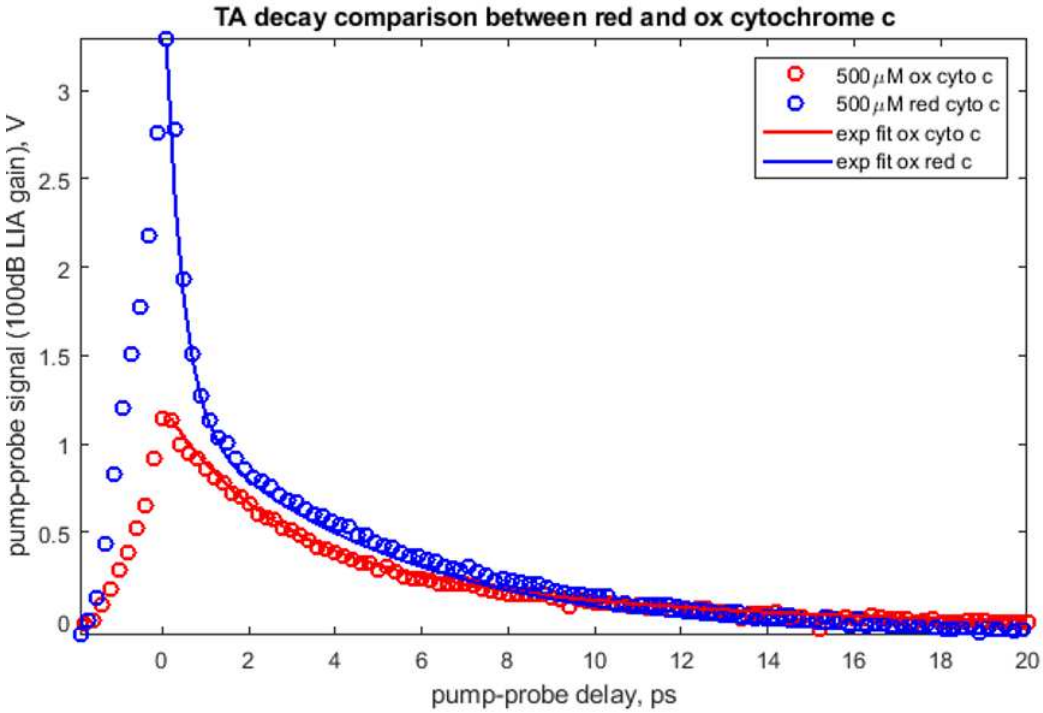

Figure 5.2: TA responses of reduced and oxidized cytochrome c solution.

Different pump-probe wavelength pairs provide us with different contrasts between two redox states. Our first goal is to show that the 530 nm pump and 490 nm probe produced by TuCo will provide redox contrast once sample heating has been mitigated with the resonant scanner. The sample is 0.5 mM horse heart cytochrome *c* (Sigma-Aldrich) solution in a 0.1 mm pathlength cuvette. For the oxidized preparation, powdered cytochrome *c* was dissolved in DI water and diluted to 0.5mM. The reduced form was prepared by adding 5mM sodium hydrosulfide. The molar ratio between sodium hydrosulfide and cytochrome *c* is 10/1, ensuring reduction of all the cytochrome in solution. To avoid heating, the two-dimensional resonant scanner raster scans the focused laser beam through the cuvette. The line scan rate is 3.5kHz; the frame rate is 0.5Hz. The scanning range is carefully tuned until a stable and maximal signal read out by the LIA. After

setting up the scanning range, we scanned the delay stage to vary pump-probe delay τ from -2 to +20ps, with 0.1ps step size. At each step, one pump-probe signal $\Delta P(\tau)$ is recorded, which is the average pump probe signal of the one frame.

From the pump-probe signal shown in Figure 5.2, we can see a significant difference between reduced (red) and oxidized (blue) cytochrome *c*. The first thing to be noticed is the reduced cytochrome *c* has two times more sub-ps ESA response than the oxidized one. The sub-ps ESA difference arises from the tryptophan UV absorbance difference between two redox states. However, sub-picosecond dynamics are not visible due to our the relatively long (800 fs) pulse widths used here. When observing the overall TA decay curves, one would notice that there are two time constants, 0.5ps and 6.53ps, in reduced TA decay after using an exponential curve to fit the reduced measurements. Meanwhile, there is only one time constant, 3.5ps, for the oxidized form. The two time constants of reduced form agree with Consani's measurements[56,58],assigned as hot ground state cooling decay and ligand recombination decay. The 3.5ps time constant of oxidized form also agrees with their results, assigned as ground-state vibrational cooling. These measured time constants are consistent with the observation that Met80 ligand dissociation/re-attachment process only occurs in the reduced form(see Section 4.3).

5.3 Towards pump-probe imaging: relative intensity noise (RIN) reduction

The pump-probe spectroscopic measurements prove that the current pump and probe wavelength pair offers an excellent contrast between two redox states. The next goal is to extend the current spectroscopy modality to an imaging modality. As mentioned before, due to cytochrome's high absorbance, a 3.5kHz high scanning rate two-dimensional scanner must be implemented to avoid excessive heating by the focused visible laser beams. Yet the fast scanning rate also puts a stringent

requirement on pixel dwell time. For example, a 100×100-pixel image with the 3.5 kHz line scanning rate requires very short, 2.8 µs pixel dwell time.

However, because the typical minimum noise floor of a fiber-based ultrafast laser is around -120 dBc/Hz, which is over 40 dB higher than the shot-noise limit, the SNR of the cytochrome's pump-probe signal is insufficient for such short integration times. Considering the relatively high fiber-based laser RIN and the small pump-probe signal ($\Delta P/P_0 \sim 1e-6$), a millisecond integration time is required. Therefore, we employed software-based adaptive noise cancellation (ANC) that can mitigate the laser RIN, and then enhance the SNR to a level that high enough to meet the fast-imaging speed requirement.

In short, the adaptive filter uses a convolutional filter with coefficients w to modify a reference measurement of the laser RIN, $x[n]$, to match rapidly-varying probe signal, $d[n]$. Feedback is used to adjust the coefficients w to minimize the square of the residual difference, $e[n] = d[n] - w \otimes x[n]$, which contains the pump-probe signal minus laser RIN and DC components.

5.3.1 Software adaptive filter results

This Section[1] is a modified form of my work previously published in Journal of Biomedical Optics[59].

Figure 5.3 shows the experiment schematic. The optical setup is similar to Section 2.1. The only difference is to add a 50/50 beam splitter on the probe arm before entering the LSM, in order to sample the reference, x, by a photodetector (PDA36A, Thorlabs). The other half passes through the LSM and then is detected by an identical photodetector, to serve as the signal, d. The reference

[1] Section 5.3.1 has published in Journal of Biomedical Optics.

and signal pass through 22 MHz low-pass anti-aliasing filters (Minicircuits) and are digitized by the two 50 MHz analog to digital converting (ADC) channels of a data acquisition (DAQ) device (Analog Discovery Studio, Digilent). The ADC is synchronized to the resonant scanner through a digital Transistor-Transistor Logic (TTL) trigger.

For this experiment, all digital signal processing is done offline in MATLAB. (Later, we will show results with a real-time FPGA). The transmitted light image is formed by passing the $d(n)$ through a downsampling cascaded integrator comb (CIC) filter [60], which reduces the sample rate from 50 MHz to the pixel rate of 2.56 µs/pixel. The pump-probe image is formed by passing $d[n]$ and $x[n]$ through an adaptive filter (see Appendix A.1) and a lock-in amplifier (see Appendix A.2). The lock-in X and Y channels pass through identical CIC filters to low-pass and downsample to the pixel clock, and the magnitude R is calculated as the final output (limitations with the DAQ digital input buffers prevented simultaneous acquisition of a synchronization signal for f_m that would be required for phase-sensitive detection).

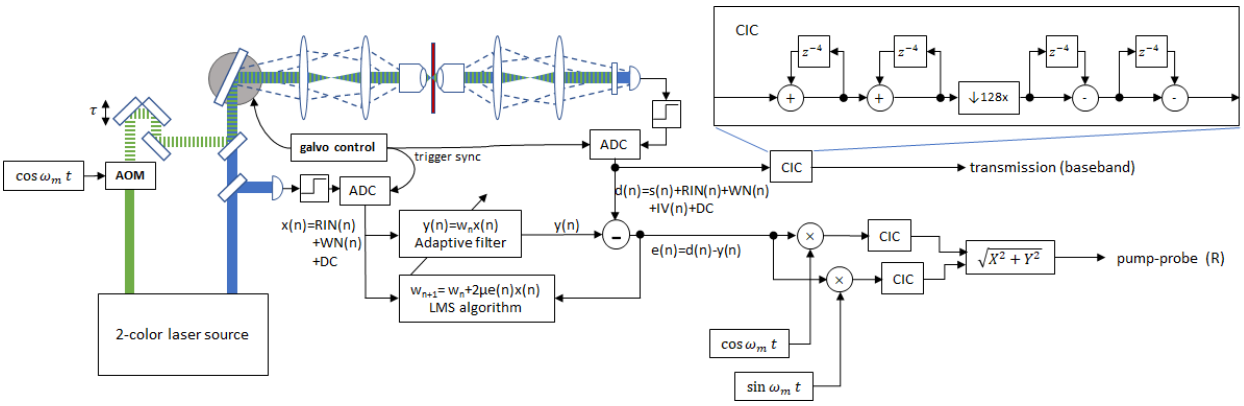

Figure 5.3: A conventional pump-probe microscope is employed to generate probe signal, d(n), and reference, x(n). The probe and reference signals feed into a software-based adaptive filter to produce the output e(n), which contains the pump-probe signal minus estimated RIN. Then, a software LIA and CIC filters are used to demodulate the pump-probe signal from the e(n). The transmission image is generated by directly applying the CIC filter to the probe d(n).

To test the noise suppression ability, we use a piece of spatially-homogenous BGO crystal as the specimen. Figure 5.4(b) shows power spectral density (PSD) plots of the transmitted signal (d), reference (x), the noise canceling output of the adaptive filter (e), along with the ADC noise floor and calculated shot noise limit. The adaptive filter (LMS) parameters were $L = 3, \mu = 0.2$. The PSD units are in decibels relative to the carrier (dBc), referenced to the DC power of the reference ($\propto 0.1225\ \mathrm{V}^2$). As can be seen from signal and reference PSDs, the ADC noise floor is about 15 dB above the shot noise limit and the laser RIN contributes an additional ~20 dB to the overall noise floor. A $1/f$ character of the RIN can be seen from DC to 1 MHz. Above 1 MHz, a gradual increase starts to appear, hitting a maximum at 8 MHz, which we attribute to the photodetector transimpedance amplifier[61]. Above 20 MHz, the noise from both signal and reference photodetectors converge to the ADC noise floor. When inspecting the PSD of the adaptive filter output e, the noise floor in the 1 MHz region has been decreased and now the 1 MHz pump-probe signal peak can be seen clearly. The total noise reduction in the vicinity of this signal is ~10 dB. This highlights that the electronic noise is currently the limiting factor, and that additional averaging is required to see a clear pump-probe image. We show later that averaging alone is not sufficient to recover a pump-probe image under these conditions (Figs. 6 and 7).

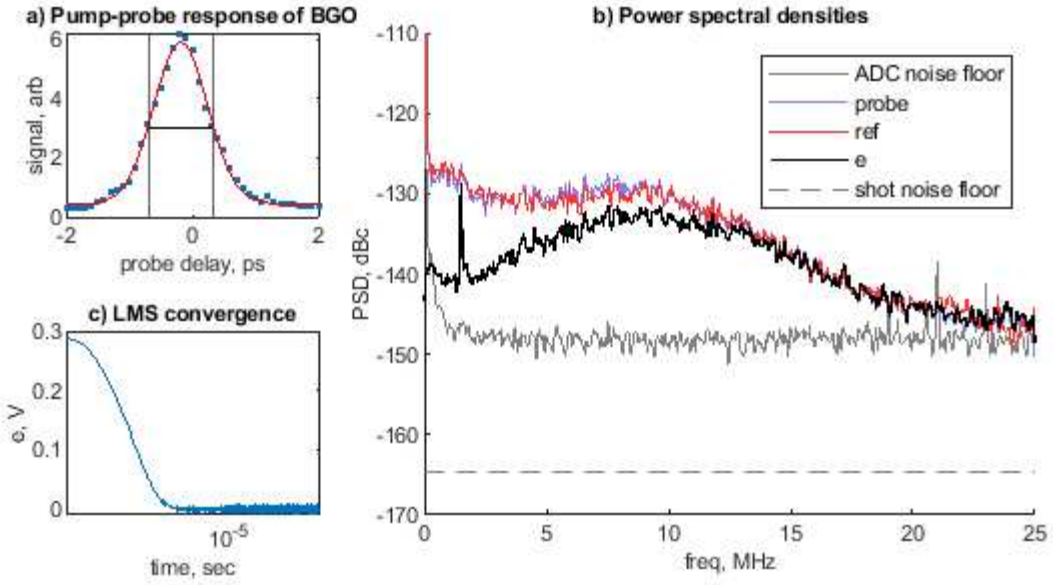

Figure 5.4: a) (blue dots) Measured pump-probe response of BGO at 530-nm pump, 490-nm probe, (red line) fit to Gaussian with 1 ps FWHM. (b) The measured PSDs of probe d, reference x, adaptive filter output e, and ADC noise floor are shown. Electronic noise floor is 24 dB above shot noise limit and ANC shows noise reduction around 1 MHz region. (c) The adaptive filter converges after 1 µs.

To test the imaging ability, we perform pump-probe imaging, with and without ANC, on BGO crystal particles. The specimen was prepared by crushing a fragment of BGO on a glass slide with a metal pick. Then a spacer was placed around the particles, with a coverslip on top. Images were acquired with 100x line repetitions. Yet, due to limited 16k data points buffer capacity of the DAQ, we could only record enough data for one scanning line at a time. Subsequent lines were acquired by stepping the sample stage in 1 µm increments. Given the 50 MHz sample rate (20 ns / sample)

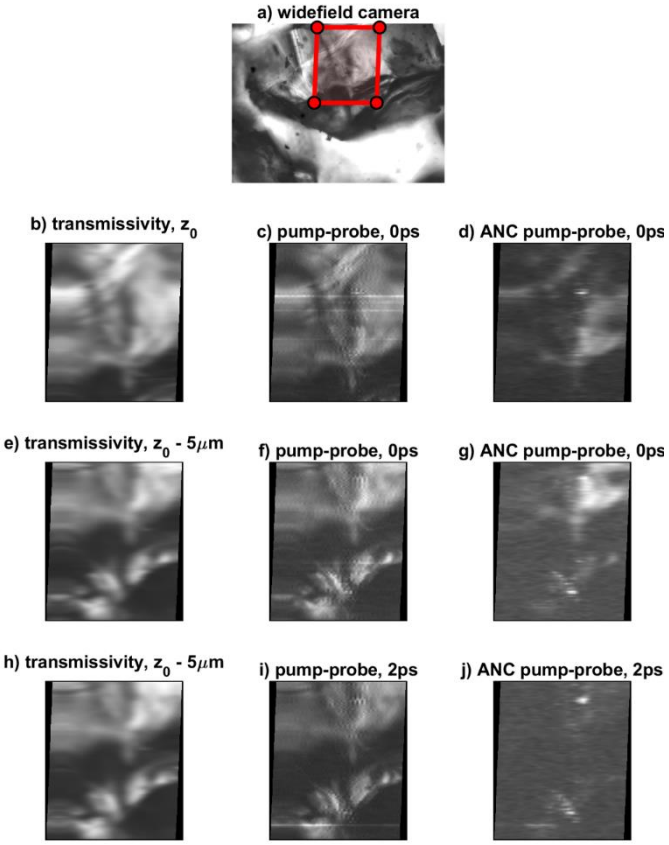

Figure 5.5: Imaging results. (a) The wide-field transmission image is shown on the top, with laser scanned area (70 μm × 100 μm) highlighted by the red box. (b) Laser-scan transmissivity, (c) lock-in output without ANC, and (d) lock-in output with ANC, at 0-ps pump-probe delay. (d) Laser-scan transmissivity, (e) lock-in output without ANC, and (f) lock-in output with ANC, for a z-section offset by 5 μm. (h) Laser-scan transmissivity, (i) lock-in output without ANC, and (j) lock-in output with ANC, for 2-ps pump-probe delay.

and 128x down sampling after the lock-in mixers, this 100x averaging is equivalent to a lock-in integration time constant of 256 μs. The field of view (FOV) is 75 μm ×100 μm. This process of acquiring one line at a time is admittedly time-consuming; fortunately, real-time adaptive noise cancellation can be done on an FPGA as we published in[62] and also shown in the next section. Results are shown in Fig. 5.5 and 5.6, comparing acquisition of pump-probe images with and without ANC. Without ANC, the signal recovered from the lock-in is strikingly similar to the linear transmissivity image; this is attributable to the broad-band nature of the fiber laser's RIN,

which extends into the pump modulation band. Note that only the ANC results exhibit the strong dependence of probe delay τ and optical sectioning, as expected for TAM.

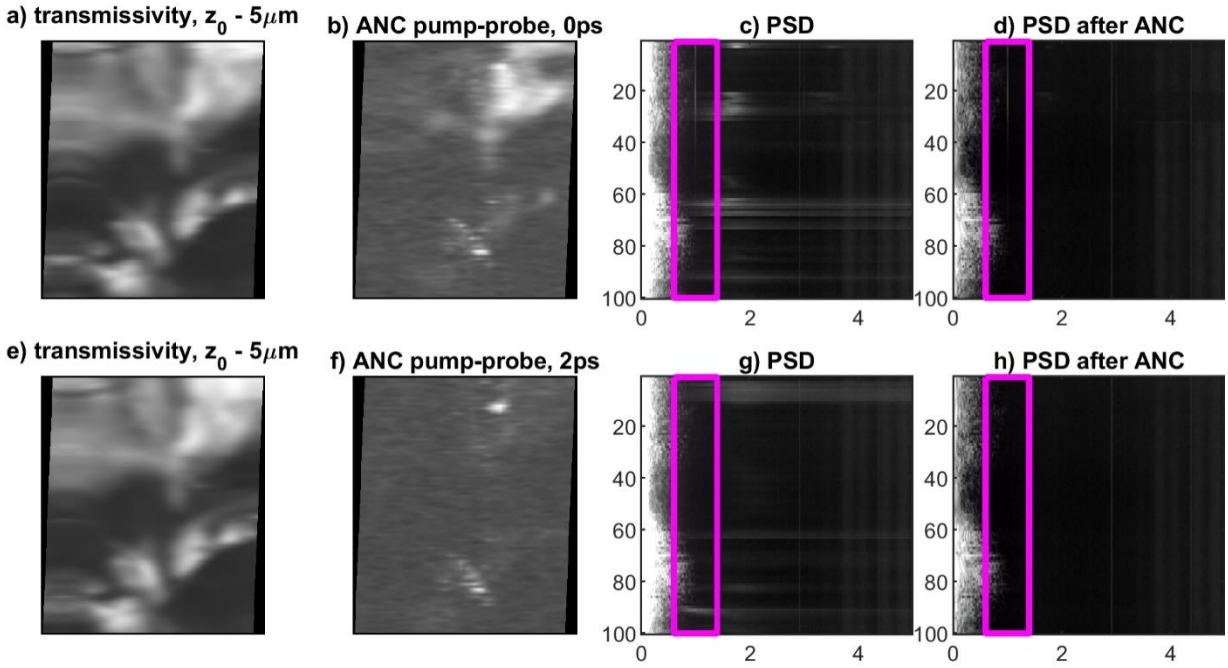

Figure 5.6: Imaging results along with power spectral densities of each scan line. (a) Laser-scan transmissivity, (b) lock-in output with ANC, (c) PSD without ANC, and d) PSD with ANC for 0-ps pump-probe delay. Note the pump-probe signal at 1 MHz in both PSDs. (e) Laser-scan transmissivity, (f) lock-in output with ANC, (g) PSD without ANC, and (h) PSD with ANC for 2-ps pump-probe delay. Note the absence of pump-probe signal at 1 MHz in both PSDs.

5.3.2 FPGA based adaptive filter results: electrophoresis gel of cytochrome

This Section is a modified form of my work previously published on Journal of Physical Chemistry B[2] [63].

The software-based adaptive filter has one obvious shortcoming: it cannot realize real-time noise canceling. Our group then wrote the adaptive filter algorithm into an FPGA board to build an FPGA-based adaptive filter device to conquer that obstacle[62]. That device is compatible with

[2] Section 5.3.2 has published on Journal of Physical Chemistry B.

commercialized LIA's, such as SRS and Moku LIA. Using the FPGA-based adaptive filter in accompanying an LIA and a DAQ, we achieved the real-time noise-canceling pump-probe signals from cytochrome electrophoresis gels.

The optical set up and the theory of pump-probe signal detection method is the same as that in Section 5.4.1. The only difference is that we substituted the previous software-based adaptive filter and software-based LIA with a FPGA board and a Moku LIA respectively. In that way, we do not need to store all the signal (d) and reference (x) data streams in advance for offline data processing. The new hardware-based approach can separate the pump-probe signal from RIN in real time.

During this experiment, the pump is modulated at 4MHz. The probe is detected by the signal photodetector and reference detector. The analog outputs of the signal photodetector (d) and the reference photodetector (x) are feed into analog-to-digital (ADC) channels of an FPGA board (Red Pitaya). The FPGA performs adaptive noise canceling and sends the output e through a digital-to-analog converter (DAC) in real time. The output is then passed through the Moku LIA to extract the phase-sensitive 4 MHz pump-probe signal. The ANC-enhanced pump-probe signal is then captured by a DAQ (National Instruments) operating at 10 kS/s.

System sensitivity investigation using cytochrome c solution: We investigated sensitivity limits of our transient absorption system by measuring a signal from successive dilutions of Cyt-*c*, in both redox forms.

Samples of Cyt-*c*-Fe^{3+} were prepared by dissolving 6.25 mg of Cyt-*c* powder (Sigma-Aldrich, 95% purity) in 1 mL of pH 7 buffer solution, resulting in an initial 0.5 mM concentration. A series of dilutions were prepared at 0.4, 0.3, 0.2, 0.1, 0.05, 0.01, and 0.005 mM. Cyt-*c*-Fe^{2+} at 0.5 mM was prepared by adding 174 mg of sodium hydrosulfide powder to 1 mL of 0.5 mM Cyt-*c*-Fe^{3+} solution. This resulted in a ratio of >10:1 sodium hydrosulfide to Cyt-*c* to ensure full reduction. Liquid

samples were loaded into a quartz cuvette with 0.1 mm path length and placed at the focus of the microscope objective for TAS measurements.

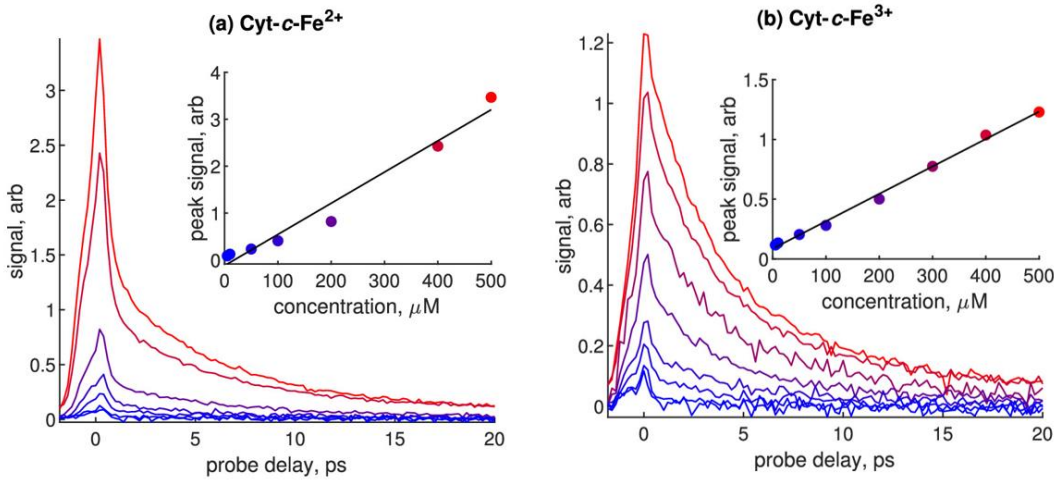

Figure 5.7. Concentration-dependent responses of (a) reduced and (b) oxidized cytochrome c. Insets show scaling of peak signal with respect to concentration compared to linear (black line). Color indicates concentrations from 0 (blue) to 500 μM (red).

Figure.5.7 shows the results. As before, there is a clear difference in excited-state lifetime between redox states. This contrast was absent in our previous results with high repetition rate pulses and a fixed (nonscanning) beam[57], likely because of the temperature sensitivity of the vibrational cooling (VC) processes in addition to the tendency of the methionine ligand to dissociate upon heating[64–66]. The fact that rapid scanning restores redox contrast is also consistent with experiments showing that flowing a liquid sample rapidly through the focal spot can minimize heating effects and bring high-repetition-rate measurements of nonlinear refractive index in line with low repetition-rate findings[67]. From the $\lambda_{\mathrm{pu}} = 530$ nm and $\lambda_{\mathrm{pr}} = 490$ nm signals in Figure 5.7, the most prominent difference between redox states is within the subpicosecond region. Cyt-c−Fe2+ has a narrower peak and roughly 3× the amplitude compared with Cyt-c−Fe3+. These results are consistent with previous 490 nm probe findings[56] [68] suggest that redox may be estimated from as few as two or three probe delays in an imaging scenario.

TA Measurements of WT and TAZ Gel Bands: Blue native polyacrylamide electrophoresis (BN-PAGE) gels of mitochondrial respiratory supercomplexes were prepared by Adam Chicco's lab (CSU). The different components of mouse mitochondria were separated and located at different positions of the gel by utilizing the gel electrophoresis technique. supercomplexes are known to show up as high molecular weight bands in a blue native electrophoresis[68,69]. Recently, the Chicco group published a study of these from healthy mice (WT) versus a mitochondrial disease model for Barth syndrome, deficient in a key molecule for stabilizing supercomplexes, Taffazzin (TAZ)[70]. A brief description of the supercomplex bands and their differences associated with Barth syndrome follows:

- Band I, ~900 kDa molecular weight (MW), contains a CI−CIII−CIV supercomplex and is found to be significantly diminished in TAZ versus WT. CIII contains both *c*- and *b*-type cytochromes, and CIV contains *a*-type cytochromes. In TAZ versus WT mice, band I exhibited a significant decrease in overall expression, in addition to a decrease in CIV content.
- Band II, ~880 kDa MW, contains a CI−CIII−CIV supercomplex, of different stoichiometries of CI, CIII, and CIV than band I. Band II heme composition is expected to be similar to band I, although the ratios between *a*-, *b*-, and *c*-type cytochromes may be different. Analyses form 2D gel electrophoresis suggest band II contains higher amounts of CIV than band I. [70]
- Band III, ~800 kDa MW, contains a CIV−CV supercomplex. CV lacks hemeproteins, and so the band III heme composition comes from the *a*-type cytochromes in CIV.
- Band IV, ~720 kDa MW, contains a CIII−CIV supercomplex; its heme composition is expected to be similar to band I.

- Band V, ~600 kDa MW, contains an undefined conglomerate of CII and CIV complexes. CII contains a *b*-type heme in addition to the *a*-type hemes found in CIV.

BN-PAGE uses a dye, Coomassie Blue, which is anionic when bound to protein and imparts a negative charge to the proteins, so that they can be separated by molecular weight under the Coulomb force of an applied electric field. Because the dye is a strong absorber, it can interfere with transient absorption measurements. The dye can be removed with a mildly acidic destaining solution, but this makes it more difficult to locate protein bands within the gel. Though we were able to locate the more intense protein bands in destained gels using the transient absorption signal alone[62], we found this impractical for the weaker bands. Therefore, for consistency, we chose to perform all measurements directly on the dye-stained samples and numerically unmix the hemeprotein and dye signals (see below). Here we characterize the transient absorption response of Coomassie Blue in both its protein-bound and free forms, as Coomassie Blue has an absorption spectrum that depends strongly on protein binding[71].

To characterize the possible impact of the dye on transient absorption measurements of hemeproteins, we also prepared gel fragments with Coomassie Blue by itself and Coomassie Blue bound to a mixed tissue homogenate (fetal sheep muscle) low in hemeproteins compared to isolated mitochondria. Figure 5.8(a) shows the TAS response of a bare electrophoresis gel incubated in a Coomassie Blue stain (red dot-dashed line) and a gel band of mixed protein bound to Coomassie Blue (solid blue line). The first case reports on the free dye, while the second case reports on the protein-bound dye. The TA signal from the free dye shows a short-lived increased probe absorption. By contrast, the TA signal from the protein-bound dye shows a biphasic pump–probe response with a positive peak at around 0 ps, a negative valley around 2 ps, and a transient

ground state bleach signal that persists >16 ps. This response is distinct from the typical heme response at these wavelengths.

Then we move to explore the transient absorption responses from five supercomplex bands cut from two WT gels and two TAZ gels. For each of the five supercomplex bands, five repetitions were recorded, denoised in MATLAB with first-degree polynomial local regression with weighted linear least-squares using the built-in command `smooth(x,'lowess',2)`, and then averaged. The resulting individual and averaged TAS decay curves are show in Figure 5.8(b). Each respiratory supercomplex band exhibits a transient absorption response at λ_{pu} = 530 nm and λ_{pr} = 490 nm. This indicates that at these wavelengths the transient absorption response from cells and [70,72,73][73] contains a mixture of contributions from type a, b, and c cytochromes. There is also a consistent shortening of transient lifetimes for the TAZ disease model, across all supercomplex bands. The disease-associated lifetime shortening is most apparent in band I – the same band that exhibits the greatest differences between WT and TAZ, in terms of both the amount of protein and composition of respiratory complexes. Next, we analyze the lifetimes of these response curves and

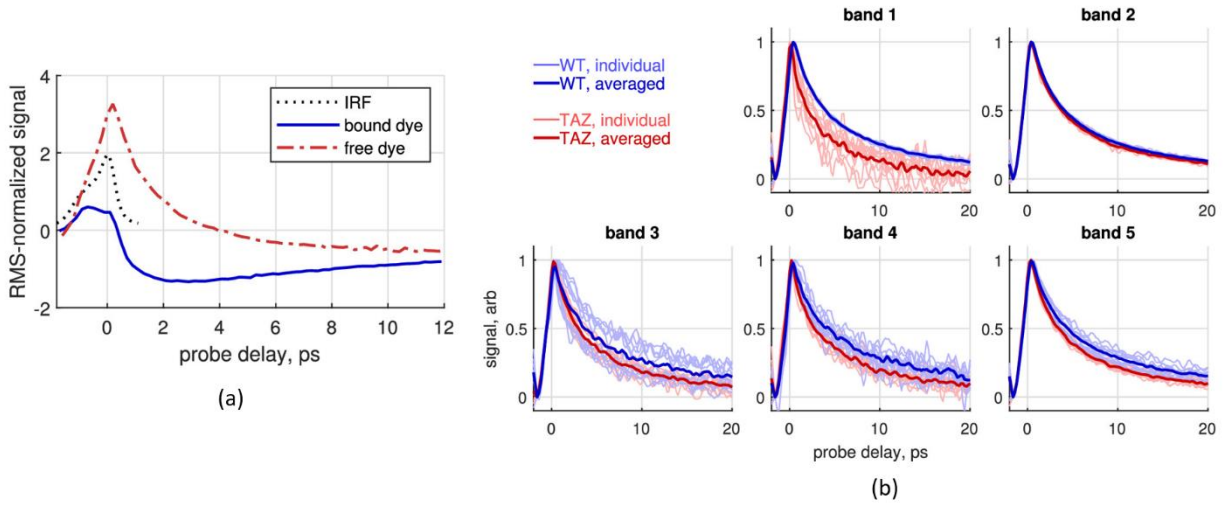

investigate possible artifacts from the Coomassie Blue dye.

Figure 5.8:(a) Transient absorption response of Coomassie Blue dye, in both protein-bound and free forms. The system impulse response function (IRF), as measured by nondegenerate two-

photon absorption in BGO, is shown for comparison. All signals are normalized by the RMS value. (b). Normalized mitochondrial gel transient absorption responses. Individual measurements are shown as thin lines, and averaged signals are shown as thick lines. WT in blue and TAZ disease model in red

Numerical Separation of Heme and Coomassie Blue: The signals for each band in Figure 5.8(b) should be understood as a linear superposition of the underlying heme response for that band's supercomplex and the Coomassie Blue dye. Here we investigate the extent to which the dye contributes to the overall measured lifetimes of the gel bands.

We treat each gel band separately as a two-component unmixing problem. Electrophoresis separates a mixture of proteins (or supercomplexes in this case) based on molecular weight. These cluster into distinct bands, each band containing many copies of a specific protein (or supercomplex). The bands then may be cut out of the gel, and the proteins eluted, as a method commonly used for separating and purifying proteins from a complex biological sample[74]. For example, in the scenario at hand, WT band I is populated with many copies of a CI–CIII–CIV supercomplex having ~900 kDa MW, each having the same composition of heme–porphyrins embedded in the same molecular environment. Therefore, each of the CI–CIII–CIV supercomplexes that makes up WT band I has the same transient absorption response (one component). The other component comes from the Coomassie Blue dye in its protein-bound state, which imparts the charge needed for electrophoretic separation. This dye response is known; however, the TAS response of each band's supercomplex is unknown, and the proportion between dye and supercomplex signals is unknown. Thus, for each band, we have a two-component unmixing problem, with one component known (TAS response of the protein-bound dye) and one component unknown (TAS response of the supercomplex found in the band). The forward mixing problem can be written as a matrix product

$$Y = MX$$

where X represents the underlying heme and dye response curves, M represents the proportions of the underlying sources found in the measurements, and Y is the measured response curves. In this case, Y (the measurements themselves) is known in addition to one row of X (Coomassie Blue's measured response). The goal is to find the mixing matrix M and the remaining rows of X (the underlying heme contributions).

The standard methods for solving this problem all make assumptions that do not apply to this scenario. Principal component analysis (PCA) can be used to find X such that each component is orthogonal, but the multiexponential nature of the heme and dye signals makes them inherently nonorthogonal. Non-negative matrix factorization (NNMF) can be used to find a solution such that the elements of both M and X are non-negative, but the dye's signal is primarily a ground-state bleach, and its row of X will be mostly negative. Independent component analysis (ICA) searches for a set of components X such that their mixing coefficients (columns of M) are statistically independent, but the amounts of dye and heme for each measurement are both in proportion to the protein concentration and will be statistically correlated.

Therefore, we tailored an approach based on the alternating least-squares form of multivariate curve resolution (MCR-[75]) [76–78]which takes into account the assumptions we can make about this data set. Specifically, (a) one of the rows of X is the measured dye response and (b) the mixing matrix M must be non-negative. See Appendix A.4 for details.

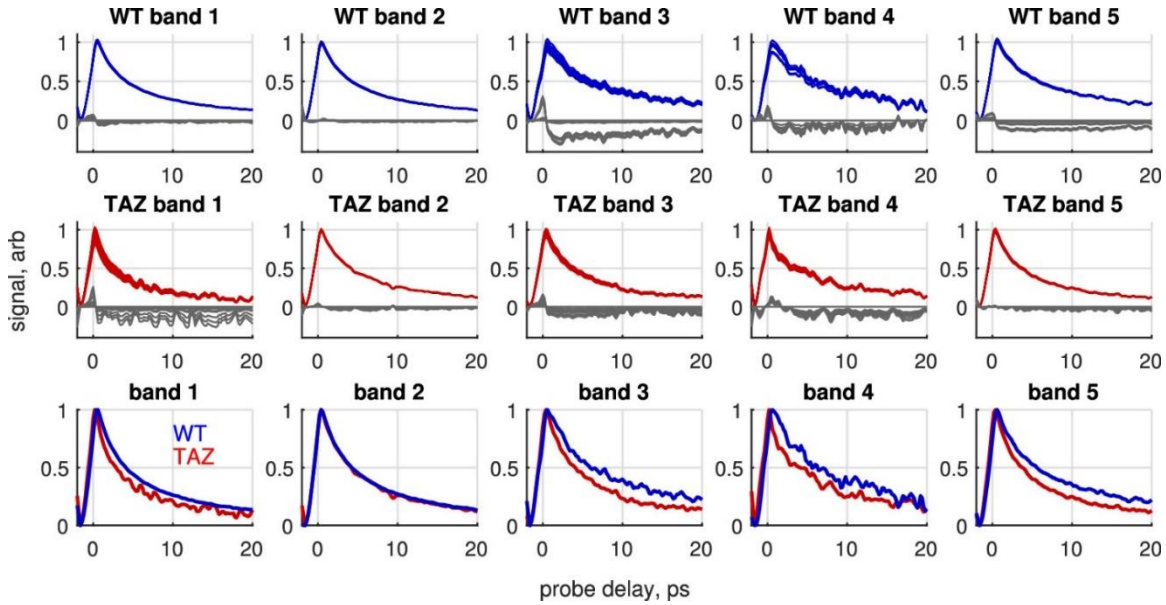

Figure 5.9. MCR two-source recovery results for mitochondrial gel band TA curves. WT heme signals are in blue, TAZ heme signals in red, Coomassie Blue dye signals in gray. Bottom row compares WT vs TAZ for each band.

The MCR results for each band from WT and TAZ gels are shown in Figure 5.9. The recovered x_1 responses are similar to that of Cyt-*c*–Fe3+ (see Figure 5.7(b)), while x_2 resembles the shape of the protein-bound dye (see Figure 5.8(a) , solid blue line). From this analysis, the dye appears to have a peak amplitude of at most 20% of the heme signals. The largest dye contributions come from the WT samples. Subtracting the dye from these hemeprotein signals results in an increased lifetime for WT bands, further increasing the differences between WT and TAZ transient absorption signals. A comparison of WT vs TAZ responses for each band is shown in the bottom row of Figure 5.9.

Lifetime Analysis: To quantify the time constants of these signals, we fit the data with a multiexponential model, accounting for the instrument response function (IRF) and an instantaneous component to account for processes that are faster than the IRF such as nondegenerate two-photon absorption (2PA). The IRF was modeled as a superposition of two

Gaussian functions. The convolution of this IRF and the multiexponential function, plus an instantaneous component, is (see ref[79])

$$a_0 \sum_{i=1}^{2} b_i e^{-\frac{(t-\mu_i)^2}{\sigma_1^2}} + \sum_{i=1}^{2}\sum_{j=1}^{m} \frac{a_j b_i}{2} e^{\left\{-\frac{t}{\tau_j}\right\}} \exp\left[\frac{1}{\tau_j}\left(\mu_i + \frac{\sigma_i^2}{2\tau_j}\right)\right] \times \left\{1 + \operatorname{erf}\left[\frac{t - (\mu_i + \sigma_i^2)}{\sqrt{2}\sigma_i}\right]\right\}$$

where $b_i, \mu_i,$ and σ_i indicate the amplitudes, time locations, and standard deviations for the IRF Gaussian functions, a_j and τ_j are the amplitudes and time constants of the exponential terms, and a_0 is the amplitude of the instantaneous component. The number of exponential components m was determined by comparing $m = 1,2,3$ fits with an Akaike information criterion (AIC) [75]

$$\mathrm{AIC} = n_\tau \log \mathrm{MSE} + 2k$$

Where n_τ is the number of probe delays measured, MSE is the mean-squared error, and the number of unknowns is $k = 2m + 3$, accounting for exponential amplitudes and time constants, instantaneous component amplitude, an overall time offset, and baseline. Fitting was performed first by using the MultiStart algorithm (MATLAB, Global Optimization Toolbox) with 500 start points. The resulting batch of results was averaged and then fed through nonlinear least-squares fitting (MATLAB, Optimization Toolbox) to calculate confidence intervals. For both Cyt-*c*–Fe^{2+} and Cyt-*c*–Fe^{3+}, the best AIC was obtained with the biexponential ($m = 2$) model. Fitting results are summarized in Table 1. Cyt-*c*–Fe^{2+} exhibits a larger relative contribution from instantaneous (i.e., faster than our 0.8 ps IRF) processes and has a ligand recombination time in the range previously measured by kilohertz transient absorption[58]. The remaining τ components for both redox states are attributable to VC. However, a comparison between these VC lifetimes and the higher-order multiexponential model of ref [58] cannot be directly made because our data, coming from only a single probe wavelength, supports only a biexponential model. Nonetheless, each of

the VC times found with our data lands in the center of the nearest VC times in ref[58] However, we note that VC is inherently nonexponential[64,65], and these numbers are presented only to give a sense of the time scales involved. Even at the lowest concentration tested, 5 μM, a TA signal near 0 ps probe delay can be observed for both redox states. This is 2 orders of magnitude below the 0.5 mM physiological concentration in [80,81].

Table 1. Multiexponential Fitting Results for 0.5 mM Cyt-c TA Responses Comparing Ligand Recombination Times τ_r, Vibrational Cooling Times τ_c' and τ_c'', and Ratio of Nondegenerate Two-Photon Absorption Amplitude to Noninstantaneous Component Amplitudes $a_0/(a_1+a_2)$.

	Cyt-c-Fe2+ Ours	Ref[58]	Cyt-c-Fe2+ Ours	Ref [58]
τ_r, ps	6.4 ± 0.82	5.9 ± 0.1		
τ_c', ps	0.90 ± 0.047	0.60 ± 0.07	2.4 ± 0.70	0.70 ± 0.09
		1.8 ± 0.05		3.4 ± 0.3
τ_c'', ps			6.7 ± 2.9	3.4 ± 0.3
				11 ± 2.0
$a_0/(a_1 + a_2)$	3.1		1.6	

Of greater interest, though, is the minimum detectable change in redox of a Cyt-c pool. To estimate redox sensitivity, we synthesize random noisy mixtures Y of Cyt-c–Fe^{2+} and Cyt-c–Fe^{3+}using the fitted function from 0.5 mM to form the two columns of a basis matrix X with added Gaussian noise σ to match the measurement noise

$$\boldsymbol{Y} = \boldsymbol{XM} + \sigma$$

where **M** is a randomly generated mixing matrix. The first row, m_1, is drawn from a random uniform $U(0,1)$ distribution, representing the fraction of Cyt-c–Fe^{2+}, while the second row, $m_2 = 1 - m_1$, represents the fraction of Cyt-c–Fe^{3+}. Then we compute an estimated mixing matrix $\widehat{\boldsymbol{M}}$ by solving the following equation with the `mldivide()` function (MATLAB):

$$\boldsymbol{Y} = \boldsymbol{X}\,\widehat{\boldsymbol{M}}$$

The error in estimating redox is then reported as the root-mean-squared (RMS) difference between $\boldsymbol{M}$ and $\widehat{\boldsymbol{M}}$. For noise levels matching the T = 200 ms integration time used to acquire the above data, the redox estimation RMS error is 0.4%. Physiological variations in respiratory chain redox are at most 10%[80]. By scaling the noise $\sigma \propto 1/T$, we find that the redox estimation error hits this 10% limit at $T = 0.3$ ms integration time.

The strong dependence of heme TAS on vibrational cooling explains why early high-repetition-rate experiments on Cyt-*c* with a static beam lacked redox contrast,[72] which is restored here by rapidly scanning the beam so as to prevent excessive heating at the focal spot. On our fiber-laser-based transient absorption spectrometer, we have demonstrated sensitivity down to 5 μM. We estimate this translates to the ability to detect a 0.4% change in redox at typical 0.5 mM physiological concentrations[82] using a 200 ms integration time. We also presented the first TAS measurements on respiratory hemes in their native supercomplexes, separated and embedded in electrophoresis gels. Given that each of the supercomplex bands, even those lacking Cyt-c, yielded a similar TAS signature typical of hemes, we conclude that at the current $\lambda_{\mathrm{pu}} = 530$ nm and $\lambda_{\mathrm{pr}} = 490$ nm, the signal we observed previously in TAM imaging[42,72] likely originated from a mixture of *a*-, *b*-, and *c*-type respiratory chain hemeproteins. Though redox contrast at these pump/probe wavelengths was strong, the lifetime differences between different respiratory hemes in the gel, which are fully oxidized, remained subtle. Therefore, though the$\lambda_{\mathrm{pu}} = 530$ nm, $\lambda_{\mathrm{pr}} = 490$ nm probe suffices for redox contrast, other wavelengths will need to be found for resolving individual respiratory hemes. When comparing healthy (WT) versus the Barth syndrome disease model (TAZ), we found that TAZ respiratory hemes tended to exhibit faster transient relaxation, which can be seen in the raw data and is more pronounced after numerically subtracting the

background Coomassie Blue dye signal. This disease-associated lifetime shortening was the most pronounced for band I, which was the band previously found to exhibit the greatest differences in protein amount and composition between WT and TAZ. A possible explanation for the lifetime contrast between WT and TAZ might be from effects of cardiolipin (CL). The TAZ model of Barth syndrome lacks tafazzin, a molecule that stabilizes the formation of CL, leading the TAZ mitochondrial membranes to have less CL than WT. When bound to Cyt-*c*, CL is known to cause partial unfolding,[83] [84] detachment of the axial methionine ligand, and thus conversion to a 5-coordinate heme. CL-induced unfolding of Cyt-*c* is also known to result in longer excited-state lifetimes[85] on picosecond time scales. Therefore, the samples from the WT model may have a larger population of partially unfolded Cyt-*c*-CL, which could explain its overall longer lifetimes. Altogether, this disease-associated lifetime shortening suggests that with TAS and TAM it might be possible in the future to detect the underlying CL deficiency in Barth syndrome and monitor efforts to restore CL in patients. Further investigation at other pump and probe wavelengths may reveal other disease-associated changes in TAS related to mitochondrial defects.

Chapter 6. Redox-dependent TAM cytochrome imaging based on solid state laser source

This chapter is a reformatted and expanded version of my work published in Biomedical Optics Express[3] [86].

6.1 Introduction

Hemeproteins are not fluorescent; to make use of hemes for imaging contrast requires techniques based on detecting absorption, like photothermal, photoacoustic, and TAM imaging. TAM offers improved chemical specificity because of its ability to detect ultrafast dynamics based on time-resolved absorption changes.

Below is a brief introduction to the current hemeprotein imaging methods.

Yasuda et al.[87,88] utilized the Raman effect to extract cytochrome distribution in Aspergillus nidulans hyphae. Raster-scanning was realized by scanning the sample stage. Multivariate curve resolution (MCR), which will be discussed later, was used to determine the relative contribution of cytochrome *c* to each pixel's spectrum. Moreover, because the reduced and oxidized cytochrome have different characteristic Raman spectra, such a method can differentiate the cytochrome's redox states and show redox level differences among various hyphae regions. However, such an approach requires recording the entire Raman spectrum at each measurement point; therefore, the shortest pixel dwell time is 1s.

[3] Chapter 6 has been published in Biomedical Optics Express.

Lu et al. [89] employed photothermal microscopy to achieve cytochrome imaging in live cells. A 200 μs pixel dwell time was realized by utilizing galvo scanning mirrors. Unlike conventional photothermal imaging that used one-photon linear absorption of the laser beam to induce local heating, they utilized two-photon nonlinear excitation from a near-infrared (NIR) ultrafast laser as the heating source. Such an excitation scheme enhances the optical sectioning ability, increases the penetration depth, and reaches the heme proteins' intense Soret absorption band.

Zhang et al.[90] detected acoustic waves excited by absorption of laser pulses (label-free photoacoustic microscopy) of cytochromes in the cytoplasm from fixed fibroblasts, based on Soret absorption peak (420nm) of hemeproteins. They also confirmed that *a*-, *b*-, and *c*-type cytochromes are the main absorbers they detected in fibroblast cells, through analysis of the photoacoustic spectra. However, neither the photothermal nor photoacoustic technique has shown the ability to image changes in mitochondrial redox.

At the same time, transient absorption imaging, i.e., TAM, has been used to distinguish hemoglobin from its glycated form found in diabetics[91], oxy- versus deoxy-hemoglobin[92–94], hemoglobin versus hemozoin in plasmodium (malaria)-infected red blood cells[95], and to track heme storage and transport in *C. elegans*[96]. As for our contributions to hemeprotein TAM, a clear spectroscopic redox contrast in cytochrome *c* solution has already been shown in Section 5.3, indicating it should be possible to use TAM to form redox images of hemeproteins. Yet two challenges remain: signal-to-noise ratio (SNR) and the choice of optimal pump and probe wavelengths. As mentioned in Chapter 5, even though the adaptive noise canceling method can lower the fiber laser's RIN up to 10 dB, we still need to mitigate another 25 dB to reach the shot-noise limit. Here, we used instead a solid-state laser (Insight X3, Spectra-Physics), which, unlike

a fiber-based laser, has RIN that is limited to lower frequencies. Thus we can overcome RIN simply by modulating the pump at a frequency above the characteristic RIN of this laser.

As mentioned in Section 1.2, much effort has been devoted to shorter pulse generation to increase pump-probe microscopy's temporal resolution. Instead of exploring a method to give us better temporal resolution, our goal is to explore an ideal pump wavelength and probe wavelength that will provide us with better contrast between reduced and oxidized cytochromes. Majed Chergui's group has studied the transient absorption spectra of reduced and oxidized cytochrome with probe wavelengths covering the entire visible range [56,58]. For the pump, they compared both UV and a 530 nm. Figure 6.1 shows their results with the visible-wavelength 530 nm pump. The blue dashed arrow labels our probe wavelength. Note that by tracing the time-course of 490 nm probe absorption in Fig. 6.1, one can observe faster relaxation for Cyt-*c*-Fe^{2+} compared with Cyt-*c*-Fe^{3+}, in agreement with our results in Chapter 5.

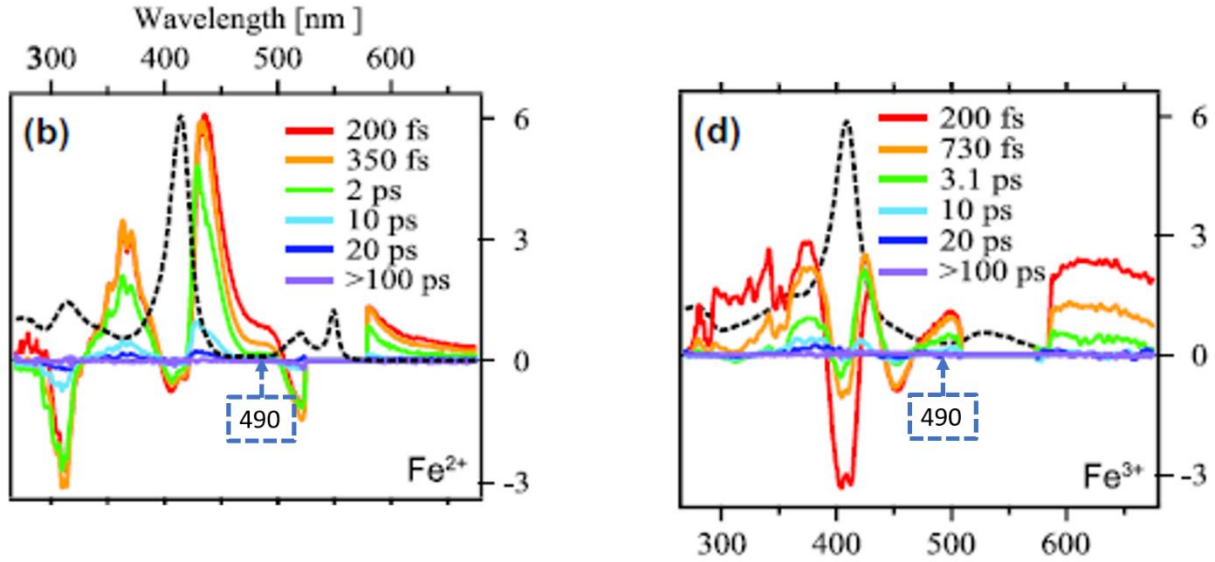

Figure 6.1: Transient absorption spectra after 530nm pump photon absorption. The left panel shows a reduced cytochrome c solution. The right panel shows the oxidized cytochrome c solution. Figure reproduced from [58].

Nevertheless, one should also notice that the current 490 nm probe does not provide the best redox contrast. For instance, if we choose a 450 nm probe wavelength, we will see a decay curve that starts with a positive value and ends with a zero value in reduced form. On the contrary, we will see a curve that increases from an initial negative value to zero in oxidized form. Therefore, if we build a pump-probe microscope that allows us to have a tunable pump and tunable probe wavelength across the entire visible range, we will better differentiate reduced and oxidized cytochromes. The next step is to build another pump-probe microscope with a tunable pump wavelength and tunable probe wavelength using the Insight X3 laser source. This laser source has RIN that falls below the shot noise floor in the MHz region, one fixed IR output (1045 nm) and a tunable output with wavelength range from 680 nm to 1300 nm. Direct frequency doubling of the two outputs allows us to have a 522 nm pump and a 340 nm to 650 nm tunable probe. This chapter will focus on imaging with varying probe wavelengths; the next chapter will present preliminary efforts at a tunable pump with supercontinuum generation from a segment of photonic crystal fiber (PCF).

6.2 TAM with 520nm pump and visible tunable probe.

Before building the tunable pump arm, we created a TAM with fixed 520nm pump and a visible tunable probe to explore which probe wavelength would offer us the best hemeprotein redox contrast. Previously, our lab reported spectroscopy of cytochrome c and label-free TAM imaging of cryosectioned tissue at 530nm pump (an absorption peak of oxidized, Fe3+, cytochrome c) and 490nm probe with a fiber laser source, in addition to TAS of respiratory chain supercomplexes showing excited-state lifetime differences corresponding to mitochondrial disease[63,72]. Here, we frequency-doubled the fundamental (1040nm) to produce a 520nm pump (an absorption peak of reduced, Fe^{2+} cytochrome *c*). We frequency-double the tunable output of the X3 to produce a

probe at 450nm, 490nm, and 620nm. These are selected to maximize contrast by considering the TA response of cytochrome c (see Fig. 6.1): 450nm results in a signal that is of the opposite sign for reduced (ground state bleach) and oxidized (excited-state / hot band absorption); 620nm results in a cyt *c* signal that is significantly larger than that at 450nm or 490nm, for the oxidized state and has a more pronounced lifetime difference between reduced and oxidized states. That is, of course, an approximate starting point, as the TA response of mitochondria will need to consider all of the respiratory chain hemeproteins and account for the likelihood that the TA responses of these hemeproteins will be different in isolation versus in their native molecular environment within the inner mitochondrial membrane. TAM imaging experiments were conducted on fresh reduced and oxidized muscle fiber preparations. The reduced preparations are achieved by the addition of mitochondrial fuels to oxidized mitochondria. The picosecond-timescale change in probe absorptivity after pumping shows an excited state lifetime difference between two mitochondrial redox states. Applying multivariate curve resolution (MCR) to muscle tissues' TA image stacks reveals pixel-wise lifetime differences among mitochondria within muscle fibers. The most substantial redox contrast comes from a 620nm probe. The realization of TA images from live tissue with hemeprotein redox contrast takes us one step closer to applications, for example, in cancer metabolism and noninvasive evaluation of mitochondrial diseases.

6.2.1 Experiment set up

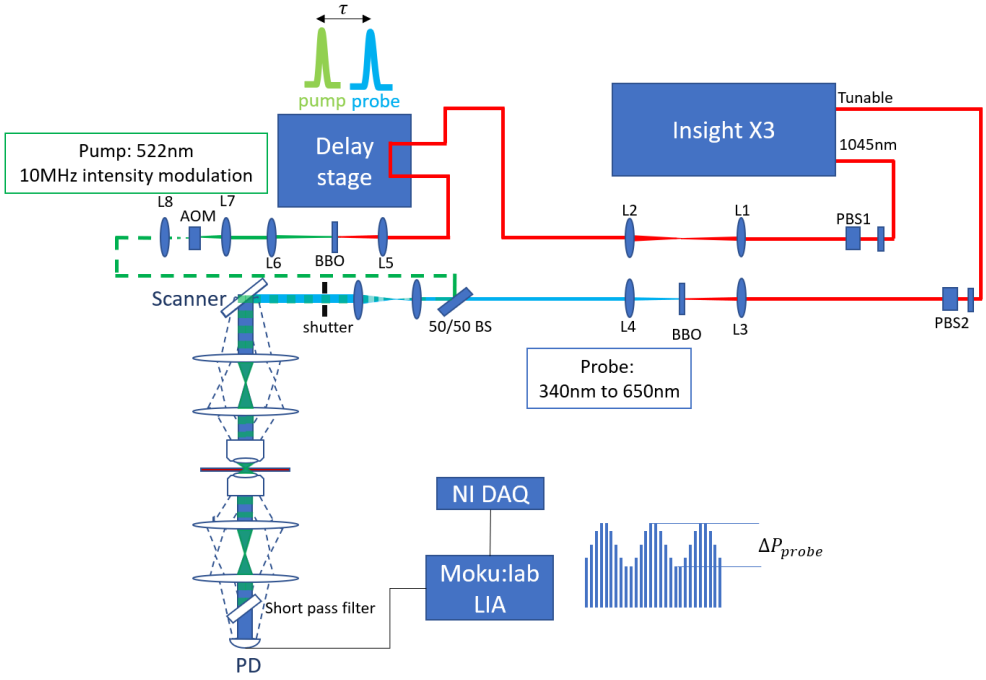

Figure 6.2: TAM with solid state laser source. The fixed 1045nm output is frequency doubled to 522nm pump. The tunable IR output is frequency doubled to visible probe, The probe wavelength tunability covers the entire visible spectrum. AOM: acoustic optical modulator. PD: single pixel photodetector. PBS: polarization beam splitter. BS: beam splitter. BBO: frequency double beta barium borate crystal

Our TAM imaging system is based on an Insight X3 ultrafast laser source (80 MHz repetition rate, ~100fs pulse width), with each output frequency doubled in a BBO crystal (0.5mm thickness, Type I phase matching, EKSMA BBO-651H) to provide a visible-wavelength pump/probe pulse pair. The fixed 1045 nm output is frequency-doubled to produce a 522 nm pump beam. The tunable (680nm—1300nm) output is frequency-doubled to produce a visible probe beam tunable from 340 nm to 650 nm. After frequency doubling, the 522 nm pump beam and the tunable visible probe beam are combined by a 50/50 beam splitter (used instead of a dichroic because the tunable probe arm can be longer or shorter wavelength than the 522nm pump). The two collinear beams are then expanded from 1mm diameter to 10mm diameter through a telescope and directed to the resonant

LSM, which has been described in section 5.1. Then the transmitted probe laser is detected by a detection system, consisting of a photodetector (Thorlabs SM05PD1B), a 50 Ω pass through terminator, a 1MHz high pass filter, a 20MHz low pass filter, and a low noise pre-amplifier (Edmund Optics 59-179). The high pass and low pass filter combination blocks the significant DC component and limits the aliasing outside 1MHz to 20MHz. Finally, the pump-induced changes in probe transmissivity $\Delta P_{\mathrm{pr}}(\tau)$ are then detected with a lock-in amplifier (LIA, Moku:lab).

A motorized delay stage controls the pump-probe time delay τ. The pump laser pulse train is intensity modulated at 10 MHz by an acoustic, optical modulator (AOM, TEM-100-25, Brimrose) to ensure several on/off pump modulation cycles per pixel (the 3.5 kHz line rate, at 516-pixels per line, results in a pixel dwell time of 277 ns).

At each τ, we acquire TA image data with the scanning LSM for 5 seconds, equivalent to 10 frames. A shutter blocks the beam between acquisitions to minimize exposure to light when changing τ. The data acquisition device (DAQ, NI PXI-6133 simultaneously records the scanner x position, y position, and the LIA in-phase output (proportional to $\Delta P_{\mathrm{pr}}(\tau)$. Pump-probe signal levels over the scan region were compared before and after each stack. Any image stacks with a noticeable average signal drop (either from photobleaching of the hemes or from z-drift of the sample) were discarded. For each 10-second acquisition, the time-domain data were then reconstructed into an image with isotropic 1 μm^2 pixels with `gridfit()`, a regularized grid fitting function[97]. The phase shift between the x position and the acquired signal was fine-tuned by applying linear spectral phase to the acquired signal, adjusting the slope to maximize the standard deviation of the reconstructed images (during this adjustment, `gridbin()` was used to speed up reconstruction[98]; final reconstruction was done with `gridfit()`).

Laser power used was 24mW for the 522nm pump, 17mW for the 450nm probe, 53mW for the 490nm probe, and 24.5mW for the 620nm probe. Except for 450nm, which was attenuated to prevent photobleaching, these were set to the maximum available out of the frequency-doubling stages. While further study is needed to understand the impact of ultrafast pulses on cell damage, we note that a recent detailed study on damage in LSM with ultrafast 1040nm pulses by Talone et al. [99] found phototoxicity to be dependent on average power P, the number of lines L scanned over a $2500\ \mu m^2$ area, and scanning speed V_s, where $x = P[\mathrm{W}] \times L \times V_s[\mathrm{mm/s}]^{-0.08} < 5.367$ resulted in minimal photodamage (<5% probability of cell death). Adjusting this for the larger area over which the laser exposure is spread out in our scenario, $0.2975\ \mathrm{mm}^2$, a factor of 119 larger, results in $x' = x \times (2500\ \mu m^2)\ /\ \mathrm{FOV} = x/119$. With 5 sec acquisition time and a 3.5 kHz line rate for the delay stacks, $L = 35{,}000$. Our worst-case scenario (77 mW total power) is then $x = 1 \times 10^{-3}$, three orders of magnitude within Talone's $\lambda = 1040\mathrm{nm}$ safety limit. However, this rule of thumb does not account for increased absorption and heating of hemeproteins at shorter wavelengths. For example, we noted that at 450nm probe, >17mW ($x = 1.8 \times 10^{-3}$) caused photobleaching of the TA signal (hemeproteins absorb significantly more energy at 450nm due to the strong Soret band, thus increasing local heating). Further studies on ultrafast pulse phototoxicity are needed to discover the wavelength dependence of the phototoxicity parameter x.

6.2.2 SNR measurement

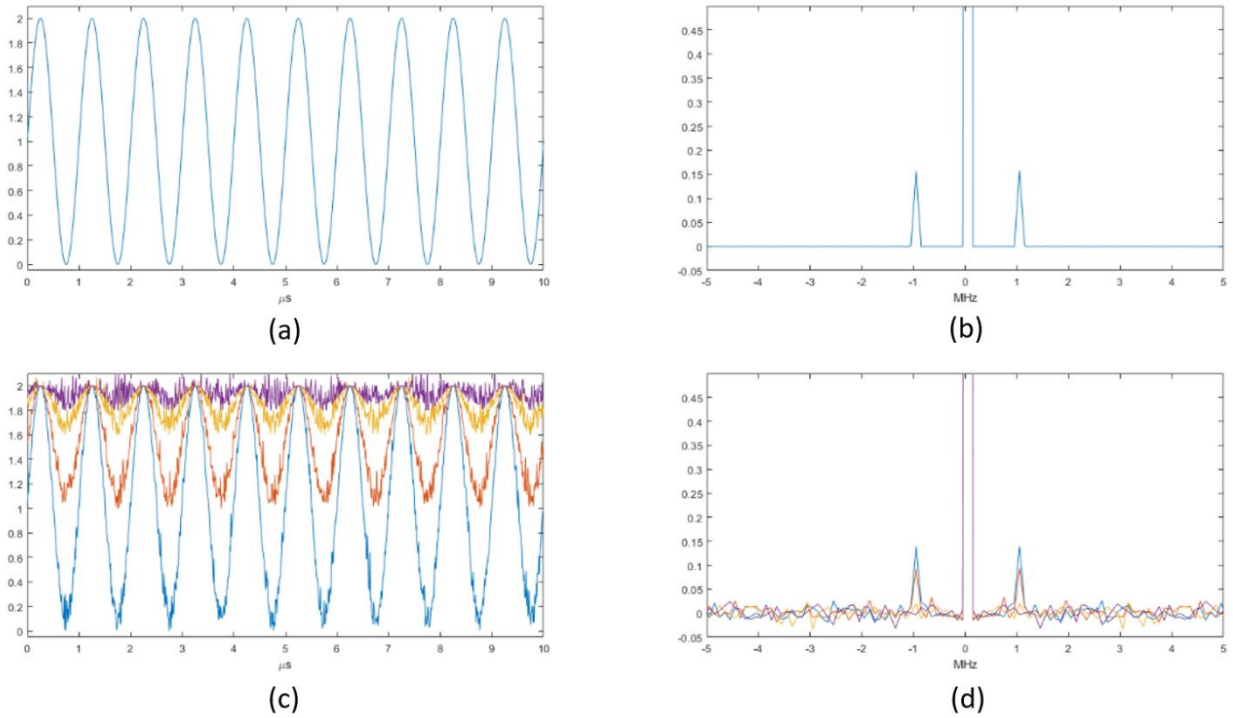

Figure 6.3: TA signal in time and frequency domain with added Poisson noise. a) and c) clean TA signal and TA signal with Poisson noise in the time domain. B) and d) clean TA signal and TA signal with Poisson noise in the frequency domain. If the TA signal is lower than the shot noise, it can be buried underneath the Poisson noise in the frequency domain.

The TA signal, before the LIA, takes the form of a sinusoidal wave, $\Delta P(\tau) \times \cos(\omega t)$. In the previous TAM with a fiber laser source, laser intensity fluctuations (RIN) on both pump arm and probe arm contribute equally to the noise. Here, with the solid-state laser source, we only need to consider the shot noise of the PD and electronic noise from other components of the detection system, because both pump RIN and probe RIN are smaller than the shot-noise. Figure 6.3 compares sine waves of varying modulation depths (the pump-probe ΔP signal) in the absence and presence of simulated shot noise, drawn from a Poisson distribution, along with Fourier transform spectra. Figure 6.3(d) shows the that, although shot noise covers the entire frequency spectrum and cannot be fully separated from the signal ΔP in the lock-in detection band, the majority of the shot noise can be rejected by restricting detection bandwidth.

However, since the scanning speed is 3m/s, it is crucial to maintain a large detection bandwidth to reserve fine sample structures. Thus, we choose the 1MHz LIA detection bandwidth, which offers a 277 ns pixel dwell time. We later use signal averaging to further suppress noise by a factor of $\sqrt{n}$, where n is the number of replicate measurements.

We use a home-built detection system to detect transmitted probe light. To test the SNR, the Moku:lab is used as a spectral analyzer to read out the probe laser's power spectrum density (PSD). With the delay stage set to 0 ps, pump laser modulated at 10 MHz with a square, 3.5 kHz mirror scanner to the minimum scanning range (75 μm line scanning), we recorded the transmitted probe laser power spectrum density (PSD) with the TA signal from a homogeneous BGO crystal, shown in blue in Fig.6.4(a). One can observe the 10 MHz signal and its harmonics originating from square wave modulation. The electronic noise of the detection system, shown as the orange curve, is measured by turning off the probe laser. The fact that the noise floor is the same in both measurements implies that the current detection system does not allow us to reach the shot-noise limit.

In the future, this might be obtainable with a resonance amplified photodiode detector (RA-PD), such as offered commercially by VibroniX. Figure 6.4(b) shows the difference between PSD with both pump and probe on and without any laser passing through the system. The TA signal at 10MHz is 45dB larger than the adjacent electronic noise floor. One last thing that we can learn

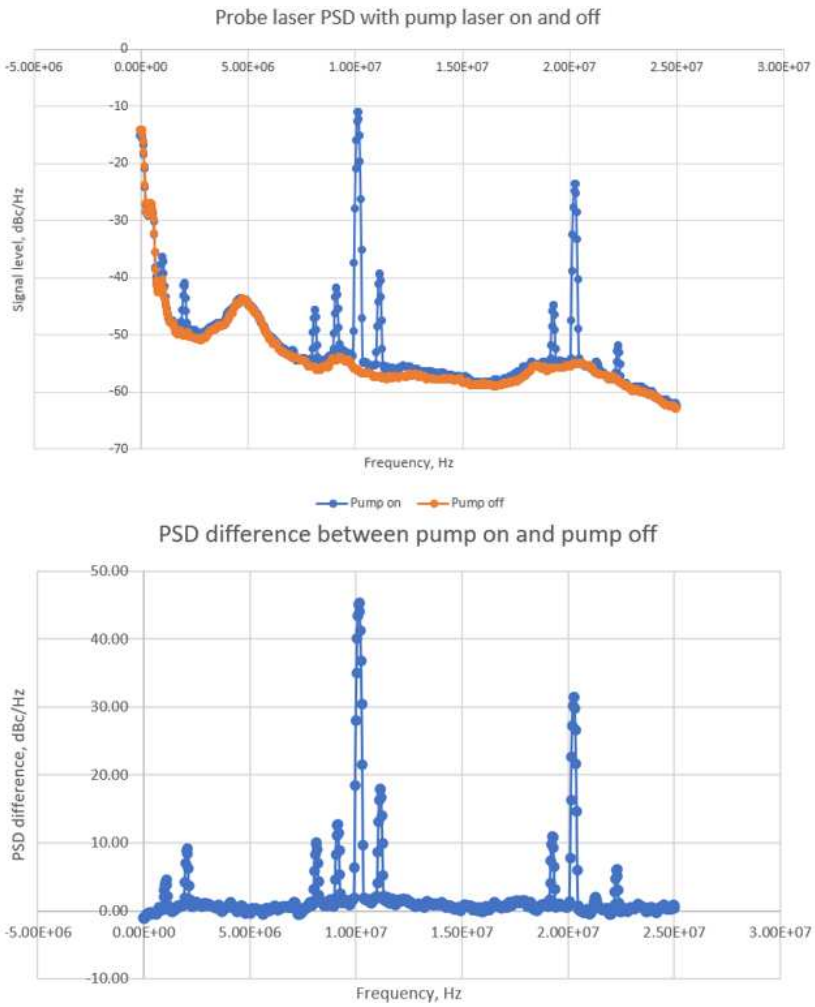

Figure 6.4: a) power spectrum density of probe laser with pump laser modulation turned on and turned off. Both pump and probe focus on the BGO crystal with two-photon absorption signals at the pump modulation frequency. As can be seen, the 1MHz signal and its harmonics only appear when 1MHz pump modulation is turned on. b) Subtraction of the two curves in a) gives us a flat noise floor and a clear SNR.

from Fig. 6.4 (b) is that the modulation harmonics fall within the detector response, and might lead us to a higher resolution. In this example, the harmonics arise from the square pump modulation, but in cases where a pure sine wave modulation is applied, and pump nonlinearities (such as saturation) produce harmonics in the sample[100], these might be used for super-resolution with the help of the Structured Illumination Microscopic (SIM) technique. The idea of utilizing comb filtering and higher harmonics signal to achieve high-resolution image has been applied to ultrasound photoacoustic imaging[101–104]. High-resolution wide-field fluorescence imaging has

also been realized by combining SIM with harmonics signals generated from saturated fluorescence emission. As long as all the harmonics peaks can be simultaneously detected with a multi-frequency lock-in[105] , the resolution is limited only by SNR [106].

6.2.3 Sample preparation

Samples were prepared in the Chicco lab from skeletal muscles of adult (6-8 month old) C57Bl/6N mice (Jackson Labs, Bar Harbor, ME) housed in a temperature-controlled facility with water and food provided ad libitum. Animals were sacrificed by carbon dioxide inhalation followed my midline thoracotomy and removal of the heart using procedures approved by the Colorado State University Care and Use Committee in accordance with the Guide for the Care and Use of Laboratory Animals published by the U.S. National Institutes of Health[107]. Hindlimb muscle tissues were immediately harvested for preparation of isolated mitochondria, permeabilized muscle fibers, or intact muscle tissue. Mitochondria were isolated from homogenized sections of gastrocnemius, plantaris and tibialis anterior muscles using differential centrifugation methods previously described in detail[108]. Soleus muscles from the same animals were carefully removed intact and placed in ice-cold BIOPS preservation solution containing (in mM) 0.1 µM free calcium, 20 imidazole, 20 taurine, 50 K-MES, 0.5 DTT, 6.56 MgCl2, 5.77 ATP, 15 phosphocreatine, pH 7.1. One soleus muscle (~10 mg) was teased with sharp forceps into fiber bundles and incubated with 50 mg/ml saponin in BIOPS on ice for 20 minutes with gentle rocking to permeabilize cell membranes and remove myoglobin while leaving mitochondrial membranes intact[108,109]. The contralateral soleus was left intact in ice-cold BIOPS until analysis.

To generate reduced and oxidized preparations, samples were transferred to mitochondrial respiration medium (MiR05;[108]) and incubated at 37° C for 5-10 minutes with (reduced) or without (oxidized) mitochondrial substrates (1 mM malate, 5 mM pyruvate, 20 mM succinate) in

the absence of adenosine diphosphate. This protocol provides saturating levels of reducing equivalents to the respiratory chain through Complexes I and II (reduced), or depletes any endogenous substrates present in the sample in the absence of exogenous substrates (oxidized).

6.2.4 Spectroscopic and imaging results

Mitochondrial Redox Spectroscopy:

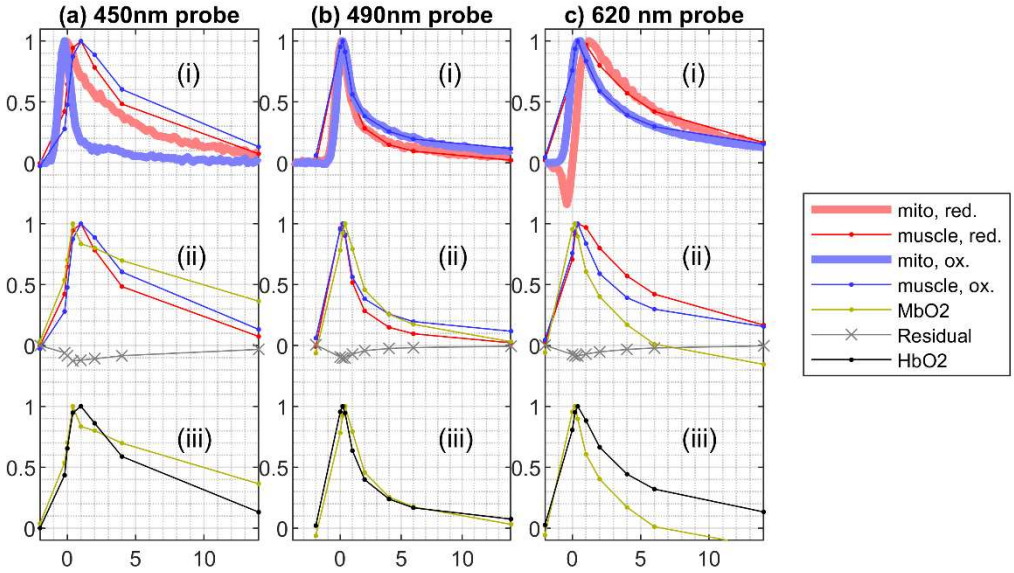

Figure 6.5. Transient absorption response curves. Solid lines indicate measurements on isolated mitochondria; thin lines extracted from muscle fiber imaging. See text for details.

TA spectroscopy of isolated mitochondria in suspension was performed with the LIA time constant set to 0.1sec, stepping τ from -2ps to 16ps in 0.2ps increments, while the imaging scan mirrors are running to prevent heating at the focus. The resultant delay scans are shown as thick solid lines in Figs. 6.5(a)(i), 2(b)(i), and 2(c)(i). For 490nm probe, oxidized versus reduced mitochondria have a longer lifetime, while both 620nm and 450nm probe reveal oxidized mitochondria to have shorter lifetimes. 450nm probe reveals the strongest redox contrast, while 490nm shows the smallest difference between redox states. These can be compared with the averaged signals from muscle fibers (red and blue thin dot lines), HbO2 response and the MCR-estimated MbO2 response (yellow and black thin dot lines), as discussed below.

Muscle Fiber Imaging:

TAM delay stacks of muscle fibers were then acquired with τ = {-2ps, 0ps, 0.2ps, 0.4ps, 1ps, 2ps, 4ps, 6ps and 14ps}. An example TAM delay stack of permeabilized muscle fibers with 522nm pump / 620nm probe is shown below in Fig. 6.6. The absence of signal at τ=-2 ps indicates the absence of any appreciable photothermal or long-lived (ms to μs timescale) signals. A sharp rise in ΔP_{pr} is seen at $\tau = 0\mathrm{ps}$, which decays almost entirely within 14ps. This image shows a striated pattern inside the fibers and bright spots distributed along the periphery of the fibers. These striations and bright spots are consistent with intra-fibrillar mitochondria (IFM) and paravascular mitochondria (PVM), respectively, typically observed in fluorescent staining of mitochondria in muscle fibers (see, e.g. Fig. 4 of Ref. [110]). Besides the striated structures, we can still observe a faint background inside each cell. This background may be from myoglobin, other hemeproteins, and out-of-focus mitochondria. Myoglobin is diffused throughout the cytoplasm and has $8-10\ \mathrm{mM}\times\mathrm{cm}^{-1}$ molar absorptivity at 522 nm[111], compared with $16\ \mathrm{mM}\times\mathrm{cm}^{-1}$for reduced cytochrome c [50]. Considering that both myoglobin and cytochrome c have about 0.5 mM concentrations in cytoplasm and mitochondria, respectively, and that cytochrome c is just one of four mitochondrial hemeproteins that can contribute signal, the mitochondrial contribution to the measured TA signal is expected to have a two- to eight-fold stronger signal than myoglobin. The bright spots of ~5μm diameter on the periphery of the muscle fibers are likely red blood cells, considering their diameter, and that each hemoglobin molecule contains four heme groups, and thus a $4\times$ stronger absorption cross-section than mitochondrial cytochromes or myoglobin.

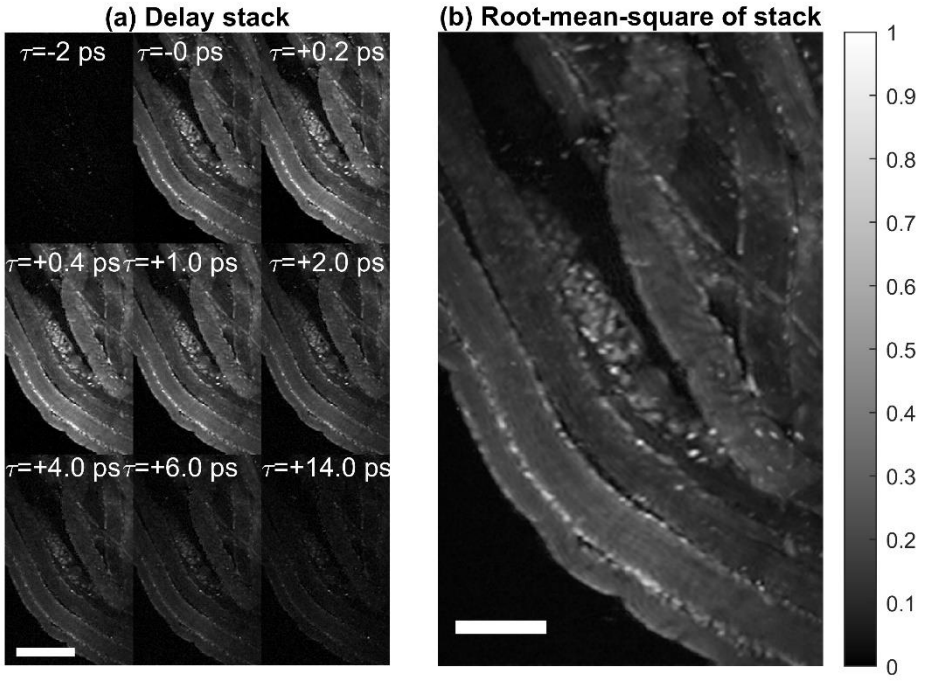

Figure 6.6. Transient absorption imaging stack, 620nm probe. 100μm scale bar. (a) Frames acquired at different probe delay times. (b) Root-mean-square taken across all probe delay times.

Transient absorption is a two-photon process, and like two-photon fluorescence microscopy, is capable of intrinsic optical sectioning. To demonstrate this with visible-wavelength TAM, we acquired a 3D volume of reduced intact muscle fibers at 490nm probe, setting the pump-probe delay to $\tau = 0$ps and stepped through the sample stage (ASI) along z axis for 100 μm with a step size of 2 μm. At each z slice, 20 frames of images are acquired and averaged, then the whole stack is filtered with a 3x3x3 median filter before interpolation to a volume with 1 μm^3 isotropic voxels. Representative z-slices and a volume rendering (maximum intensity projection, using MATLAB's built-in volshow function) are shown in Fig. 6.7. The thickness of the acquired volume suggests that visible-wavelength TAM has the potential for imaging not just cell cultures but tissues as well, though it should be noted our current configuration detects transmitted, rather than backscattered light.

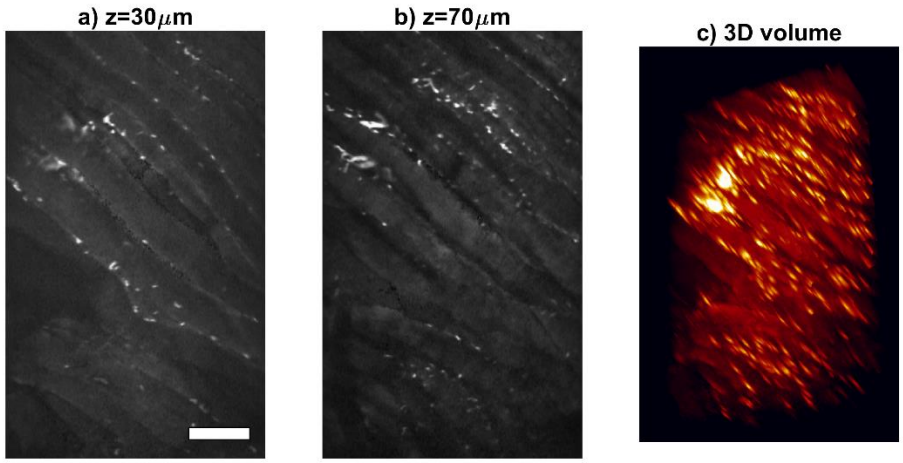

Figure 6.7. Z-stack of muscle fibers at τ=0ps probe delay. (a) Slice at z=30µm, (b) slice at z=70µm, and (c) maximum intensity projection rendering of entire stack. Scale bar 100µm..

6.2.5 Multivariate Cure Resolution (MCR) analysis of delay stacks

Transient absorption stacks were analyzed with multivariate curve resolution (MCR) [112,113] in order to retrieve the underlying signals corresponding to reduced and oxidized mitochondria and myoglobin and assign to each pixel an estimated redox ratio. In transient absorption imaging, this process of identifying the underlying components (i.e. spectral endmembers) is frequently done through principal component analysis (PCA) and phasor analysis[114]. Both PCA and phasor project the data onto an orthogonal basis. Because the transient absorption signals of the underlying components are often non-orthogonal (as can be seen from the reduced and oxidized responses of isolated mitochondria), additional steps are needed to identify the spectral endmembers[115]. Here we use MCR instead, which can recover non-orthogonal components with non-negative concentrations and has been successfully used to estimate underlying components and distributions in similar scenarios such as coherent Raman microscopy and transient absorption spectroscopy [116–118]. Here, MCR was set up as an alternating least-squares problem (MCR-ALS) with a non-negative concentration's constraint, two known components supplied by the averaged reduced and

oxidized responses from the interior regions of permeabilized muscle fibers, and a third unknown component to account for myoglobin.

In brief, MCR-ALS assumes the measured transient absorption responses $\boldsymbol{Y}$ to be a linear mixture of some underlying basis $\boldsymbol{X}$ plus some noise $\boldsymbol{N}$:

$$\boldsymbol{Y} = \boldsymbol{M}\boldsymbol{X} + \boldsymbol{N}.$$

Here, $\boldsymbol{Y}$ is an $(n_y\, n_x\, n_s) \times n_\tau$ matrix with each row containing the transient absorption response of an image pixel. $\boldsymbol{Y}$ is arranged to contain measurements from the mitochondrial portion (interior of the fibers), from all image stacks sharing a common probe wavelength. Each image stack is n_x pixels across, n_y pixels tall, n_τ probe delays deep, and there are n_s stacks. $\boldsymbol{X}$ is the underlying $n_c \times n_\tau$ basis, where $n_c = 3$ is the number of components assumed. $\boldsymbol{M}$ is the $(n_y\, n_x\, n_s) \times n_c$ mixing matrix, where each row contains the concentrations of the underlying components for a pixel. Specifically, the entries along the first column, $\boldsymbol{M_{i,1}}$ represents the magnitude of the reduced component, $\boldsymbol{M}_{i,2}$ represent the oxidized component, and $\boldsymbol{M_{i,3}}$ represents the magnitude of the myoglobin component. The first two basis of the initial estimate $\widehat{\boldsymbol{X}}$ is formed from the averaged signals of the interior of reduced and oxidized, permeabilized (lacking myoglobin) preparations of muscle fibers, respectively. The initial guess for myoglobin is provided by the average of the bright hemoglobin response of red blood cells at the periphery and between intact muscle fibers. Then an estimate of $\boldsymbol{M}$,that is, $\widehat{\boldsymbol{M}}$, is formed by use of the Tikhonov-regularized[119] pseudo-inverse of $\widehat{\boldsymbol{X}}$,

$$\widehat{\boldsymbol{M}} = \boldsymbol{Y}\, \widehat{\boldsymbol{X}}^{+}. \quad (2)$$

Next, the non-negativity constraint is applied by setting all negative elements of $\widehat{\boldsymbol{M}}$ to zero. Then the estimate of $\widehat{\boldsymbol{X}}$ is updated,

$$\widehat{\boldsymbol{X}} = \widehat{\boldsymbol{M}}^{+}\boldsymbol{Y}. \quad (3)$$

Then the first two rows of $\widehat{\boldsymbol{X}}$ are replaced with the known averaged TA signal of reduced and oxidized, permeabilized muscle fiber, the third row is allowed to change to account for the myoglobin response. This process of alternately estimating $\boldsymbol{X}$, $\boldsymbol{M}$, and enforcing the non-negativity and known components constraint is repeated until convergence. Then one final step estimating all three components of $\boldsymbol{X}$ is performed without replacement of the first two rows.

The results of MCR-recovered components $\widehat{\boldsymbol{X}}$ are shown in Figs. 6.5(a)(ii), (b)(ii), and (c)(ii) for 450nm, 490nm, and 620nm probe, respectively. Figs. 6.5(a)(iii), (b)(iii), and (c)(iii) show the comparison between MCR recovered myoglobin versus the hemoglobin response estimated by thresholding the brightest pixels. Fitting residuals, normalized to stack peak signal are shown in thin gray lines. In all three cases, the MCR-recovered basis shows typical positive excited state absorption (ESA) responses and myoglobin lifetimes are different from reduced and oxidized muscle. Both 490nm and 620nm probe wavelengths revealed good agreement between isolated mitochondria and MCR-recovered components. In addition, when comparing reduced versus oxidized mitochondrial component, it can clearly be seen that 620nm probe offers the largest differences in excited-state lifetime.

Next, the MCR-recovered concentrations of each pixel are used to generate false-color images of each TAM stack. The reduced, oxidized, and myoglobin components are mapped to yellow, cyan, and magenta, respectively by setting the {red, green, blue} value of each pixel to $\{M_{i,1} + 3M_{i,3}, M_{i,1} + M_{i,2}, M_{i,2} + 3M_{i,3}\}$. The resulting images for 450nm, 490nm, and 620nm probe wavelengths are shown in Figs. 6.8, 6.9, and 6.10, respectively. As expected from the response curves in Fig. 2, the separation between reduced and oxidized muscle fiber preparations was poor

for 450nm and 490nm, but clear at 620nm. The 620nm probe also reveals the clearest difference between intact and permeabilized muscle fibers, in terms of the third component (myoglobin), visible by the third component (purple) haze in the intact samples that is cleared away in the permeabilized samples (marked with a *).

Next, for each pixel, a redox ratio was calculated as the fraction of the reduced component over the sum of reduced and oxidized components,

$$R_i^{\text{redox}} = \frac{\boldsymbol{M}_{i,1}}{\boldsymbol{M}_{i,1}+\boldsymbol{M}_{i,2}+\epsilon}, \quad (4)$$

where $\epsilon = 0.01$ is used to avoid dividing by near-zero values in the case pixels with small signals. For each probe wavelength, the redox ratios were binned into histograms, as shown in Figs. 6.11(a-c). Again, the 620nm probe provides the clearest redox contrast, judging from the decreased overlap between reduced and oxidized histograms.

Finally, a similar process was used to estimate the myoglobin fraction of each pixel,

$$R_i^{\text{MbO}_2} = \frac{\boldsymbol{M}_{i,3}}{\boldsymbol{M}_{i,1}+\boldsymbol{M}_{i,2}+\boldsymbol{M}_{i,3}+\epsilon}. \quad (5)$$

Histograms of myoglobin fraction are shown in Figs. 8(d-f) comparing intact muscle fibers versus those that had cell membranes permeabilized with saponin. The 450nm probe does not show any difference, but both 490nm and 620nm results indicate that the MbO2 concentration decreases with permeabilization, as expected.

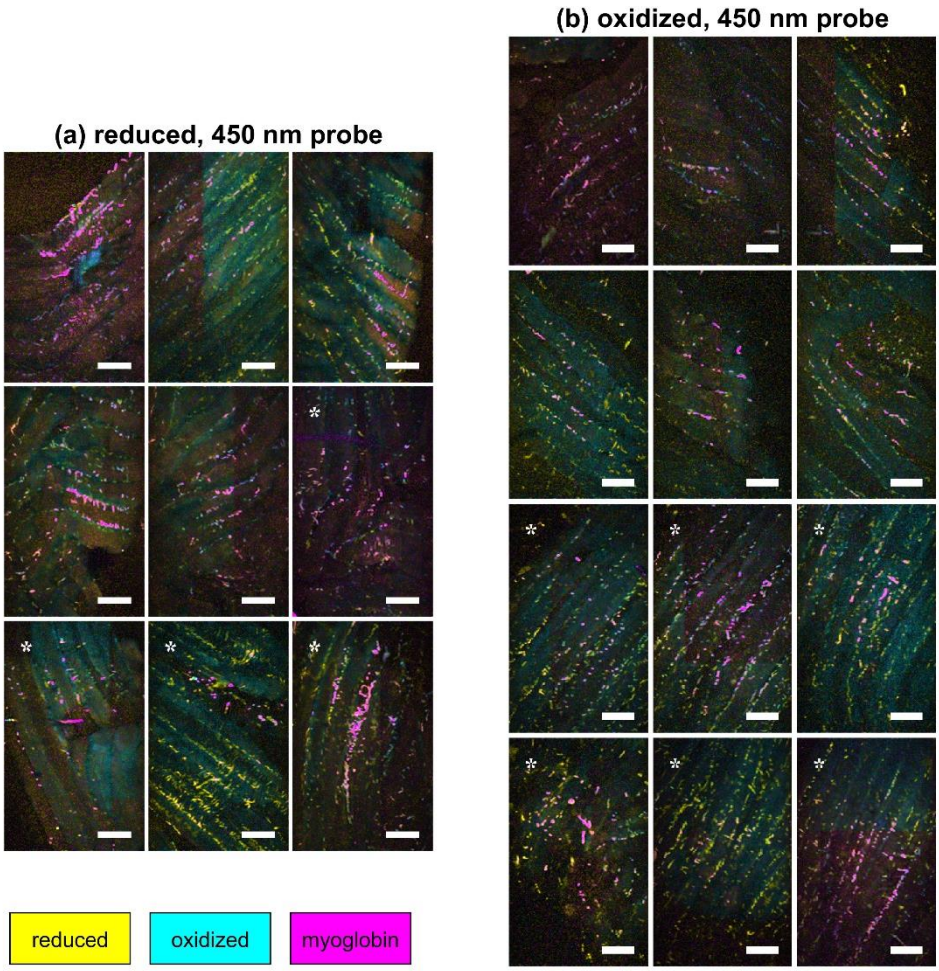

Figure 6.8. False-color images for 450nm probe based on MCR-recovered concentrations of reduced mitochondria (yellow), oxidized mitochondria (cyan), and myoglobin (magenta). (a) Reduced muscle fibers. (b) Oxidized muscle fibers. Asterisk (*) indicates permeabilized fibers. Scale bars 100µm

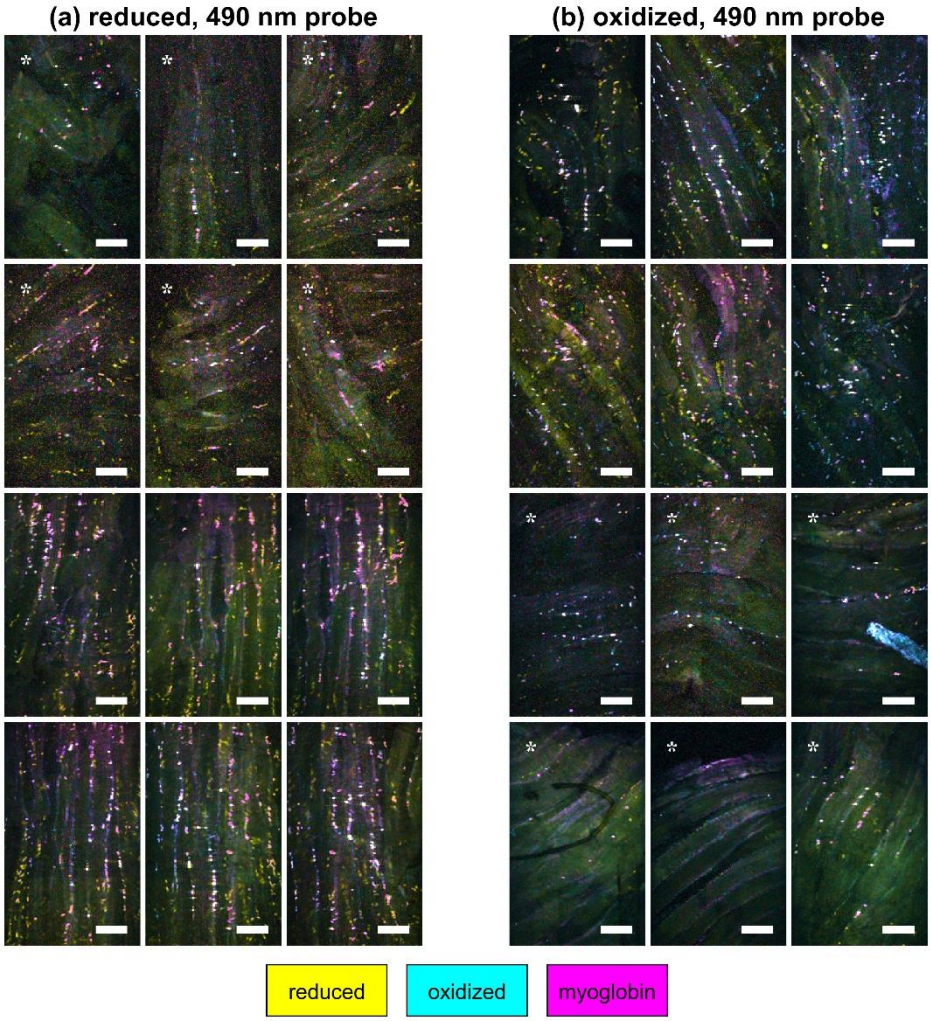

Figure 6.9. False-color images for 490nm probe based on MCR-recovered concentrations of reduced mitochondria (yellow), oxidized mitochondria (cyan), and myoglobin (magenta). (a) Reduced muscle fibers. (b) Oxidized muscle fibers. Asterisk (*) indicates permeabilized fibers. Scale bars 100µm

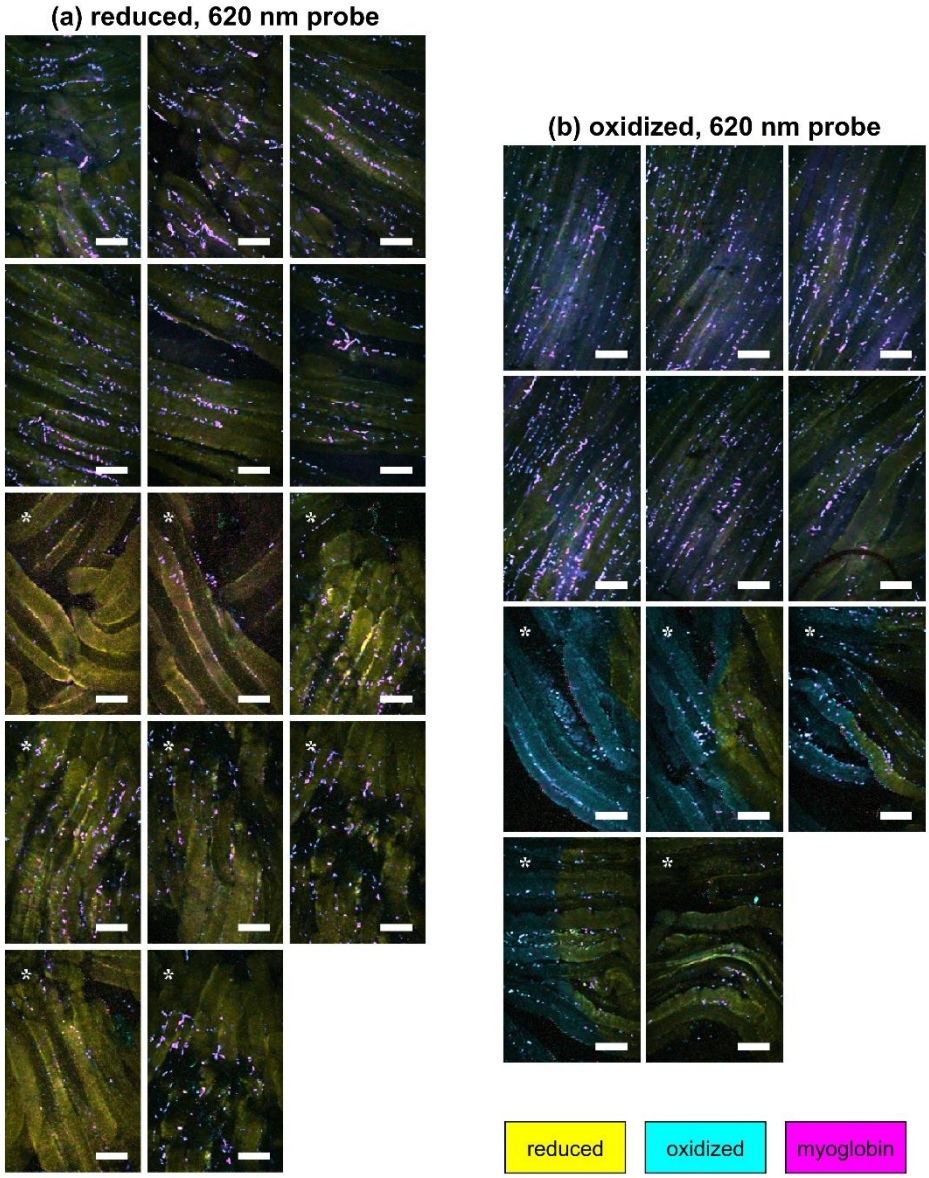

Figure 6.10. False-color images for 620nm probe based on MCR-recovered concentrations of reduced mitochondria (yellow), oxidized mitochondria (cyan), and myoglobin (magenta). (a) Reduced muscle fibers. (b) Oxidized muscle fibers. Asterisk (*) indicates permeabilized fibers. Scale bars 100µm.

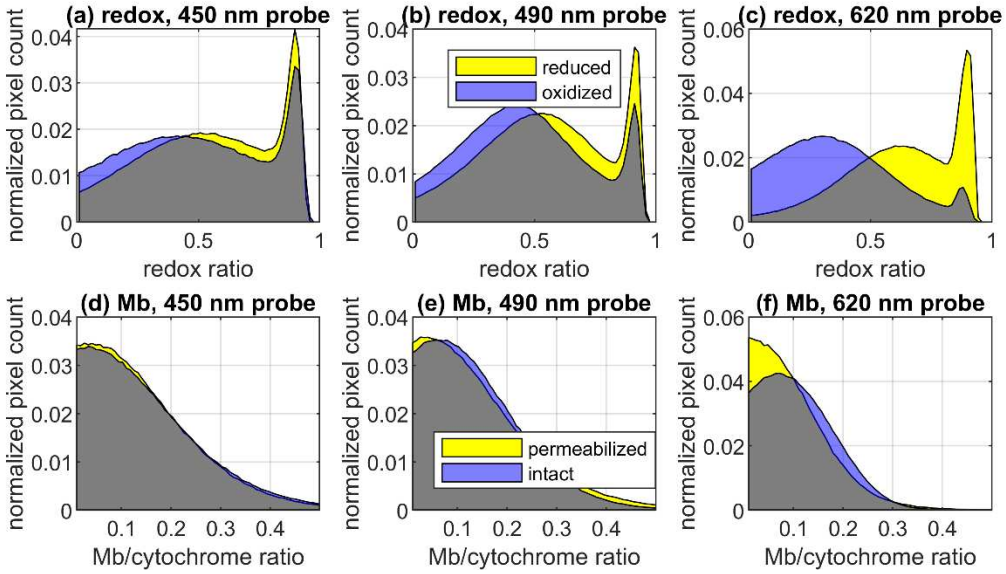

Figure 6.11. Redox ratio histograms for (a) 450nm probe, (b) 490nm probe, and (c) 620nm probe. Myoglobin ratio histograms for (d) 450nm probe, (e) 490nm probe, and (f) 620nm probe. Overlap indicated by gray

Chapter 7. Progress towards a tunable/hyperspectral pump.

7.1 TAM with both tunable IR pump and tunable visible probe.

This section will introduce the background and my achievement in developing a tunable IR pump laser based on self-phase modulation (SPM) of photonic crystal fiber (PCF) and Martinez pulse compressor. The technique of using SPM to broaden the laser spectrum and then using a Martinez pulse compressor to bring all the wavelength components in phase has been fully developed[120–123]. To first order, the broadening mechanism for the PCF (NL-1050-NEG-1) we are using is based on the combined effect of both group velocity dispersion (GVD) and SPM. SPM broadens the spectrum then GVD acts on the broadened spectrum to elongate the pulse width, making the temporal pulse shape rectangular. Then optical wave breaking appears on both leading and trailing edges[124,125]. The quadratic spectral phase arising from SPM can be easily compensated by the Martinez pulse compressor. Section 7.2 will introduce the quadratic spectral and temporal phase on a Gaussian pulse. The corresponding analytic equations will be derived. Section 7.3 briefly introduces the derivation of nonlinear Schrodinger equation (NLSE) that governs the nonlinear effects in optical fibers and different kinds of optical fiber used for supercontinuum generation. Section 7.4 compares my experimentally measured SC spectrum with theoretical predictions. In section 7.5, I use MATLAB to design and simulate a Martinez pulse compressor used for compressing the SC spectrum.

7.2 Spectral and temporal domain representations of Gaussian-shaped ultrafast laser pulse with linear chirp

This section is based on unpublished lecture notes from Dr. Randy Bartels' course in Ultrafast Optics at Colorado State University.

The time-domain expression for a transform-limited Gaussian laser pulse can be expressed as:

$$\mathcal{E}(t) = E_0 e^{-at^2} e^{j\omega_0 t} \quad (7.1)$$

Where E_0 is constant amplitude, e^{-at^2} portrays a temporal Gaussian envelope, and $e^{j\omega_0 t}$ describes a rapidly changing carrier electric field. The corresponding pulse intensity is:

$$I(t) = \frac{1}{2}\varepsilon_0 cn E_0^2 e^{-2at^2} \quad (7.2)$$

where the rapidly-varying $e^{j\omega_0 t}$ term has been averaged out by the slow response of the detector. The parameter a relates to the pulse duration τ_p through the following:

$$a = \frac{2\ln 2}{\tau_p} \quad (7.3)$$

Now consider a Gaussian pulse with a quadratic temporal phase:

$$\mathcal{E}(t) = E_0 e^{-at^2} e^{i(\omega_0 t + bt^2)} = E_0 e^{-(a-ib)t^2} e^{i\omega_0 t} \quad (7.4)$$

where bt^2 is the temporal phase. The above equation can be regarded as the product of a slowly varying amplitude and phase, and a rapidly changing optical carrier wave. Note that the slowly varying envelope approximation (SVEA) is valid only if $\sqrt{a} \ll \omega_0$ and $\sqrt{b} \ll \omega_0$, meaning both amplitude and phase envelope vary much slower than the carrier frequency. The intensity of a Gaussian pulse with a quadratic phase is:

$$I(t) \propto \mathcal{E}(t) \cdot \mathcal{E}(t)^* = I_0 e^{-4\ln 2 \times \left(\frac{\tau}{\tau_p}\right)^2} \quad (7.5)$$

Because the temporal phase, ibt^2, is a pure imaginary number, multiplying its conjugate brings the product to be 1. Therefore, the quadratic temporal phase does not affect the intensity profile.

To carry out the Fourier transform, we use the relative value $\Omega = \omega - \omega_0$, the frequency deviation relative to the center carrier frequency. For the transform-limited case, the complex spectral envelope of the Gaussian pulse without temporal phase can be written as:

$$\hat{E}(\Omega) = \int_{-\infty}^{\infty} E_0 e^{-at^2} e^{-i\Omega t} dt = e_0 \sqrt{\frac{\pi}{a_0}} e^{\left\{-\frac{\Omega^2}{4a}\right\}} \quad (7.6)$$

Its power spectrum as measured by a spectrometer is:

$$S(\omega) \propto \exp\left(-\frac{\Omega^2}{2a}\right) = \exp\left[-4\ln 2\left(\frac{\Omega}{\Delta\Omega_p}\right)^2\right] \quad (7.7)$$

From the above equation, we can derive the spectral FWHM $\Delta\Omega_p$ of a Gaussian pulse is directly related to its temporal pulse width:

$$\Delta\Omega_p = 2\sqrt{2\ln 2a} = \frac{2\ln 2}{\tau_p^2}$$

In order to study how quadratic temporal phase affects spectral FWHM, we use a Taylor expansion of the spectral phase to arrive at:

$$E(\Omega) = E_0 \sqrt{\frac{\pi}{a_0}} \exp\left[\frac{-\Omega^2}{4}\left(\frac{1}{a_0} + 2i\varphi_2\right)\right] \quad (7.8)$$

Before deriving the analytic expression for both spectral and temporal chirped Gaussian pulse, two concepts need to be addressed first: Taylor expansion for the spectral phase and instantaneous frequency. The spectral phase $\varphi(\Omega)$ is the relative phase of all the frequency components inside a laser pulse compared to the carrier frequency phase. The slowly varying envelope approximation (SVEA) implies the phase produced by 2nd order or higher-order dispersion is much slower than the carrier frequency phase. We can apply Taylor expansion to the spectral phase to simplify the math.

$$\varphi(\Omega) = \varphi_0 + \varphi_1 \times \Omega + \frac{1}{2}\varphi_2 \times \Omega^2 + \cdots = \sum_{n=0}^{\infty} \frac{\varphi_n}{n!} \times \Omega^n \quad (7.9)$$

where

$$\Omega = \omega - \omega_0, \qquad \varphi_n = \frac{d^n \varphi(\Omega)}{d\Omega^n}|_{\Omega=0} \quad (7.10)$$

The spectral phase defined here is equivalent to the phase term of the frequency domain counterpart in equation (7.4). But here, we include not only the quadratic term but also the constant term, 3rd order, and even higher-order terms.

The instantaneous frequency is the rate of phase change inside a laser pulse:

$$\omega_{inst} = \frac{d\phi(t)}{dt} \quad (7.11)$$

For example, if the temporal phase of a pulse takes the form $\phi(t) = \omega_0 t + bt^2 + \phi_0$, we will have an instantaneous frequency that changes linearly with respect to time: $\omega_{inst} = \omega_0 + 2bt$. This is analogous to the rising or falling pitch of a bird call, thus, it is also called a 'chirp'.

After having an instantaneous frequency and spectral phase Taylor expansions in mind, we can go ahead and derive the temporal expression of the Gaussian pulse that has a quadratic spectral phase, defined in Eqn. 7.8. Using the inverse Fourier transform to convert Eqn. 7.8 back to the time domain, we reach the following equation:

$$E(t) = 2\pi E_0 \sqrt{\frac{\Gamma'}{a_0}} e^{-\Gamma' t^2} \quad (7.12)$$

where

$$\Gamma' = a' - ib', a' = \frac{a_0}{1 + 4a_0^2\varphi_2^2} \ , b' = \frac{2a_0^2\varphi_2}{1 + 4a_0^2\varphi_2^2} \quad (7.13)$$

One final takeaway from this section is to notice that linear chirp is a quadratic temporal phase. And a Gaussian pulse with a quadratic temporal phase, after Fourier transforms, will give us a Gaussian pulse with a quadratic spectral phase. Material dispersion can cause 2nd order or even higher-order spectral phase to accumulate. But we can use a Martinez pulse compressor to compensate for the 2nd order dispersion, which will lead us closer to a transform-limited pulse.

7.3 Supercontinuum generation (SC) fiber

A mathematical model to inspect the nonlinear effect inside an SC fiber or any fiber requires solving the Helmholtz wave equation that relates the electric field to nonlinear and linear polarization. At the beginning of this section, I will follow Dr. Govind Agrawal's[126] procedure that derives the well-known nonlinear Schrödinger equation (NLSE) that governs the laser pulse evolution inside a fiber.

In Chapter 2 of his book "Nonlinear Fiber Optics"[126], he mentioned that the more convenient way to solve this problem is to start with the wave equation in the temporal Fourier domain:

$$\nabla^2\widetilde{\mathrm{E}}(\mathrm{r},\omega-\omega_0)+\epsilon(\omega)\mathrm{k}_0^2\widetilde{\mathrm{E}}(\mathrm{r},\omega-\omega_0)=0 \quad (7.14)$$

Where $\widetilde{\mathrm{E}}(\mathrm{r},\omega-\omega_0)$ is the Fourier transform of slowly varying envelope (SVE) $\mathrm{E}(\mathrm{r},\mathrm{t})$, defined as:

$$\widetilde{\mathrm{E}}(\mathrm{r},\omega-\omega_0)=\int_{-\infty}^{\infty}\mathrm{E}(\mathrm{r},\mathrm{t})\exp[\mathrm{i}(\omega-\omega_0)\mathrm{t}]\,\mathrm{dt} \quad (7.15)$$

And dielectric constant $\epsilon(\omega)$ here includes the nonlinear contributions $\epsilon_{\mathrm{NL}}(\omega)$:

$$\epsilon(\omega)=1+\tilde{\chi}^{(1)}(\omega)+\epsilon_{\mathrm{NL}}(\omega) \quad (7.16)$$

Equation 7.14 resembles free-space propagation, but with the nonlinear polarization source term accounted for by $\epsilon_{\mathrm{NL}}(\omega)$. As for the exact analytic formula to $\epsilon_{\mathrm{NL}}(\omega)$ varies with the different types of nonlinearities.

To solve the wave equation defined as Eqn. 7.14, the method of separation of variables needs to apply to the $\widetilde{\mathrm{E}}(\mathrm{r},\omega-\omega_0)$:

$$\widetilde{\mathrm{E}}(\mathrm{r},\omega-\omega_0)=\mathrm{F}(\mathrm{x},\mathrm{y})\widetilde{\mathrm{A}}(\mathrm{z},\omega-\omega_0)\exp(\mathrm{i}\beta_0\mathrm{z}) \quad (7.17)$$

Where $\mathrm{F}(\mathrm{x},\mathrm{y})$ is the modal distribution along the fiber cross-section. Since the fiber I will use is a single-mode fiber, we only need to set the $\mathrm{F}(\mathrm{x},\mathrm{y})$ to portray a fundamental mode[127] HE_{11}. $\widetilde{\mathrm{A}}(\mathrm{z},\omega-\omega_0)$ is a slowly varying function of z, and β_0 is the wavenumber. After applying the separation of variables to equation 7.14, we reach two wave equations for $\mathrm{F}(\mathrm{x},\mathrm{y})$ and $\widetilde{\mathrm{A}}(\mathrm{z},\omega-\omega_0)$ respectively:

$$\frac{\partial^2\mathrm{F}}{\partial\mathrm{x}^2}+\frac{\partial^2\mathrm{F}}{\partial\mathrm{y}^2}+\left[\epsilon(\omega)\mathrm{k}_0^2-\tilde{\beta}^2\right]\mathrm{F}=0 \quad (7.18)$$

$$2\mathrm{i}\beta_0\frac{\partial\widetilde{\mathrm{A}}}{\partial\mathrm{z}}+\left(\tilde{\beta}^2-\beta_0^2\right)\widetilde{\mathrm{A}}=0 \quad (7.19)$$

Solving the wavenumber $\tilde{\beta}$ requires applying first-order perturbation theory to Eqs. 7.18. briefly speaking, one only needs to consider the linear part of the dielectric constant and solve equation 7.18, assuming $F(x,y)$ to be HE_{11} mode. Then, the nonlinear dielectric constant is treated as a small perturbationEqn, 7.18 is solved again. These two steps will give an unperturbed wavenumber and a small wavenumber perturbation. $\tilde{\beta}$ is then the superposition of the two.

$$\tilde{\beta} = \beta(\omega) + \Delta\beta(\omega) \quad (7.20)$$

By substituting Eqn. 7.20 into Eqn. 7.19, we can reach the wave equation below:

$$\frac{\partial \tilde{A}}{\partial z} = i[\beta(\omega) + \Delta\beta(\omega) - \beta_0]\tilde{A} \quad (7.21)$$

where the approximation $\tilde{\beta}^2 - \beta_0^2 \approx 2\beta_0(\tilde{\beta} - \beta_0)$ has been used. Equation 7.21 is the NLSE in the spectral domain. It states that each spectral component that consists of a laser pulse accumulates a peculiar phase shift that is both frequency and intensity dependent[126].

For calculation convenience, $\beta(\omega)$ is expanded as a Taylor series:

$$\beta(\omega) = \beta_0 + (\omega - \omega_0)\left(\frac{d\beta}{d\omega}\right) + \frac{1}{2}(\omega - \omega_0)^2\left(\frac{d^2\beta}{d\omega^2}\right) + \cdots + \frac{1}{n!}(\omega - \omega_0)^m\left(\frac{d^m\beta}{d\omega^m}\right) \quad (7.22)$$

Meanwhile, we can treat $\Delta\beta(\omega)$ just as $\Delta\beta(\omega_0)$, when the pulse bandwidth is much smaller than carrier frequency ω_0. Now take the inverse Fourier transform of equation 7.21, we can reach the NLSE in the time domain:

$$\frac{\partial A}{\partial z} + \beta_1\frac{\partial A}{\partial t} + \frac{i\beta_2}{2}\frac{\partial^2 A}{\partial t^2} = i\Delta\beta_0 A \quad (7.23)$$

One simple trick is used here when doing the inverse Fourier transform, $(\omega - \omega_0)^n$ is equivalent to $i^n(\frac{\partial^2}{\partial t^2})$. In addition, $\beta_m = \left(\frac{d^m\beta}{d\omega^m}\right)$ is the linear dispersion and therefore the spectral phase is

$\phi_m\ \Omega^m$. That variable determines the accumulated spectral phase of m[th] order of dispersion. $\Delta\beta_0$ is the contribution of nonlinear optical effects to the pulse evolution in fiber. This term is also in charge of expanding pulse spectrum width.

I rewrite the NLSE below to include the optical fiber nonlinear effect in the general case. I ignore the 1[st] order spectral phase that corresponds to β_1. Because the linear spectral phase only leads to an identical time shift for all the spectral components. It does not affect the nonlinear optical effects.

$$\left\{\frac{\partial}{\partial z}+\frac{\alpha}{2}+i\frac{\beta_2}{2}\frac{\partial^2}{\partial T^2}-\frac{\beta_3}{6}\frac{\partial^3}{\partial T^3}\right\}A=i\gamma\left[|A^2|+\frac{1}{A\omega_0}\frac{\partial}{\partial T}(|A^2|A)-T_R\frac{\partial|A|^2}{\partial T}\right]A \quad (7.24)$$

Where T represents a time frame moving with the pulse at the group velocity v_g: T=t-z/v_g[126]. T_R, which is determined by the measured Raman-gain spectrum of the fiber in use, is the first moment of the Raman response function defined in equation 2.3.43 in ref[126]. Equation 7.24 has all the dispersion terms on the left-hand side, including loss, group velocity dispersion (GVD), and third-order dispersion (TOD). Here, A is the slowly varying envelope, which is a function of pulse propagation length inside the fiber and reduced time. The right-hand side considers three nonlinear terms: self-phase modulation (SPM), self-steepening, and Raman scattering. These nonlinear terms are responsible for generating new frequency components. Therefore, it is these nonlinear terms to broaden the pulse spectrum. If we only consider TOD, GVD and SPM and use the split-step method [128–131] to solve the NLSE, we can calculate the slowly varying envelope as a function of propagation distance inside the fiber. The simulation result shows that the input wave packet in the frequency domain is very narrow. The bandwidth increases with increasing propagation

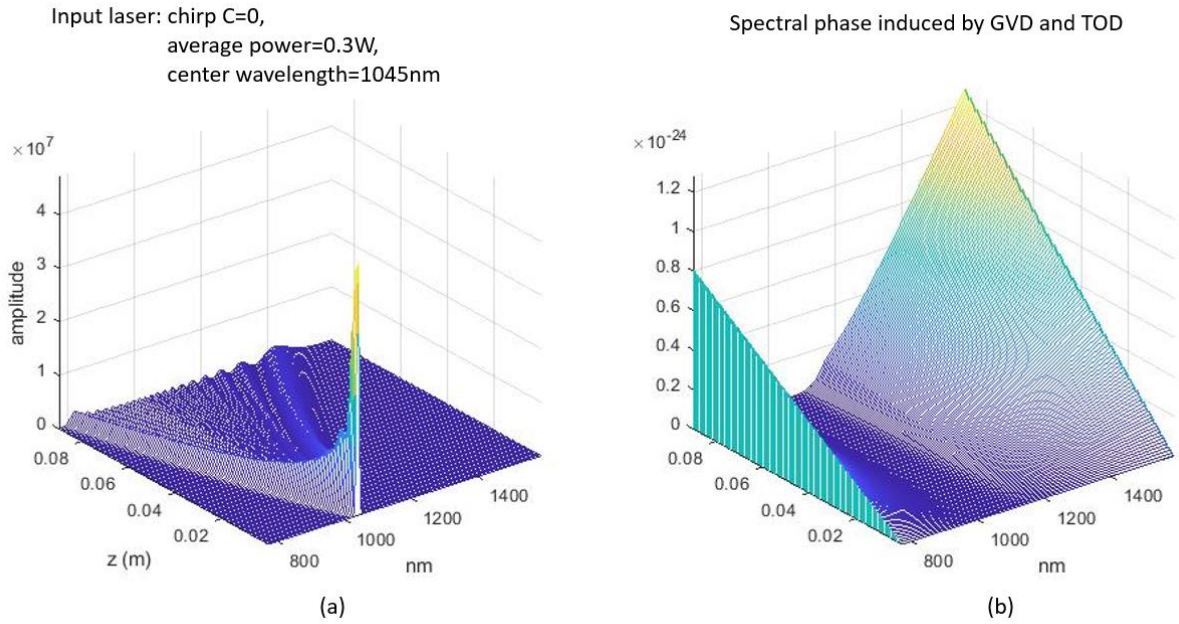

Figure 7.1: (a) SC generation initiated by a transform limited laser pulse with 0.3W average power and 1045nm center wavelength. The z is the propagation length inside the fiber. (b) spectral phase induced by GVD and TOD only. Note that the quadratic spectral phase induced by SPM is not shown in this figure.

distance inside the PCF. Figure 7.1 (b) shows the spectral phase arises from the TOD and GVD. The SPM induced spectral phase overwhelms those arising from the dispersion terms. When I plot the SPM spectral phase along with TOD and GVD spectral phase, I cannot tell if my linear dispersion term works properly. The reason why I only plot TOD and GVD spectral phase is just to make sure the phase calculation of each mechanism is correct. Here just to show the relatively small GVD and TOD spectral phase have the expected shape.

Since the input pulse has a center wavelength of 1045nm to initiate supercontinuum generation, the PCF needs to be designed to have a zero-dispersion wavelength (ZDW) around 1045nm. Various geometries have been invented for tapered fiber or photonic crystal fiber (PCF) to alter the ZDW of a fiber.

S.G. Leon-Saval and his colleagues found that decreasing the diameter of the taper waistcan move the ZDW to a shorter wavelength[132]. For each taper waist diameter, we can observe two ZDW in figure.7.2(a). When taper waist diameter decreases from 1100nm to 500nm, the larger/lower ZDW of each waist diameter continually decreases from >1100nm/450nm to 550nm/420nm. Therefore, one can always find a taper waist diameter of 1045nm ZDW to meet our requirements. The output spectrum from a 20 mm tapered fiber is shown in figure.7.3. The input pulse has a 1.5mW average power and a center wavelength of 532nm. The pulse duration is at the ns scale. After passing through the highly nonlinear fiber (HNLF) with a 510 nm waist diameter, the spectrum is broadened to cover the entire visible range. The spectrum structure shows that this fiber redistributes the pulse energy that was initially stored in the 532 nm frequency component to the whole visible range.

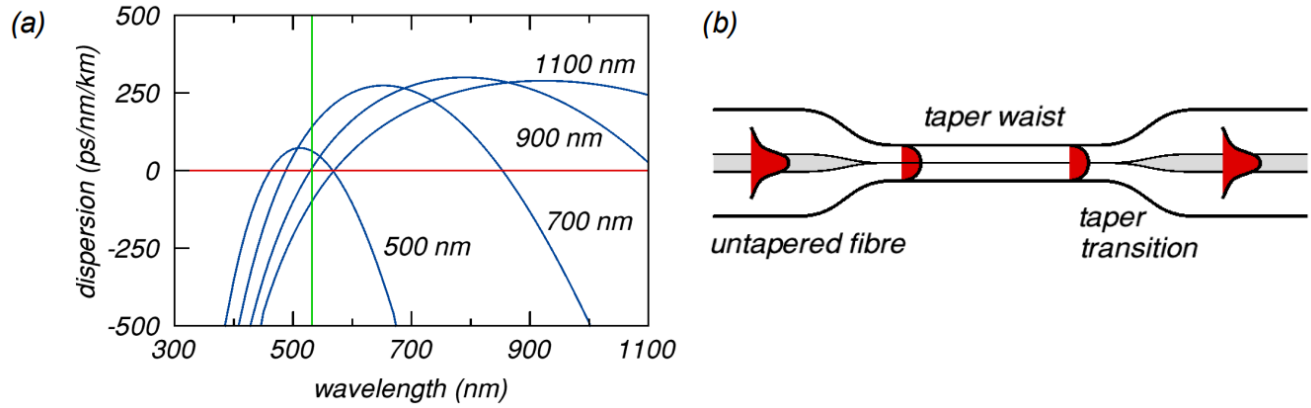

Figure 7.2: smaller taper fiber waist diameter leads to shorter zero dispersion wavelength. (a) dispersion profile changes with respect to decreasing taper waist diameter. (b) the sideview of the tapered fiber. *[121]*

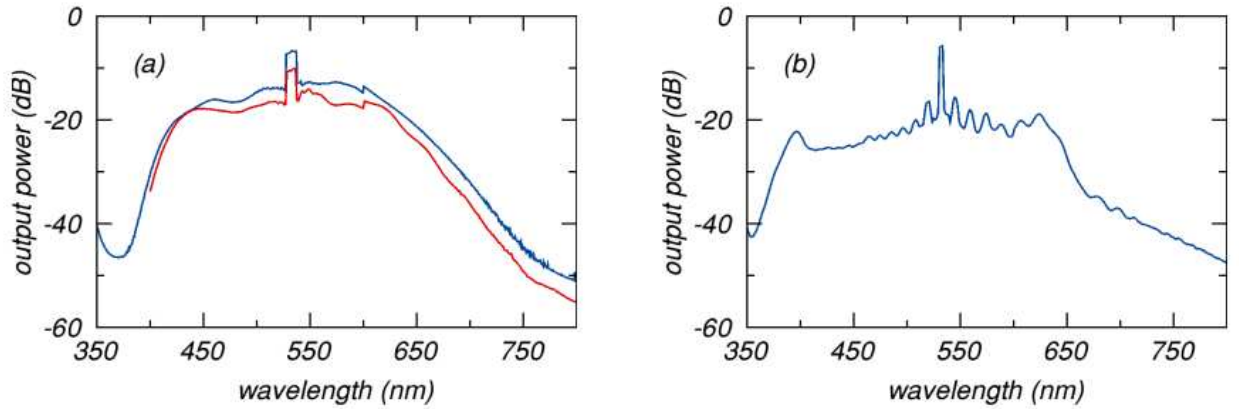

Figure 7.3: SC spectra generated by two sets of taper waist, tapered fiber length and average laser power (a) 920nm, 90nn and 3mW; (b) 510nm, 20mm and 1.5mW. The red curve is for a sample made from Nufern 630-HP. The blue curve is from Corning SMF-28. *[121]*

Instead of using tapered fiber made out of the commercialized single-mode fiber (SMF), Alexander and his collogues carefully designed the PCF's pitch size and relative hole size to meet the ZDW requirement[133]. They concluded that when using 1.55 μm pitch and 0.37 relative hole size,

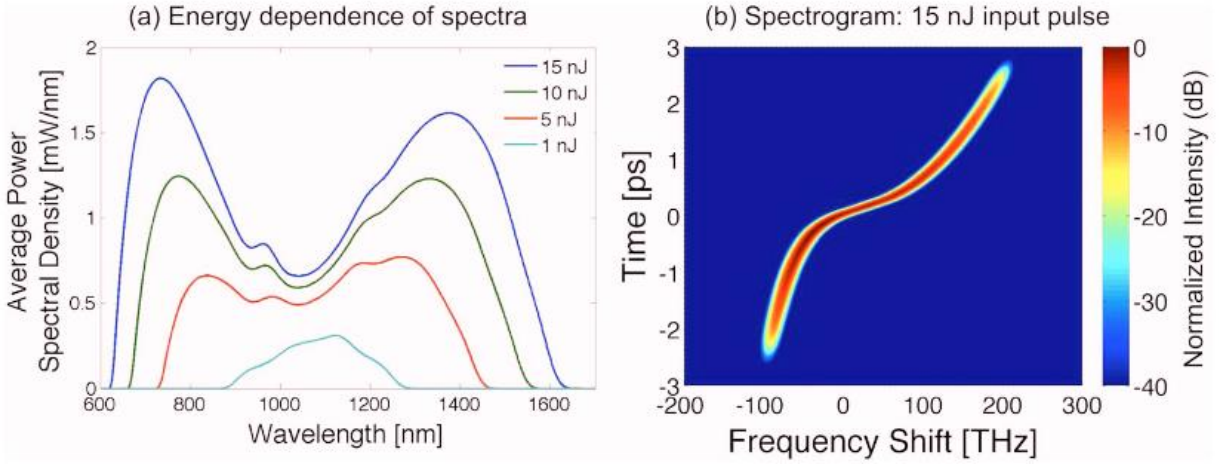

Figure 7.4: (a) SC spectra initiated from different input pulse energies. Fiber length is 10cm. pulse duration is 50 fs. (b) Spectrogram of the SC generated with the 15 nJ input pulse. Figure derived from ref [133]

the PCF will have 1080 nm ZDW and provide octave-spanning highly coherent supercontinuum generation, with mostly quadratic spectral phase. They also claimed that larger pulse energy leads to a broader output spectrum (Figure 7.4(a)). But the spectral density profile is less than ideal. The spectrogram (Figure 7.4(b)) of the output pulse from a 10cm PCF that is seeded by a pulse with

15nJ pulse energy and 50 fs pulse duration shows that the pulse duration becomes 2ps. The spectral profile has the signature structure that arises from SPM. A redshift and a blueshift can also be observed at the leading and trailing edges. Other than that, the chirp is predominantly linear in the central region. This spectrum has enough bandwidth to support 4 fs pulses if compressed.

Haohua Tu and his colleagues[134–138] use a commercially-available all-normal dispersion PCF NL-1050-NEG-1 to achieve an SC spectrum spanning from 900 nm to 1200 nm with high spectral power density. Firstly, this PCF has the ZDW located very close to our laser source fixed output of 1045nm. More importantly, SPM is the dominant nonlinear effect that broadens the spectrum. As mentioned, SPM will lead to quadratic spectral phase, which a Martinez pulse compressor can easily compensate for. This approach could lead to a compressible 300nm bandwidth supporting a transform-limited 5fs pulse, which could serve as a hyperspectral pump source for our TAM. Therefore, we decided to use NL-1050-NEG-1 purchased from NKT to create a hyperspectral pump source.

7.4 Experiment results comparing to split-step simulation results

In this experiment, two segments of 4cm single-mode fiber (Thorlabs SM980) were spliced to both ends of the PCF (NL-1050-NEG-1) by Tratech Fiberoptics Inc. Initial beam conditioning, alignment, and coupling were performed on a 1-meter segment of SM980. The beam diameter was adjusted to be ~1mm and beam position and angle were tuned until I had over 80% coupling efficiency. After replacing the alignment fiber with the SMF-PCF-SMF spliced fiber, the coupling efficiency dropped to 35%. This may be due to mode mismatch between the SMF and PCF. Other aspects are limiting the coupling efficiency, such as bending loss and fiber splice loss. Dr. Tu's experiments revealed the importance of keeping the fiber perfectly straight [139]. Otherwise, bending will prohibit longer and shorter wavelength components from passing through. This effect

has even been used by Jung Youngtae[140]to make an optical bandpass filter out of a PCF. The spliced PCF that we received is glued inside an aluminum groove. This fixed connection made sure the fiber does not break into pieces. But it is inevitable to introduce bending on the PCF segment and the very short 4cm SMF.

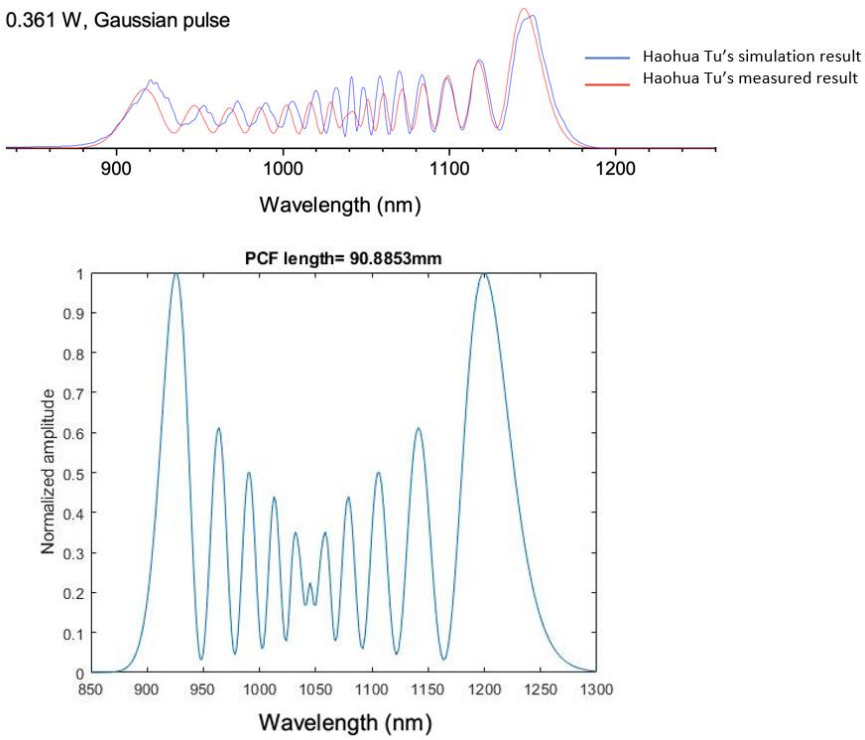

Figure 7.5: Haohua Tu's experimental and simulation results (upper panel)[134] compared to my simulation result (lower panel). Assume transform-limited pump pulse with 0.36W average energy and gaussian temporal pulse shape.

Figure.7.5 shows my split-step simulation comparison to Dr. Tu's published results. It shows that if the input pulse is nearly transform-limited, the resulting broadened spectrum is beautifully symmetric and wavy. SC spectrum with this shape are characteristically dominated by SPM and GVD effects, and the corresponding spectral phase is quadratic and easily compressible [120].

Unfortunately, my SC spectra (Fig.7.6 (c)) do not look like anything close to Dr. Tu's beautiful results. Instead, my measured spectra show a blue shifted peak that depends on incident power. There is likely a redshift peak around 1200nm to 1500nm, beyond our spectrometer detection range.

This is consistent with a chirped input pulse, which causes optical wave breaking at the pulse trailing and leading edges, and walk-off between different wavelength components. The leading and trailing edge wave-breaking phenomenon leads to the severe red and blue shift [121–123,141,142]. Meanwhile, the walk-off between wavelength components degrades the temporal overlap between different wavelengths, making it harder for SPM to take place.

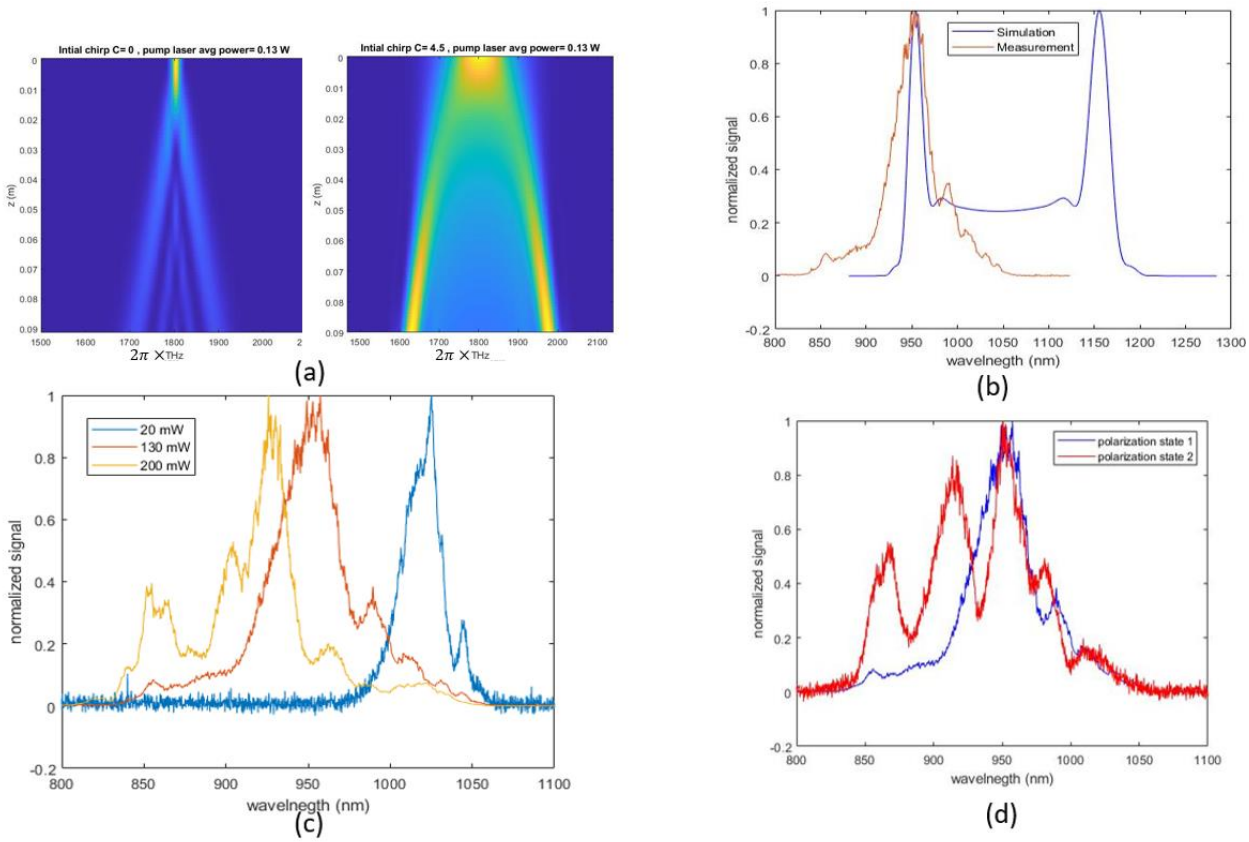

Figure 7.6: a) SC generation with transform-limited pump pulse and pre-chirped pulse. For the transform-limited case, a clear SPM takes place right at the fiber entrance, and the spectrum keeps on broadening symmetrically. In the pre-chirped case, wave breaking occurs right at the fiber entrance. SPM never initiates. Spectral broadening due to wave breaking produces red and blue shift edges. b) comparison between simulation and measurement when laser power is set to 130 mW. c) SC measurements when varying the PCF output laser power from 20mW to 200mw. d) PCF output laser power is set to 130mW, rotate the input laser polarization states. I choose two polarization states. The spectral shape is very sensitive to the input laser polarization state.

In order to confirm this interpretation assumptions, I use the split-step method to simulate the SC spectrum initiated by a pre-chirped Gaussian pulse with a positive chirp. Fig. 7.6 (a) compares the

case with transform-limited pump pulse and that with pre-chirped pump pulse. The Chirp parameter "C" follows the definition in Section 3.2.2 of Nonlinear Fiber Optics written by Govind P. Agrawal[126]. When C is positive, the instantaneous frequency increases from the leading pulse edge to the trailing edge, namely positive chirp or up-chirp, vice-versa.

The transform-limited case (Fig. 7.6(a), left panel) shows an evenly and symmetrically broadened spectrum arising from SPM. The pre-chirped case (Fig. 7.6(a), right panel) shows instead the emergence of a red-shifted and blue-shifted peak. The comparison between my experimental measured SC spectrum and my split-step simulation is shown in Fig.7.6 (b). The laser power is set to 130mW since this is measured output laser power from PCF in the experiment. When setting the initial chirp parameter to 4.5, we can see the measured and simulated SC spectra both have peaks at 930nm, and the side lobes around 920nm also roughly coincide. Again, the measurement result only shows wavelength components below 1100nm, limited by the spectrometer detection range. If we had a spectrometer that could detect around 1200nm to 1500nm, we would expect to see a red shift peak and side lobes that roughly match the simulation results.

The following elaborates on how to calculate the chirp parameter and pulse width at the PCF input facet.

If the laser source produces a laser pulse that has the following form:

$$E(t) = E_0 \exp\left[-\left(\frac{t}{\sqrt{2}\tau_0}\right)^2\right] \exp(iC_{int}t^2) \exp(i\omega_0 t) \quad (7.25)$$

Where the three exponential terms represent a Gaussian envelope, chirp term and a rapidly changing carrier term. The pulse width τ_0 is the half-width at 1/e-intensity point of the Gaussian envelope only. I chose τ_0 to be 100 fs in my simulation. When the initial chirp parameter $C_{int} =$

4.5, my simulation and experimental result have the best agreement. Dr. Agrawal's approach only requires the knowledge of GVD and the length of the dispersive components for calculating the extra chirp arising from those dispersive components. Following this approach, the chirp parameter at the PCF input facet has the simple form:

$$C_{fiberEntr} = C_{int} + (1 + C_{int}^2)(\beta_2 z/ \tau_0^2) \quad (7.26)$$

And the pulse width at the PCF input facet takes the form below:

$$\frac{\tau_{fiberEntr}}{\tau_0} = \sqrt{\left(1 + \frac{C_{int}\beta_2 z}{\tau_0^2}\right)^2 + \left(\frac{\beta_2 z}{\tau_0^2}\right)^2} \quad (7.27)$$

Therefore, we come to the final formula for pulse right at the PCF input facet:

$$E(t) = E_0 \exp\left[-\left(\frac{t}{\tau_{fiberEntr}}\right)^2\right] \exp\left(iC_{fiberEntr}t^2\right) \exp(i\omega_0 t) \quad (7.28)$$

In the current experimental setup, there are two kinds of dispersive components between the laser source and the PCF: BK7 (lens) and fused silica (SMF SM980). Their GVD are 23.909 fs^2/mm and 17.874 fs^2/mm respectively. The SM980 is 4cm long. And the lens material is also roughly 4cm thick. All those preconditions lead to the pulse right at the PCF entrance to have a pulse width of 187 fs and chirp parameter of 8.56.

One shortcoming of the current split-step implementation is that it does not account for the input laser polarization state. Yet when dealing with PCF, the SC spectrum is very sensitive to the input pulse polarization state. Figure 7.6(d) shows the rotating input laser polarization. Even with the same 200mW laser output power, the SC spectrum profile can change significantly. The

disagreement on the spectral profile between simulation and measurement is very likely related to the input laser polarization state.

7.5 Pulse shaping using Martinez pulse compressor

Even though the prechirped input pulse prohibits the PCF from having a pure SPM spectrum, once this problem is solved, we anticipate a SC spectrum that only has a quadratic spectral phase, which can be compensated with a folded Martinez compressor. The next step is to compress the broadened light with a Martinez pulse compressor. In this section, I use a modified ABCD raytracing matrix to simulate the optical path lengths (OPLs) for all the wavelength components.

Materials always exhibit large positive material dispersion in their corresponding transparency regions. The ultrafast community always refers to the positive material dispersion as normal dispersion. For example, fused silica's (a common fiber material) refractive index is 1.46 for 600 nm incident light[143]. And its material dispersion, $d^2n/d\lambda^2$, evaluated around 600nm is 1.3×10^{-7} nm^{-2}. That material dispersion leads to quadratic phase accumulation with respect to incident wavelengths. Thus, after propagating for a certain distance within fused silica, the accumulated phase difference between each wavelength component becomes the obstacle to achieving transform-limited (TL) pulses in the time domain.

Several methods have been developed to generate *negative* (i.e. anomalous) dispersion to compensate for material dispersion and produce compressed pulses. Several prominent figures among many are Treacy, who utilized diffraction grating pair for pulse compression[144], and Martinez and Fork, who invented prism pair pulse compression[145]. Here, I will use a Martinez pulse compressor to bring the SC wavelength components in phase again[146].

Fig. 7.7 shows the schematic of an unfolded Martinez pulse compressor. It is composed of two identical gratings and two identical lenses. To make a folded Martinez pulse compressor, one can

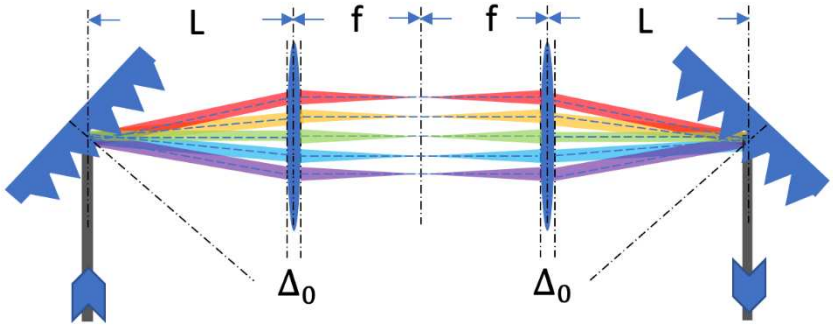

Figure 7.7: Martinez pulse compressor layout. It is consisted of two identical positive lenses and two identical gratings. Because of the wavelength dependent angular dispersion of grating, the chief ray of each wavelength counterpart follows different optical path. Where L is the grating to lens distance, f is the focal length of the positive lens. Δ_0 is the center thickness of a lens.

also put a mirror on the center Fourier plane. In that way, only one grating and one lens are needed. The beam will double pass the grating lens pair to fulfill the same pulse compression that an unfolded Martinez pulse compressor can offer. The unfolded pulse compressor schematic is shown for illustration.

The incident pulse has some initial large positive material dispersion. Because of the dispersion, the wavelength components consisting of the pulse are no longer in phase. Therefore, the incident pulse is not transform-limited. The 1st grating produces angular dispersion between wavelength components. It decomposes the input pulse into a series of plane waves with different center wavelengths, propagating along with different angles. That is the critical step to introducing wavelength-dependent group delay actively. Then all the plane wave components are focused by the first lens and form a series of focal points onto the center Fourier plane. A translatable slit at the Fourier plane can select the pump center wavelength. Then the second lens brings all the components back to plane waves. Last, the second grating is to collimate and combine all the spectral components. It resets the angular dispersion to zero and makes all the spectral components

propagate counter parallel to the input beam. One thing that needs to notice is that spatial chirp does exist when two gratings are not at the front and back focal planes of the center 4-f system.

The distance between the two lenses is fixed to twice as long as the focal length. But one can still adjust the distance between the grating and the lens to introduce either negative or positive dispersion. The pulse compressor needs to be set to a configuration to introduce negative dispersion to compensate for the initial material dispersion.

Even though the relationship between the grating lens distance and the pulse compressor dispersion has been carefully studied, this report will introduce another phase shift calculation method that utilizes ray tracing to compute the optical path length (OPL) of each spectral component one optical element by another. The ray-tracing Matrices are sufficient to calculate OPL differences between all the spectral components. We can decompose the ray-tracing-based OPL simulation into two steps. First, it executes the ray-tracing procedure assuming that two lenses are infinitely thin. The resultant ray positions corresponding to each spectral component at the exit facet of each optical element can be used to calculate OPLs in air. Second, the OPL in lenses is calculated by an easy equation and added to the OPL in the air to form the total OPL of each spectral component.

Light propagation length in air

The 3×3 matrix can describe light propagation inside each optical element in Eqn. 7.29. Equation 7.29 indicates that the incident ray right before element i has position x_i and propagates at an angle of x_i'. To achieve the exit ray position and propagating angle, one only needs to multiply the 3×3 matrix associated with the optical element, marked as x_{i+1} and x'_{i+1}, respectively.

$$\begin{vmatrix} x_{i+1} \\ x'_{i+1} \\ 1 \end{vmatrix} = \begin{vmatrix} A & B & E \\ C & D & F \\ 0 & 0 & 1 \end{vmatrix} \begin{vmatrix} x_i \\ x'_i \\ 1 \end{vmatrix} \qquad (7.29)$$

A, B, C, and D elements consist of the usual ray transfer matrix[147]. The 2×2 ray transfer matrix can calculate an exit ray's position and propagating angle from an optical element. However, it does not contain any information about the angular dispersion of the element due to refraction or diffraction differences between wavelengths. Siegman[148] introduced two other matrix elements, E and F, to address that issue ([148] Chapter 15). The E element adds a wavelength-dependent correction to the exit ray position. The F element expresses the angular dispersion. F is crucial for accurate ray tracing of each spectral component and phase shift calculation in the Martinez pulse compressor.

For Martinez pulse compressor ray tracing, we only need to know the grating matrix, the lens matrix, and the free space matrix. These three matrices and their corresponding optical elements are shown in Fig. 7.8. The Martinez pulse compressor contains five optical elements. To achieve the pulse compressor output ray's position and propagating angle, one just needs to multiply the five matrixes associated with their corresponding elements in reverse order [146]. On the other hand, by multiplying these matrixes, we can trace the ray one element after another. Then we can track the OPL of each spectral component accurately. One thing that needs to be noticed is that the lens matrix utilizes the thin lens assumption. Instead of regarding the lens as two curved surfaces and a glass slab in between, the lens matrix implies that the lens is regarded as an integral whole with infinitely small thickness, ignoring light propagation distance inside the lens.

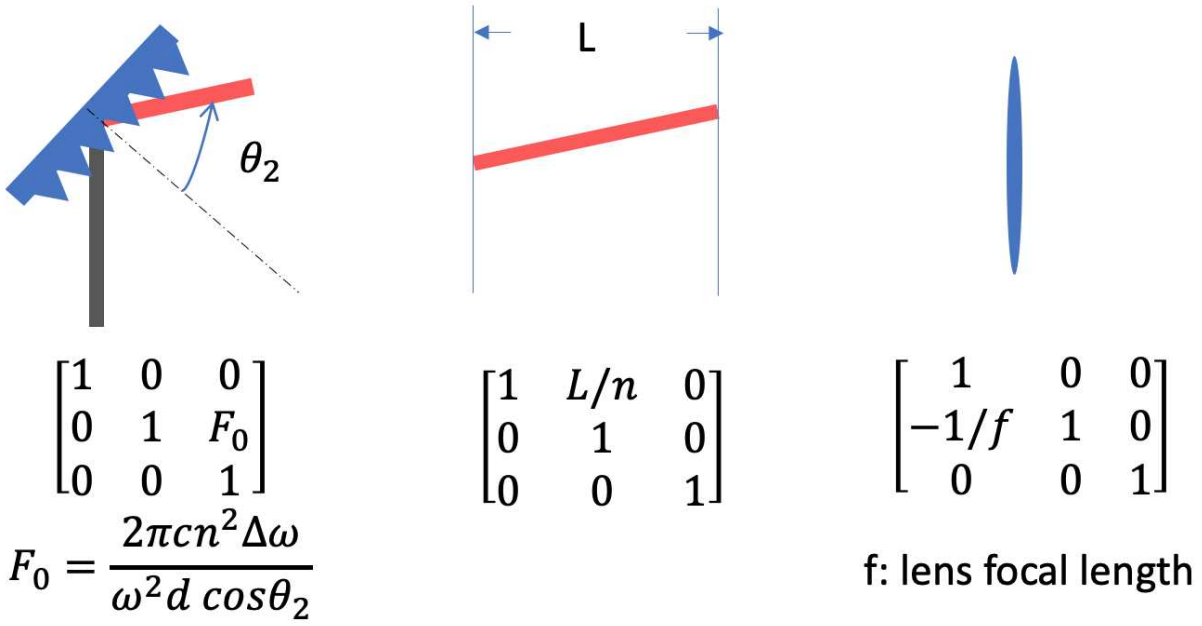

Figure 7.8: optical components that consist of the pulse compressor and their corresponding ray tracing matrixes. They are grating (a), free space (b) and lens (c).

The Matlab simulation explores GDD imparted by the compressor by launching an incident unchirped pulse and examining the spectral phase afterwards. The grating diffraction angle of the carrier frequency, ω_0, is set to 0 degrees. Right after the 1st grating, the initial pulse is decomposed to a series of plane waves with different center frequencies, distributed along wavelength-dependent angles. The deviations between those frequency components with respect to the central carrier component are Δω. Then with the transfer matrix shown in Fig.7.8, we can calculate the ray position and propagating angle of each spectral component one element after another. This ray tracing is simpler than the convention ray tracing. Instead of tracing the chief ray and marginal ray, the simulation only focuses on tracing central lines of the spectral components, marked as dash lines in Fig. 7.7.

The ray-tracing procedure is followed. It starts with an unchirped Gaussian pulse that is then represented in the angular frequency domain with carrier frequency ω_0. After the grating transfer matrix multiplication, the ray positions and propagating angles of the output rays right are marked as $x_{out1}(\omega)$ and $x'_{out1}(\omega)$. Those positions and propagating angles are frequency-dependent because the grating's first-order grating diffraction angle increases with decreasing optical frequency. The second optical element is the free space between the first grating lens. Its matrix does not contain the angular dispersion term. Therefore, each spectral component propagates with its own initial angle $x'_{out1}(\omega)$ to the front facet of the lens. At that facet, the ray positions and angles are marked as $x_{out2}(\omega)$ and $x'_{out2}(\omega)$. Then multiplication with the lens matrix calculates output ray positions, $x_{out3}(\omega)$, and angles, $x'_{out3}(\omega)$. This approach is repeated for the rest of the elements, producing the output rays' positions and angles of every element.

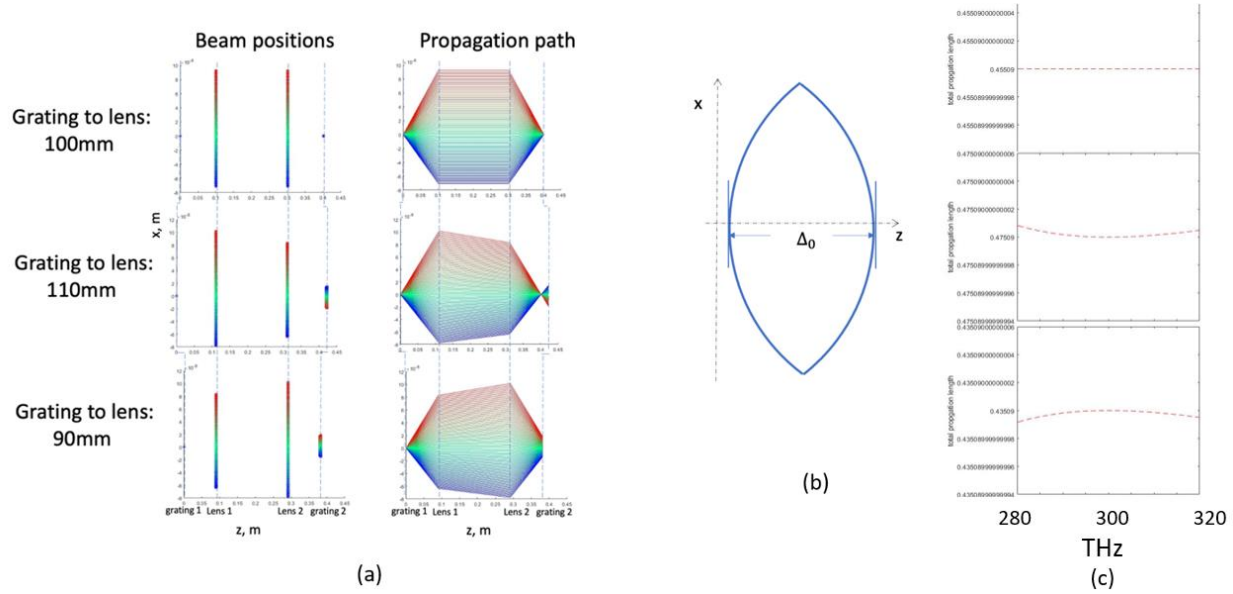

Figure 7.9. Ray tracing analysis of the pulse compressor (a) Optical paths of the grating without considering the lens thickness. (b) lens thickness as a function of vertical axis x, as well as on axis thickness and optical axis z. (c) optical path differences between frequency components for three grating to lens distance. When gratin to lens distance equals to lens focal length 100mm, it does not introduce any spectral phase. When grating to lens distance is larger or smaller than the focal length, pulse compressor introduces positive or negative quadratic spectral phase.

The ray-tracing simulation results are shown in Fig. 7.9 (a), for grating-to-lens distance of 100 mm, 110 mm, and 90 mm. The lens focal length is fixed at 100 mm. When the grating to lens distance equals the lens focal length, as shown in upper row of figure 7.9 (a), all the spectral components coincide at the input facet of the first grating, then start to disperse at the exit facet of the first grating, then are focused by the first lens and collimated by the second lens. In the end, all the spectral components coincide again at the second grating. The spectral components' propagations follow a similar path when the grating to lens distance is larger than the lens focal length, as shown in the middle row of Fig. 7.9 (a). The only difference is that they no longer coincide at the second grating. Along the x-axis, one can observe that the beam positions of shorter wavelength to longer wavelength components distribute from top to bottom. When the grating to lens distance is shorter than the lens focal length, as shown in the lower row of Fig. 7.9 (a), a clear beam position displacement can be observed at the second grating position as well, with reversed order. Along the x-axis, one can observe that the beam positions of shorter wavelength to longer wavelength components are distributed from bottom to top.

The OPL variation with respect to the spectral component in air alone does not reflect the whole picture of the pulse compressor induced spectral phase. For example, consider the the upper row of Fig. 7.9 (a). When lens focal length equals the lens-to-grating distance, the pulse compressor should not introduce any spectral phase. However, directly converting the OPL variation in air to the spectral phase, we can see that the phase shift introduced by the OPL difference in air alone is already a quadratic function of optical frequency. The carrier frequency component ω_0 has the shortest OPL in air. For those frequency components larger than ω_0, the OPL increases with the increasing frequency ω. For the frequency components smaller than ω_0, the OPL increases with

the decreasing frequency ω. But this is not the total phase shift that the pulse compressor brings in. We also need to consider the propagation length in the lens material.

Light propagation length in the two lenses

A positive lens has a maximum thickness at the center. The thickness gradually decreases as the position of interest moves away from the center part. In other words, the thickness varies with the transverse position x. That thickness variation introduces propagation length differences between spectral components. The illustration figure of a lens morphology is shown in figure 7.9 (b)

The OPL introduced by the lens can be written as:

$$OPL_{lens}(x) = n\Delta_0 - \frac{\|x\|^2}{2f} \quad (7.27)$$

As we can see, it is a function of transverse position x, where n is the lens refractive index, Δ_0 is the lens center thickness, f is the lens focal length. Applying this equation to two lenses successively, with the acknowledgment of each frequency component incident position $x(\omega)$, we can easily calculate the OPL in the lens for each frequency component.

Total light propagation length

The Martinez pulse compressor is firstly arranged in a 4f configuration. That is a well-known zero-dispersion setup [149]. Based on the previous two sections, OPL in the air is a positive quadratic function of ω, whereas OPL in the two lenses is a negative quadratic function. The resultant total OPL in the air and the two lenses is constant across the entire pulse spectrum, equivalent to the zero-phase shift with respect to ω which is shown in upper panel in Fig. 7.9. Setting the lens-to-grating distance to be larger or smaller than the lens focal length leads to either positive or negative

quadratic total OPL function, shown in the middle and lower panels of Fig. 7.9 (c), indicating that such pulse compressor can compensate for both positive and negative initial pulse chirp.

Chapter 8. Fiber-optic confocal reflectance probe head for future TAM miniaturization

A recent publication in Nature inspired us to miniaturize our current bench top TAM. In that paper, Alberto Lombardini et al., [150] present a compact flexible fiber optic scanning endoscope that has similar excitation delivery and signal collection mechanisms as confocal microscopy. It can generate CARS, SHG and TPEF endoscopic images with submicron spatial resolution. Instead of using a conventional single mode fiber (SMF), one of their key innovations is to use a hollow-core fiber with a Kagome lattice to guide the pump and stokes beam simultaneously. That fiber has negligible four wave mixing background, GVD and pulse distortion which are the major technical problems that hindered the CARS endoscopy development[151]. TAM miniaturization faces the same technical challenges. After reading their paper, I realized that it is very likely that we can build an endoscope that can offer TA chemical specificity. Realization of that goal will offer us a powerful noninvasive diagnostic tool for mitochondrial diseases.

To realize that long-term goal, my first periodic goal is to build a benchtop confocal reflectance microscopic probe head based on a resonantly scanned fiber cantilever that is driven by a piezo tube (PZT). In this section, I will briefly introduce the background of confocal reflectance microscopy and my current achievements on our own handheld confocal reflectance microscopic probe.

8.1 Introduction

The first confocal scanning microscope was invented in 1955 by Marvin Minsky[152]. That confocal scanning microscope was built to generate 3D visualization of neurons in unstained brain tissue. Back in the time, due to the scattered light from highly interwoven cells, the conventional microscope could not spatially differentiate the individual cell structure. During his years of being a Junior Fellow at Harvard, Marvin, by installing one pinhole right after a zirconium light source and another pinhole right in front of a sensitive device, realized point illumination and point detection that can reject out of focus stray light. With the aid of out-of-focus rejection ability, such a microscope can produce a 3D image stack of biological tissue. However, because of the limited scanning methods at the time, this confocal microscope used stage scanning to build an image, which is slow and not ideal for in vivo imaging.

Beam scanning is an alternative method to build a confocal image. Laser scanning confocal microscopy (LSCM), which is one of the most commonly used confocal imaging modalities, utilizes such a scanning mechanism. A pair of galvanometer scanning mirrors are normally employed to raster scan a collimated laser beam. Then a lens assembly set focuses the scanning laser beam to form a diffraction-limited scanning point on the specimen. The reflected light or transmitted light from each point in the specimen can be collected in the epi mode or forward mode. A photomultiplier tube (PMT) behind a pinhole detects the signal light point by point.

This more effective scanning method was initially invented by Wilke[153] and then utilized by John White and Brad Amos for epifluorescence confocal microscopy in the 1980s[154]. In conventional epifluorescence microscopy, the stray light background resulted from both the neighboring particles on the focal plane that are evenly illuminated, and the structures that are below or above the focal plane deteriorate the image contrast. Yet, in the LSCM, thanks to the out-

of-focus fluorescence rejection, the higher optical resolution, and faster-scanning speed, John White and Brad Amos were able to generate a 3D image stack of a developing embryo of c elegans, revealing fine details such as mitotic spindle structures.

Newly developed scanning components based on MEMS [155–157] allow miniature laser scanning confocal microscopy (LSCM) designs. Eric Seibel's group has very detailed theoretical and technical illustrations on fully developed laser scanning microscope based on a piezo transducer (PZT) -driven fiber cantilever[158,159]. I decided to follow their procedure to build our initial confocal probe head.

The most critical component of a fiber-optic confocal microscope is the scanning fiber. When the frequency of the AC voltage applied to the PZT equals the resonant frequency of the fiber cantilever, the fiber scanner will produce the largest scanning range. The x-axis and y-axis scanning frequency, fx and fy, should be chosen adjacent to that resonant frequency. The difference frequency between fx and fy determines the frame rate. The resonant frequency of a fiber cantilever with a round cross-section has the following form: [160,161]

$$f = \frac{\beta}{4\pi}\left(\frac{E}{\rho}\right)^{\frac{1}{2}}\left(\frac{R}{L^2}\right) \quad (8.1)$$

Where E is the Young's modulus and ρ is the mass density. These two factors are determined by the material and the mater'al's morphology. β is a constant which equals 3.52, according to Ref. [161]. L and R are the fiber cantilever's length and radius. Compared to Ref. [109], I only changed the fiber length and fiber radius in our experiment to L=188mm, R=240μm, resulting in a resonant frequency of 380Hz.

8.2 General design layout of fiber-optic confocal microscope

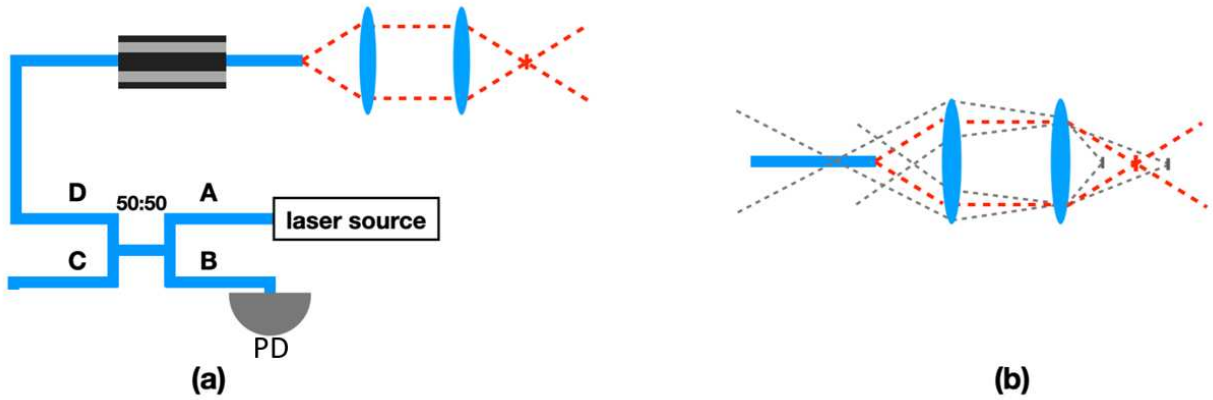

Figure 8.1: The layout of fiber-optic confocal microscope (a) Confocal probe head layout: 50/50 beam splitter let 50% of the laser source power to shine on the sample and let 50% of the reflected light from the sample to be detected by the Pd. the end of the scanning fiber cantilever serves as a pinhole to reject out-of-focus light. (b) illustrative figure to show how does the fiber end to reject out-of-focus reflected light. PD: photodetector 50:50: 50/50 beam splitter

The general system diagram of Scanning Fiber Confocal Microscopy (SFCM) is shown in Fig.8.1(a). A CW laser source (785nm, 10mW) is coupled into port A of a fiber-based 50/50 beam splitter. Therefore, 50% of the laser power is diverted to port C and abandoned. The other 50% couples into port D for later sample illumination. The illumination light from port D is then coupled into another SMF (P1-780Y-FC-1), anchored at the center of a PZT actuator distal end (TB1005). A segment of free fiber cantilever from the very same SMF that extends out of the PZT can be driven by the PZT at the cantilever's resonant frequency. Selecting the relative phase between sinusoidal driving voltages applied to x and y direction, the fiber tip can scan with a Lissajous pattern. The scanning pattern then can be imaged onto the conjugate plane of the fiber tip through a 4f lens assembly. If a tiny reflector is in focus, the reflected light will trace back the same optical path and then couple back to the same SMF and the fiber-based beam splitter. Lastly, 50% of the sample reflection is coupled to port B and detected by the photodetector.

Fig.8.1 (b) shows three different circumstances corresponding to a reflector located in front of the focal point, at the focal point, and behind the focal point, respectively. When considering these

three cases, the fiber scan is halted, and only one instant confocal imaging process is to be inspected. When the reflector is located in the front or after the focal point (marked as two grey bricks), the specular reflection beam forms a focal point before or after the fiber distal end. In these two cases, even though a small portion of reflected power still shines onto the distal end of the SMF, the incident angle of this portion of the back reflection beam exceeds the SMF critical angle, thus cannot pass through the SMF or be detected, let alone the majority portion of back reflection that does not even shine on the fiber end. Only the in-focus reflector (marked as red brick) can generate a reflection beam that can pass through the SMF and be detected by the signal photodetector. Or in other words, the SMF distal end serves as the pinhole to reject the reflection from sample slices that are out of focus, only passing the reflection from the in-focus sample point.

8.3 Optical properties of confocal reflectance microscope

The most significant merit of confocal microscopy is the out-of-focus background rejection which improves the image contrast and offers optical sectioning ability. Meanwhile, the resolution of confocal is slightly improved compared to conventional imaging modalities. This resolution improvement arises from the nature of illumination and detection processes executed by the same optical lens assembly. Thus the overall three-dimensional point spread function (PSF) of confocal microscopy is the product of two identical PSF, corresponding to illumination PSF and detection PSF, respectively:

$$PSF_{\text{confocal}}(x, y, z) = PSF(x, y, z) \times PSF(x, y, z) \quad (8.2)$$

Whereas the commonly used illumination methods in conventional microscopy do not make use of a focused illumination beam. In coherent Kohler illumination, for instance, a coherent point source is collimated by a condenser lens. The resultant coherent plane wave then illuminates the

entire sample plane evenly. Therefore, the illumination process does not produce a PSF. The PSF of such microcopy only reflects the objective lens ability to collect the point emissions from the sample.

In confocal microscopy, the product of two PSFs leads to an enhancement in both lateral resolution and axial resolution:

$$r_{lateral} = \frac{0.41\lambda}{\mathrm{NA}}, r_{axial} = \frac{1.4\lambda n}{\mathrm{NA}^2} \quad (8.3)$$

Where n is the medium refractive index, λ illumination wavelength, and NA is the objective lens numerical aperture.

Contrast is another important property to characterize a confocal microscope. Contrast is a metric used to describe an optical system's ability to resolve two adjacent emitters' intensity with the consideration of stray light background and detection of electronic noise. Lower contrast prohibits access to the full available optical resolution. An optical system's contrast is:

$$C = \frac{I_{bright} - I_{dim}}{I_{bright} + I_{dim}} \quad (8.4)$$

Where I_{bright} is the intensity of the brighter emitter and I_{dim} is the intensity of the dimmer emitter. This notation is also called visibility by Michelson and many others. It has a maximum of 1 when the relative intensities between bright and dim emitters can be fully resolved and a minimum of 0 when the relative intensities cannot be resolved at all due to stray light background or detection noise. Here, we will only focus on optical analysis, so the detection noise sources, such as shot noise and Johnson noise, will be ignored. Yet readers need to remember that the detection noise always degrades the final image contrast. Since stray light intensity is not signal but present in

both measured bright and dim emitter intensities, we can rewrite the I_{bright} and I_{dim} as the sum of the signal intensity and the stray light background intensity:

$$I_{bright} = I_{b,sig} + I_b \,, \qquad I_{dim} = I_{d,sig} + I_b \quad (8.5)$$

Combining this with Eq. 8.4 results in a contrast measure that accounts for the background effect:

$$C = \frac{I_{b,sig} - I_{d,sig}}{\sqrt{I_{b,sig}^2 + I_{d,sig}^2 + 2I_b^2}} \quad (8.6)$$

From this, one can notice that the larger the stray light background is, the lower the contrast will be. In conventional microscopy, reflection from all the reflectors in the illumination beam will contribute to the detected intensity. Those out-of-focus reflectors will be superimposed to cause a very large background intensity, I_b, which not only degrades the contrast but also prohibits the optical sectioning. In a fiber-optic confocal microscope, fiber-end rejection and laser scanning mitigate the background. The fiber-end rejects the out-of-focus reflection background. The laser scanning mechanism mitigates the background raised from adjacent reflectors by illuminating one point at a time.

Yet fiber-based confocal microscopy always suffers from one background source: the back reflection from the fiber distal end. Many researchers have explored methods to attenuate this problem.

Confocal microscopy detects the back-reflection photons from the biological tissue. The reflectivity of the biological tissue is at the scale of 20%~50%[162–164] in the visible to NIR range. This low reflectivity is due to the absorption and transmissivity of the tissue. What's more, the scattering from the fine structures of the tissue can further divert reflected photons to multiple directions. That degrades the amount of detectable direct reflected photons even more. Therefore,

for most the fiber-conducted confocal microscopes, it is crucial to eliminate any other form of the direct back-reflection. Otherwise, these unwanted back-reflections would lead to a sample-independent background, dramatically decreasing the confocal image contrast.

One of the major factors contributing to this background is the back-reflection from the cleaved distal fiber end. When the light exits from the fiber to the air, the index-mismatched interface between fiber and air leads to partially reflected photons back into the same fiber, propagating towards the detector. The typical glass-air reflection is 4%. Meanwhile muscle tissue back-reflection is around 20% to 40%. Even though the muscle tissue back reflection is still 5X to 10X larger than the fiber-air surface reflection, attenuation of fiber-end reflection is still crucial considering the highly scattering inside the tissue and larger penetration depth requirement. Generally speaking, there are three methods to attenuate the fiber end reflection in fiber-based confocal microscopy, 8-degree cleave angle, utilization of orthogonally polarized illumination and detection, and index matching.

8-degree cleave angle: The distal fiber end can be cleaved to 8 degrees so that the angle of back reflection from the fiber end will exceed the fiber critical angle. Therefore, the back-reflected photons cannot propagate within the same fiber back to the detector. It is known that angle physical contact (APC) fiber single-mode connector, in which the fiber end is polished to have an 8-degree angle, offers <-65dB fiber end reflection. In comparison, other connector forms have much larger fiber end reflection, such as -55dB for Ultra Physical Contact (UPC), -35dB for Physical Contact (PC), and -30dB for a flat polished connector. The information is from the website [165].

Ning Zhang and his colleagues[166] have developed a compact fiber scanning probe for OCT endoscopy. Inside their design, the quadruple PZT drives a single-mode fiber (SMF) segment at the mechanical resonance of the free cantilever fiber end and serves as the illumination and

collection unit. With 35V driving voltage amplitude on the PZT, 0.9mm fiber end deflection has been achieved, which has led to a 1.2mm image field diameter and 0.6mm spot size. To minimize the fiber end back-reflection background, the fiber end is angle cleaved at 8 degrees. Their Swept-Source Optical Coherence Tomography (SS-OCT) sensitivity was 95dB with 18mW laser power. In vivo human skin and ex vivo human colon specimens OCT images have been achieved, indicating that the angle cleaved the fiber end can attenuate the back-reflection background low enough for the tissue imaging.

Polarization-sensitive illumination and detection: When trying to attenuate fiber end back-reflection through an SMF with 8-degree cleave angle, an expensive fiber cleaver (F-CLX-8-3) is required. Fortunately, utilizing orthogonally polarized illumination and detection provides us with another cost-efficient method. In this method, one polarization maintained (PM) single-mode fiber (SMF), one polarized beam splitter (PBS), and one quarter waveplate are needed. The quarter waveplate is placed right between the fiber end and the sample. The PBS reflects the p polarized illumination laser into the PM SMF. Both reflected and transmitted beams appear at the distal end of this fiber. The reflected beam from this fiber end is still p polarized. Yet the transmitted beam will propagate to the sample plane, generate the back-reflection photons from the sample, then back to the distal fiber end. During this process, the transmitted beam double passes the quarter waveplate. Therefore, its polarization becomes s polarized. When both the fiber end back reflection beam and the sample back reflection beam go through the same PM SMF to the PBS, only s polarized sample reflection beam can pass through the PBS and on to the detector. This method can easily reject over 95% of the unwanted back reflection, assuming the sample back reflection is pure s polarized. Yet, in reality, many mechanisms can degrade the pure s polarization state,

such as non-normal incidence onto the quarter waveplate and birefringent properties of the interrogated sample.

Such a method has been employed by Hyun-Joon Shin[167,168] and Lin Liu [168] to enhance their image contrast in MEMS-based confocal microscopy. Instead of using a PZT-driven free fiber cantilever to realize a 2D scan, they used microelectromechanical system (MEMS) scanning mirrors. Hyun-Joon Shin achieved 2D confocal images from a human oral biopsy sample with 9.55 μm axial resolution, 0.83 μm transverse resolution, and FOV of 140μm×70μm. The strongly scattering nuclei have been identified. With the eight frames per second imaging speed, they could inspect cell dynamics.

On the other hand, Lin Liu not only utilized a MEMS mirror scanner but also built another MEMS lens scanner to fulfill the depth scanning. Compared to Hyun-Joon Shin's work, Lin Liu's design can form a 3D image. With a miniature high NA lens attached to the homemade MEMS lens scanner, a 400μm depth scan was realized, along with the transverse field of view (FOV) provided by the MEMS mirror scanner, she was able to achieve a 3D image stack from a mouse brain tissue with 180μm×180μm×380μm volume.

Index matching: The back-reflection of the fiber end originates from the index mismatch between fiber core and air. This unwanted background can be attenuated if the exiting light from the fiber core propagates into a medium with the same refractive index (RI) as the fiber core. Therefore, another background attenuation method is using index matching oil to fill up the space between fiber and the objective lens. Pierre M. Lane has thoroughly studied this method [169]. Based on Fresnel reflection theory, he built a model to explicitly elaborate the terminal RI dependence of fiber end back-reflection for step-index fiber and graded-index fiber separately. The model also

includes the effects of fiber geometry and incident light wavelength. A -35dB minimum back-reflection has been experimentally demonstrated with the predicted optimal terminal RI.

Chen Liang et al.[170] employed such a method to attenuate the background radiation originated from the distal and proximal faces of the fiber bundle being used in their fiber confocal reflectance microscope (FCRM). The matching oil with fiber core RI has been used to immerse the distal fiber face. Meanwhile, the proximal fiber face is immersed in the matching oil with average RI of cladding and core. Afterward, cooperating with the residual constant background subtraction, FCRM is able to detect the signal arising from a 0.05 RI mismatch, which translates to 0.0034% Fresnel reflectance between plasma and cell nucleus. However, their laser scanning mechanism utilizes two scanning mirrors for scanning a focused laser beam across the proximal face of the fiber bundle. Then the laser light coupled into the fiber bundle transmits the scanning pattern on the distal face. Lastly, the very same scanning pattern is projected onto the sample plan with the aid of a coupling lens assembly and an objective lens. Because of the viscosity of the fluid, however, this index matching method is not suitable for the piezo-scanned resonant fiber cantilever geometry.

8.4 Experimental procedure

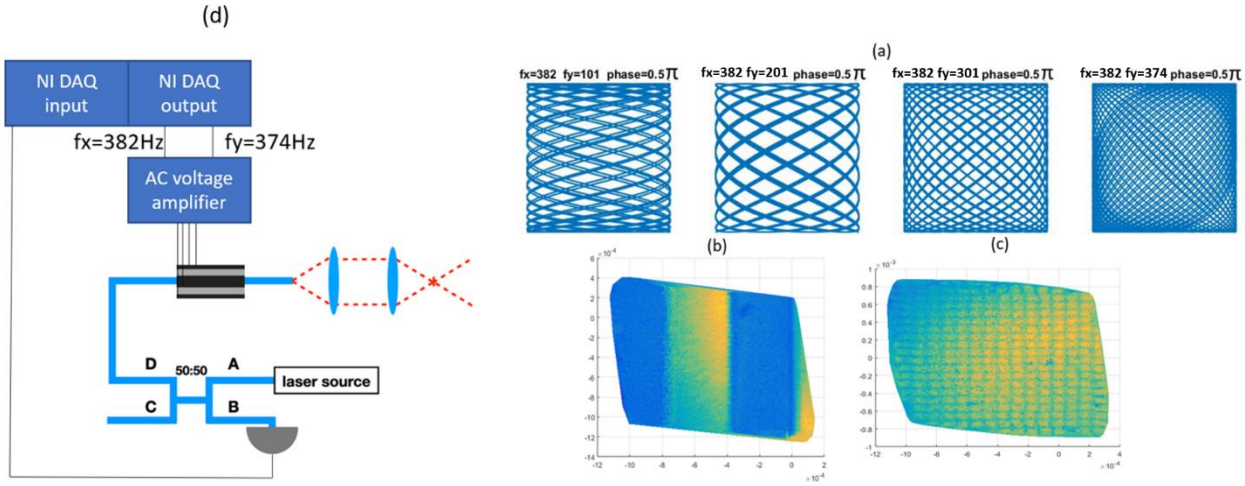

Figure 8.2: experimental set up. (d) the PZT is driven at two amplified AC voltages, 382Hz and 374Hz respectively. Fiber cantilever attached to it starts to generate Lissajous scanning pattern. A 4f system projects this pattern onto the sample. the fiber based 50/50 beam splitter is in charge of transfer laser to the scanning fiber end and read in the reflected signal through the same fiber end. The scanning fiber cantilever end works as the pinhole in confocal microscope that reject out of focus reflected light. (a) Matlab simulation on exploring the scanning frequencies to realize larger filling factor. (b) reflected confocal image of a resolution card. (c) reflected confocal image of a PSD sensor surface.

The experimental setup is shown in Fig. 8.2(d). A 532nm laser diode (DJ532-10 Thorlabs) is the laser source. After a 50/50 fiber-based beam splitter, 50% of the input laser power goes to port D and is coupled into the scanning fiber. Then a 4f imaging system projects the scanning fiber end to the sample plane, generating a Lissajous scanning pattern. The reflected laser from the sample then goes through the same scanning fiber end and beams splitter. Finally, 50% of the reflected laser light is detected by the photodetector at port B. then, the photodetector signal is recorded by the NI DAQ input to form images. The scan pattern is controlled by the NI DAQ outputs, fed into an AC voltage amplifier built by William Hudson. Through the voltage amplifier, we can drive opposite electrodes of PZT differentially with a max voltage over 300V. One pair executes x scanning, and the other executes y scanning. For these experiments, the AC voltage was fixed at a

50V amplitude. The frequency was tuned adjacent to the theoretical resonance of 380Hz, finding that 382Hz offered the largest scanning pattern. For the Lissajous pattern, we set f_x=382Hz and used Matlab to alter f_y to maximize the filling factor, as shown in Fig. 8.2 (a). In the end, I selected f_x=382Hz and f_y=374Hz. I programmed the two outputs of the NI DAQ to generate two sine voltage outputs, with an initial phase difference of $\pi/2$.

Imaging results are shown in Fig. 8.2 (b) (resolution card) and Fig. 8.2 (c) (surface of a position sensing detector). My work so far demonstrates this system can form confocal images. But it needs more investigation to achieve the largest FOV and finest resolution.

One last thing to notice, the actual scan position does not follow the exact x and y instantaneous driving voltage. To form images, we had to follow the calibration procedure from Eric Seibel's lab[158,159,171]. Briefly speaking, a position sensing detector (PSD) (PDP90A) is placed at the sample plane to record x- and y- positions of the focal spot during scanning. Then MATLAB's `griddata()` function is used to reconstruct the reflected confocal image based on the recorded information. One critical aspect of minimizing noise from the PSD is to normalize the x and y outputs by the sum pin (special thanks to Nathan You, an undergraduate researcher in our lab, for working this out).

Chapter 9. Prospect and future directions

The biggest limitation of our system is still SNR, which affects not only imaging speed but also obtainable resolution. Considering the TAM imaging transfer function as approximately Gaussian, noise will overwhelm the weaker high-frequency components before the stronger low-frequency components (see Fig 6,2), in effect blurring out the high-frequency details. The primary source of noise in our system is the electronics, which currently have a noise floor far above the shot noise. This is not so concerning for crystals and other materials that are resistant to photodamage and have a strong TA signal, since we can increase laser power to boost the signal level. Yet for biological samples, more power is not an option, and so we must lower the noise floor. The extra amount of electronic noise is primarily due to the fact that the photodiode and power supply are not packaged compactly together. One route to shot noise-limited detection would be to use a tuned amplifier (TAMP), which was developed by Ji-Xin Cheng's group [172]. Experiments with this detector for SRS imaging have shown improvement of SNR from 6 to 50.

What's more, squeezed light could reduce the noise floor even below the shot-noise limit. Recently, Warwick P. Bowen's lab used squeezed light to lower the SRS noise floor by 15dB below the shot-noise limit[173–175]. Briefly speaking, the phase and amplitude of light follow the uncertainty product given by Heisenberg's uncertainty relation[176]. This approach sacrifices phase detection accuracy to enhance amplitude detection accuracy through amplitude squeezing of the solid-state laser output. The only critical optical components needed to realize squeezing light are a solid-state ultrafast laser source and a periodically poled $KTiOPO_4$ crystal. If applied to our current system, this could lower the noise floor to 15dB below the shot-noise limit.

The next limitation to be addressed is optical resolution[175,176]. Since mitochondria's typical size is from 0.5 to 3μm, to observe sub-mitochondrial structures, we need nanoscale resolution. The well-known super-resolution imaging techniques, such as PALM STED STORM[177–180], can achieve such resolution, but the question is how to achieve super-resolution with TAM[181].

On the other hand, P. James Schuck's group[182] took another path. They designed one kind of fluorophore with very high nonlinearities[183–185] and achieved high resolution through high-order nonlinear optical effects. A comparison between these approaches is listed in Table 2.

Dr. Gustafsson's group[106] from the University of California, San Francisco, developed a microscopic method called saturated structured-illumination microscopy (SSIM) that combines the structured-illumination approach with the high-frequency harmonics introduced by saturation. The response of a fluorophore driven into saturation with a sine wave will be sinusoidal emission that is clipped at the top. The time-domain clipping, in the Fourier domain, is represented by a comb of harmonics. In principle, we will observe an infinite number of harmonics, which implies an infinitesimal resolution, limited by SNR. Gustafsson's group used SSIM to achieve <50nm resolution on sufficiently bright and photo-stable samples.

	Conventional	Confocal/TAM	SIM	STED	PALM	STORM	SSIM[106]	photo avalanching nanoparticles [182]
Rayleigh criterion (lateral)	0.61λ/NA	0.4λ/NA	0.4λ/(2NA)					$\frac{0.61\lambda}{NA\sqrt{s}}$ s is the number of photons involved in the process

$R_{lateral}$(nm) NA=0.5	600	400	200	30~70	10~50	10~55	50	Sub-70

Table 2: optical resolution comparison between Super-resolution Techniques.

This approach can be extended to non-fluorescent TAM imaging through either saturation[181] or other pump nonlinearities[100]and I propose here it can also be combined with structured illumination.

A microscopic system's maximum detectible spatial frequency is determined by the numerical aperture NA and laser wavelength $k_0 = \frac{2NA}{\lambda}$. The observable region in the spatial frequency domain defined by that is a circle with radius k_0 around the origin. Any frequency components outside this circle are cut off by the imaging system. SIM is a method to render some these high-frequency features observable by the imaging system again. It downconverts high-frequency components of the sample into the observable circular region in the form of Moire fringes. Moire fringes are generated by multiplying the local sample density and the local illumination intensity pattern. If the illumination pattern has a spatial frequency of k_1, the Moire fringes will have a spatial frequency that equals the difference frequency $k- k_1$, where k is the sample spatial frequency. Now, if $|k- k_1|<k_0$, the high sample spatial frequency k, which was beyond the observable region, is downconverted to be within the area that can be detected by the system, increasing the highest detectable spatial frequency from k0 to k_0+k_1[106]. Resolution is ultimately limited by the diffraction limit of the illumination pattern, which limits k1 to be less than $\frac{2NA}{\lambda}$, which implies that the normal, linear SIM can extend the resolution by a factor of 2[106]. But after combining SIM with a nonlinearity, one can achieve higher resolution, limited only by SNR[186].

Fig.9.1 shows a simulation of structured illumination. The basic idea is that the structural illumination downconverts higher frequency to lower frequency adjacent to DC. So that the objective lens can observe those initially high-frequency components. In the simulation, you can

see if using patterned illumination to shine on a square-shaped object (Fig.9.1(a)), the high-frequency region is down-converted to DC (Fig.9.1(b)). This downconverted region is numerically placed into the higher frequency region where it belongs (Fig.9.1(c)). Then an inverse FFT transforms back to the spatial domain. The illumination pattern can be rotated by changing the relative modulation frequency in the x and y-direction. By varying rotation angle illumination pattern frequency, we sample the entire reachable k-space outside the imaging system's bandwidth. These images are then superimposed to produce a high-resolution image (Fig.9.1(d)). The resulting frequency region (Fig.9.1(e)) is two times larger in radius than the objective lens supported region. Fig.9.1(f) shows the original image as a comparison.

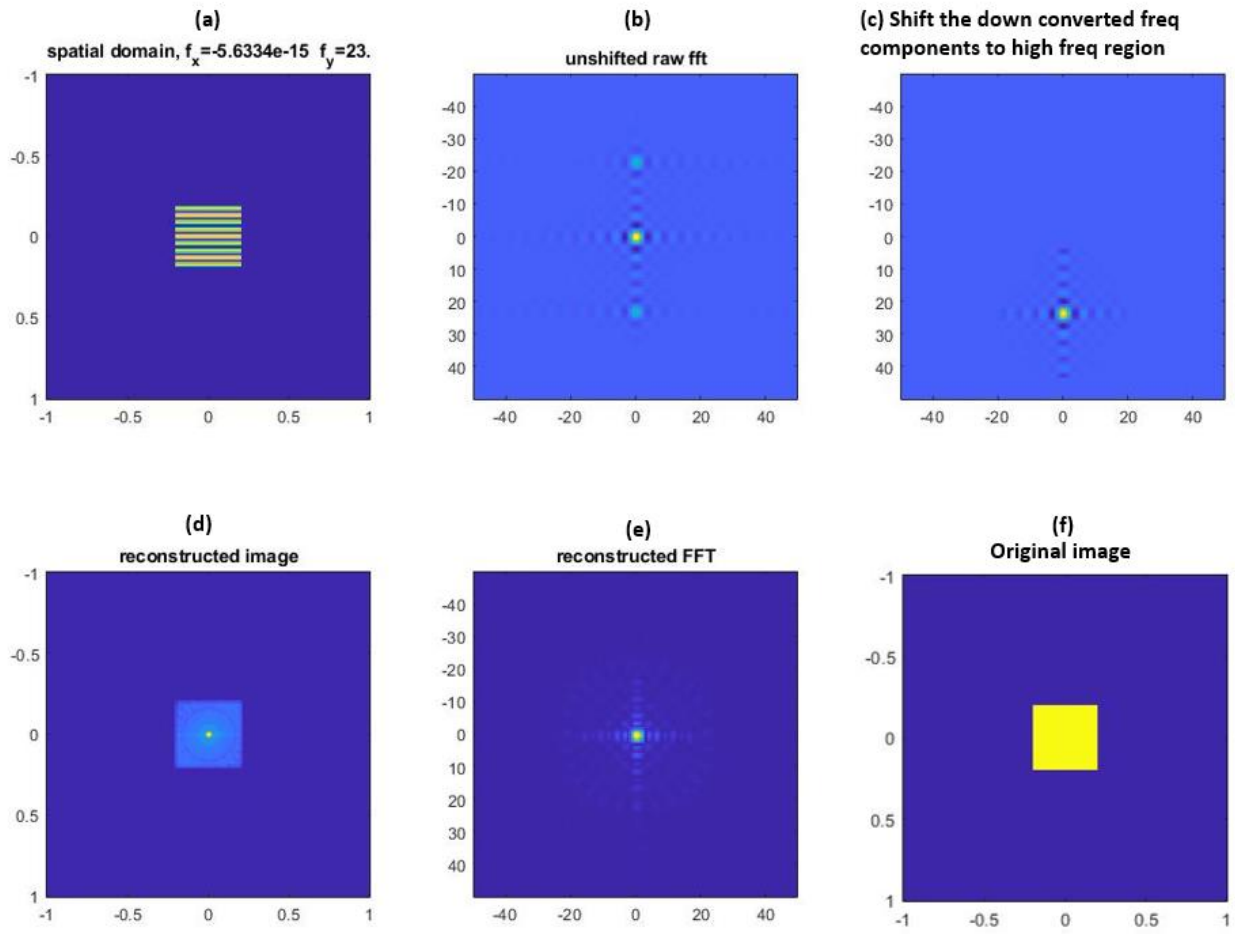

Figure 9.1: Structural illumination simulation (a) illumination pattern on a square-shaped object, illumination pattern can rotate by changing the ratio of f_x and f_y. The fringe frequency increases as the sum frequency $f=f_x^2+f_y^2$ increases. (b) Unshifted FFT of the object illuminated by one particular pattern. This is the down converted version of the original high object spatial frequency component. (c) bring the down converted version back to where it belongs. (d)(e) reconstructed image in spatial domain and frequency domain. (f) original image

Instead of using two plane wave interference to generate the illumination pattern, which is applicable mainly for wide-field microscopic illumination systems, a laser scanning microscope can make use of an acousto-optic-modulator (AOM) to generate the illumination patterns. Hyunwoo Kim et al. [187] has already reported a Lissajous scanning SIM (LS-SIM) using one Lissajous scanning micromirror and AOM induced laser beam modulation. By choosing the correct x and y scanning frequencies of the Lissajous micromirror and modulation frequency from AOM, they can rotate the SIM scanning pattern and achieve enhanced resolution, even in a linear

microscopic methods. We anticipate this scanning mechanism can also enhance the resolution of transient absorption microscopy.

References

1. M. J. Rosker, M. Dantus, and A. H. Zewail, "Femtosecond real-time probing of reactions. I. The technique," The Journal of Chemical Physics **89**(10), 6113–6127 (1988).

2. A. J. Demaria, D. A. Stetser, and H. Heynau, "Self mode-locking of lasers with saturable absorbers," Applied Physics Letters **8**(7), 174–176 (1966).

3. D. A. Stetser and A. J. Demaria, "Optical spectra of ultrashort optical pulses generated by mode-locked glass:nd lasers," Applied Physics Letters **9**(3), 118–120 (1966).

4. Walter Koechner, *Solid-State Laser Engineering*, 6th ed. (Springer, New York, NY, 2006).

5. U. Keller, "Ultrafast solid-state laser oscillators: A success story for the last 20 years with no end in sight," Applied Physics B: Lasers and Optics **100**(1), 15–28 (2010).

6. D. J. Kuizenga and A. E. Siegman, "FM and AM Mode Locking of the Homogeneous Laser—Part I: Theory," IEEE Journal of Quantum Electronics **6**(11), 694–708 (1970).

7. E. P. Ippen, H. A. Haus, and L. Y. Liu, *Additive Pulse Mode Locking* (1989), **6**(9).

8. D. H. Sutter, G. Steinmeyer, L. Gallmann, N. Matuschek, F. Morier-Genoud, U. Keller, V. Scheuer, G. Angelow, and T. Tschudi, *Semiconductor Saturable-Absorber Mirror-Assisted Kerr-Lens Mode-Locked Ti : Sapphire Laser Producing Pulses in the Two-Cycle Regime* (1999), **24**.

9. D. J. Kuizenga and A. E. Siegman, "FM and AM Mode Locking of the Homogeneous Laser—Part I: Theory," IEEE Journal of Quantum Electronics **6**(11), 694–708 (1970).

10. D. J. Kuizenga and A. E. Siegman, "FM and AM Mode Locking of the Homogeneous Laser—Part Ii: Experimental Results in a Nd: YAG Laser with Internal FM Modulation," IEEE Journal of Quantum Electronics **6**(11), 709–715 (1970).

11. U. Keller, D. A. B. Miller, G. D. Boyd, T. H. Chiu, J. F. Ferguson, and M. T. Asom, *Solid-State Low-Loss Intracavity Saturable Absorber for Nd:YLF Lasers: An Antiresonant Semiconductor Fabry-Perot Saturable Absorber* (1992), **17**(7).

12. H. A. Haus, "Parameter Ranges for CW Passive Mode Locking," IEEE Journal of Quantum Electronics **12**(3), 169–176 (1976).

13. D. E. Spence, J. M. Evans, W. E. Sleat, W. Sibbett, and J. E. Allen, *Regeneratively Initiated Self-Mode-Locked Ti:Sapphire Laser* (1991), **16**(22).

14. D. E. Spence, P. N. Kean, W. Sibbett, and J. F. Allen, *60-Fsec Pulse Generation from a Self-Mode-Locked Ti:Sapphire Laser* (1991), **16**(1).

15. J. M. Evans, D. E. Spence, W. Sibbett, J. F. Allen, B. H. T. Chai, and A. Miller, *50-Fs Pulse Generation from a Self-Mode-Locked Cr:LiSrAlF 6 Laser* (1992), **17**(20).

16. J. M. Evans, D. E. Spence, D. Burns, W. Sibbett, and J. F. Allen, *Dual-Wavelength Self-Mode-Locked Ti:Sapphire Laser* (1993), **18**(13).

17. V. Magni, G. Cerullo, and S. de Silvestri, *Matrix Analysis of Propagation of Gaussian Beams through Kerr Media* (1993).

18. V. Magni, G. Cerullo, and S. de Silvestri, *Closed Form Gaussian Beam Analysis of Resonators Containing a Kerr Medium for Femtosecond Lasers* (1993), **101**.

19. U. Keller and T. H. Chiu, "Resonanat passive mode-locked Nd:YLF laser," IEEE Journal of Quantum Electronics **28**(7), 1710–1721 (1992).

20. U. Keller, "Ultrafast solid-state laser oscillators: A success story for the last 20 years with no end in sight," Applied Physics B: Lasers and Optics **100**(1), 15–28 (2010).

21. A. Chong, J. Buckley, W. Renninger, and F. Wise, "All-normal-dispersion femtosecond fiber laser," Optics Express (2006).

22. Joel Buckley, "HIGH-ENERGY ULTRAFAST YTTERBIUM FIBER LASERS ," Cornell University (2006).

23. A. H. Zewail, "Femtochemistry: Atomic-scale dynamics of the chemical bond," Journal of Physical Chemistry A **104**(24), 5660–5694 (2000).

24. Jin Yu, Warren S. Warren, and Martin C. Fischer, "Spectroscopic Differentiation and Microscopic Imaging of Red Organic Pigments Using Optical Pump–Probe Contrast," Anal. Chem **90**(21), 12686–12691 (2018).

25. D. Fu, T. Ye, T. E. Matthews, G. Yurtsever, and W. S. Warren, "Two-color, two-photon, and excited-state absorption microscopy," Journal of Biomedical Optics **12**(5), 054004 (2007).

26. Thomas E. Matthews, Jesse W. Wilson, Simone Degan, Mary Jane Simpson, Jane Y. Jin, Jennifer Y. Zhang, and Warren S. Warren, "In vivo and ex vivo epi-mode pump-probe imaging of melanin and microvasculature," BIOMEDICAL OPTICS EXPRESS **2**(6), 1576–1583 (2011).

27. Francisco E. Robles, Jesse W. Wilson, Martin C. Fischer, and Warren S. Warren, "Phasor analysis for nonlinear pump-probe microscopy," Optics Express **20**(15), 17082–17092 (2012).

28. Masud Mansuripur, *Field, Force, Energy and Momentum in Classical Electrodynamics (Revised Edition)* (Bentham Science Publishers, 2017).

29. M. Born, E. Wolf, A. B. Bhatia, P. C. Clemmow, D. Gabor, A. R. Stokes, A. M. Taylor, P. A. Wayman, and W. L. Wilcock, *Principles of Optics* (Cambridge University Press, 1999).

30. K. M. Farrell, N. Yang, M. T. Zanni, and G. Engel, "A polarization scheme that resolves cross-peaks with transient absorption and eliminates diagonal peaks in 2D spectroscopy," (2022).

31. M. Cho, *Two-Dimensional Optical Spectroscopy* (Taylor & Francis Group, LLC, 2009).

32. S. Mukamel, *Principles of Nonlinear Optical Spectroscopy* (Oxford University Press, 1995).

33. Geoffery New, *Introduction to the Nonlinear Optics* (Cambridge University Press, n.d.).

34. Geoffrey New, "Stimulated Raman scattering," in *Introduction to Nonlinear Optics* (Cambridge University Press, 2011), pp. 87–90.

35. H. E. Lessinc-, A. Yon, and J. M. Reichert, *ORIENTATIONAL ASPECT OF TRANSIENT ABSORPTION iN SOLUTIONS* (n.d.), **36**(4).

36. R. M. Hochstrasser, *Two-Dimensional IR-Spectroscopy: Polarization Anisotropy E€ects* (n.d.).

37. A. B. Myers and R. M. Hochstrasser, "Comparison of Four-Wave Mixing Techniques for Studying Orientational Relaxation," IEEE Journal of Quantum Electronics **22**(8), 1482–1492 (1986).

38. P. Hamm and M. Zanni, *Concepts and Methods of 2D Infrared Spectroscopy* (Cambridge University Press, 2011).

39. C. T. Kuhs, B. M. Luther, and A. T. Krummel, "Recent Advances in 2D IR Spectroscopy Driven by Advances in Ultrafast Technology," IEEE Journal of Selected Topics in Quantum Electronics **25**(4), (2019).

40. M. A. Ansari, M. Erfanzadeh, and E. Mohajerani, *Mechanisms of Laser-Tissue Interaction: II. Tissue Thermal Properties* (2013), **4**.

41. M. Ganguly, R. O'flaherty, A. Sajjadi, and K. Mitra, *Tissue Response to Short Pulse Laser Irradiation* (n.d.).

42. S. R. Domingue, A. J. Chicco, R. A. Bartels, and J. W. Wilson, "Pump-probe microscopy of respiratory chain pigments: towards non-fluorescent label-free metabolic imaging," in *Multiphoton Microscopy in the Biomedical Sciences XVII* (SPIE, 2017), **10069**, p. 100691P.

43. D. B. Rodrigues, P. F. Maccarini, S. Louie, E. Colebeck, E. Topsakal, P. J. S. Pereira, P. Limão-Vieira, and P. R. Stauffer, "Numerical 3D modeling of heat transfer in human tissues for microwave radiometry monitoring of brown fat metabolism," in *Energy-Based Treatment of Tissue and Assessment VII* (SPIE, 2013), **8584**, p. 85840S.

44. Dan Fu, "Developing Novel Nonlinear Optical Contrast for Biomedical Imgaging," Princeton University (2009).

45. N. R. C. S. Designed Research; M, *In Vivo Multiphoton Microscopy of NADH and FAD Redox States, Fluorescence Lifetimes, and Cellular Morphology in Precancerous Epithelia* (1949), **104**(49).

46. S. Huang, A. A. Heikal, and W. W. Webb, "Two-photon fluorescence spectroscopy and microscopy of NAD(P)H and flavoprotein," Biophysical Journal **82**(5), 2811–2825 (2002).

47. Y. Qin and Y. Xia, "Simultaneous Two-Photon Fluorescence Microscopy of NADH and FAD Using Pixel-to-Pixel Wavelength-Switching," Frontiers in Physics **9**, (2021).

48. Martin Gouterman, Georges H.Wagnière, and Lawrence C.Snyder, "Spectra of porphyrins: Part II. Four orbital model," Journal of Molecular Spectroscopy **11**(1–6), 108–127 (1962).

49. Martin Gouterman, "Spectra of porphyrins," Journal of Molecular Spectroscopy **6**, 138–163 (1961).

50. C. Zang, J. A. Stevens, J. J. Link, L. Guo, L. Wang, and D. Zhong, "Ultrafast proteinquake dynamics in cytochrome c," J Am Chem Soc **131**(8), 2846–2852 (2009).

51. M. Gouterman, G. H. Wagnière, and L. C. Snyder, "Spectra of porphyrins: Part II. Four orbital model," Journal of Molecular Spectroscopy **11**(1), 108–127 (1963).

52. H. C. Longuet-Higgins, C. W. Rector, and J. R. Platt, "Molecular Orbital Calculations on Porphine and Tetrahydroporphine," The Journal of Chemical Physics **18**(9), 1174 (1950).

53. U. Bobinger, R. Schweitzer-Stenner, and W. Dreybrodt, *Investigation of Asymmetric Perturbations of Nickel(II) Octaethylporphyrin in CH2CI2 by Raman Dispersion Spectroscopy* (1991), **95**.

54. R. Schweitzer-Stenner, *Polarized Resonance Raman Dispersion Spectroscopy on Metalporphyrins* (n.d.).

55. Ira N. Levine, *Quantum Chemistry*, 7th ed. (Pearson, n.d.).

56. O. Bräm, C. Consani, A. Cannizzo, and M. Chergui, "Femtosecond UV studies of the electronic relaxation processes in cytochrome c," Journal of Physical Chemistry B **115**(46), 13723–13730 (2011).

57. S. R. Domingue, R. A. Bartels, A. J. Chicco, and J. W. Wilson, "Transient absorption imaging of hemes with 2-color, independently tunable visible-wavelength ultrafast source," Biomedical Optics Express **8**(6), 2807 (2017).

58. C. Consani, O. Bräm, F. van Mourik, A. Cannizzo, and M. Chergui, "Energy transfer and relaxation mechanisms in Cytochrome c," Chemical Physics **396**(1), 108–115 (2012).

59. Erkang Wang, Saurabh Gupta, and Jesse W Wilson, "Adaptive noise canceling for transient absorption microscopy," Journal of Biomedical Optics **25**(10), (2020).

60. E. Hogenauer, "An economical class of digital filters for decimation and interpolation," IEEE Transactions on Acoustics, Speech, and Signal Processing **29**(2), 155–162 (1981).

61. Burr-Brown Corporation, *Noise Analysis of FET Transimpedance Amplifiers* (1994).

62. S. Gupta, E. Wang, S. Derrien, and J. W. Wilson, "DR-RINS: Digital real-time relative intensity noise suppressor for pump-probe spectroscopy and microscopy," Review of Scientific Instruments **92**(2), (2021).

63. E. Wang, K. S. Specht, A. J. Chicco, and J. W. Wilson, "High-Repetition-Rate Transient Absorption Spectroscopy of Respiratory Supercomplexes," Journal of Physical Chemistry B **126**(7), 1404–1412 (2022).

64. E. R. Henry, W. A. Eaton, and R. M. Hochstrassert, *Molecular Dynamics Simulations of Cooling in Laser-Excited Heme Proteins (Picosecond Spectroscopy/Intramolecular Vibrational Relaxation/Raman Spectroscopy/Hemoglobin/Myoglobin)* (1986), **83**.

65. M. Negrerie, S. Cianetti, M. H. Vos, M. Jean-Louis, and S. G. Kruglik, "Ultrafast heme dynamics in ferrous versus ferric cytochrome c studied by time-resolved resonance Raman and transient absorption spectroscopy," Journal of Physical Chemistry B **110**(25), 12766–12781 (2006).

66. W. Wang, X. Ye, A. A. Demidov, F. Rosca, T. Sjodin, W. Cao, M. Sheeran, and P. M. Champion, "Femtosecond multicolor pump-probe spectroscopy of ferrous cytochrome c," Journal of Physical Chemistry B **104**(46), 10789–10801 (2000).

67. S. Singhal, S. Dinda, and D. Goswami, "Measurement of pure optical nonlinearity in carbon disulfide with a high-repetition-rate femtosecond laser," Applied Optics **56**(3), 644 (2017).

68. J. A. Enríquez, "Supramolecular Organization of Respiratory Complexes," Annual Review of Physiology **78**, 533–561 (2016).

69. Pooja Jha, Xu Wang, and Johan Auwerx, "Analysis of Mitochondrial Respiratory Chain Supercomplexes Using Blue Native Polyacrylamide Gel Electrophoresis (BN-PAGE)," Curr. Protoc. Mouse Biol. **6**, 1–14 (2016).

70. C. H. Le, L. G. Benage, K. S. Specht, L. C. Li Puma, C. M. Mulligan, A. L. Heuberger, J. E. Prenni, S. M. Claypool, K. C. Chatfield, G. C. Sparagna, and A. J. Chicco, "Tafazzin deficiency impairs CoA-dependent oxidative metabolism in cardiac mitochondria," Journal of Biological Chemistry **295**(35), 12485–12497 (2020).

71. N. Carlsson, C. C. Kitts, and B. Kerman, "Spectroscopic characterization of Coomassie blue and its binding to amyloid fibrils," Analytical Biochemistry **420**(1), 33–40 (2012).

72. S. R. Domingue, R. A. Bartels, A. J. Chicco, and J. W. Wilson, "Transient absorption imaging of hemes with 2-color, independently tunable visible-wavelength ultrafast source," Biomedical Optics Express **8**(6), 2807 (2017).

73. S. R. Domingue, R. A. Bartels, A. J. Chicco, and J. W. Wilson, "Transient absorption imaging of hemes with 2-color, independently tunable visible-wavelength ultrafast source," Biomedical Optics Express **8**(6), 2807 (2017).

74. J. M. Walker, *M E T H O D S I N M O L E C U L A R B I O L O G Y ™ Series Editor* (n.d.).

75. S. Portet, "A primer on model selection using the Akaike Information Criterion," Infect Dis Model **5**, 111–128 (2020).

76. A. de Juan, J. Jaumot, and R. Tauler, "Multivariate Curve Resolution (MCR). Solving the mixture analysis problem," Analytical Methods **6**(14), 4964–4976 (2014).

77. "c93b," (n.d.).

78. R. Tauler, A. Izquierdo-Ridorsa, and E. Casassas, "Simultaneous analysis of several spectroscopic titrations with self-modelling curve resolution.," Chemometrics and Intelligent Laboratory Systems **18**, 293–300 (1993).

79. L. D. Gauthier, J. L. Greenstein, S. Cortassa, B. O'Rourke, and R. L. Winslow, "A Computational model of reactive oxygen species and redox balance in cardiac mitochondria," Biophysical Journal **105**(4), 1045–1056 (2013).

80. J. J. Saucerman, "Modeling mitochondrial ROS: A great balancing act," Biophysical Journal **105**(6), 1287–1288 (2013).

81. Brechje J.van Beek-Harmsen and Willem J. van der Laarse, "Immunohistochemical Determination of Cytosolic Cytochrome c Concentration in Cardiomyocytes," Journal of Histochemistry & Cytochemistry **53**(7), 803–807 (2005).

82. B. J. van Beek-Harmsen and W. J. van der Laarse, "Immunohistochemical determination of cytosolic cytochrome c concentration in cardiomyocytes," Journal of Histochemistry and Cytochemistry **53**(7), 803–807 (2005).

83. Y. Hong, J. Muenzner, S. K. Grimm, and E. v. Pletneva, "Origin of the conformational heterogeneity of cardiolipin-bound cytochrome c," J Am Chem Soc **134**(45), 18713–18723 (2012).

84. J. Hanske, J. R. Toffey, A. M. Morenz, A. J. Bonilla, K. H. Schiavoni, and E. v Pletneva, "Conformational properties of cardiolipin-bound cytochrome c," (n.d.).

85. C. Govind, M. Paul, and V. Karunakaran, "Ultrafast Heme Relaxation Dynamics Probing the Unfolded States of Cytochrome c Induced by Liposomes: Effect of Charge of Phospholipids," Journal of Physical Chemistry B **124**(14), 2769–2777 (2020).

86. E. Wang, L. Whitcomb, A. Chicco, and J. Wilson, "Transient absorption spectroscopy and imaging of redox in muscle mitochondria," Biomedical Optics Express **13**(4), 2103–2116 (2022).

87. M. Yasuda, N. Takeshita, and S. Shigeto, "Inhomogeneous Molecular Distributions and Cytochrome Types and Redox States in Fungal Cells Revealed by Raman Hyperspectral Imaging Using Multivariate Curve Resolution-Alternating Least Squares," Analytical Chemistry **91**(19), 12501–12508 (2019).

88. M. Yasuda, N. Takeshita, and S. Shigeto, "Deuterium-labeled Raman tracking of glucose accumulation and protein metabolic dynamics in Aspergillus nidulans hyphal tips," Scientific Reports **11**(1), (2021).

89. S. Lu, W. Min, S. Chong, G. R. Holtom, and X. S. Xie, "Label-free imaging of heme proteins with two-photon excited photothermal lens microscopy," Applied Physics Letters **96**(11), (2010).

90. C. Zhang, Y. S. Zhang, D.-K. Yao, Y. Xia, and L. v. Wang, "Label-free photoacoustic microscopy of cytochromes," Journal of Biomedical Optics **18**(2), 020504 (2013).

91. P.-T. Dong, H. Lin, K.-C. Huang, and J.-X. Cheng, *Label-Free Quantitation of Glycated Hemoglobin in Single Red Blood Cells by Transient Absorption Microscopy and Phasor Analysis* (2019).

92. D. Fu, T. Ye, T. E. Matthews, B. J. Chen, G. Yurtserver, and W. S. Warren, *High-Resolution in Vivo Imaging of Blood Vessels without Labeling* (2007).

93. A. T. Francis, K. Berry, E. C. Thomas, A. H. Hill, and D. Fu, "In Vitro Quantification of Single Red Blood Cell Oxygen Saturation by Femtosecond Transient Absorption Microscopy," Journal of Physical Chemistry Letters **10**(12), 3312–3317 (2019).

94. D. Fu, T. E. Matthews, T. Ye, I. R. Piletic, and W. S. Warren, "Label-free in vivo optical imaging of microvasculature and oxygenation level," Journal of Biomedical Optics **13**(4), 040503 (2008).

95. A. T. Francis, M. J. Shears, S. C. Murphy, and D. Fu, "Direct Quantification of Single Red Blood Cell Hemoglobin Concentration with Multiphoton Microscopy," Analytical Chemistry **92**(18), 12235–12241 (2020).

96. A. J. Chen, X. Yuan, J. Li, P. Dong, I. Hamza, and J. X. Cheng, "Label-Free Imaging of Heme Dynamics in Living Organisms by Transient Absorption Microscopy," Analytical Chemistry **90**(5), 3395–3401 (2018).

97. J. D'Errico, "Surface Fitting using gridfit," https://www.mathworks.com/matlabcentral/fileexchange/8998-surface-fitting-using-gridfit.

98. C. Greene, "gridbin," https://github.com/chadagreene/gridbin.

99. B. Talone, M. Bazzarelli, A. Schirato, F. dello Vicario, D. Viola, E. Jacchetti, M. Bregonzio, M. T. Raimondi, G. Cerullo, and D. Polli, "Phototoxicity induced in living HeLa cells by focused femtosecond laser pulses: a data-driven approach," Biomedical Optics Express **12**(12), 7886 (2021).

100. Jesse W. Wilson, Miguel Anderson, Jong Kang Park, Martin C. Fischer, and Warren S. Warren, "Separating higher-order nonlinearities in transient absorption microscopy," in *Ultrafast Nonlinear Imaging and Spectroscopy III; 95840B (2015)* (SPIE, 2015).

101. L. Wang, Y. Zhang, Y. Wang, and P. Lai, "Video-rate dual-modal wide-beam harmonic ultrasound and photoacoustic computed tomography," IEEE Transactions on Medical Imaging **41**(3), 727–736 (2022).

102. Z. Zhang, Y. Shi, S. Yang, and D. Xing, "Subdiffraction-limited second harmonic photoacoustic microscopy based on nonlinear thermal diffusion," Optics Letters **43**(10), 2336 (2018).

103. A. Nehorai and B. Porat, "Adaptive Comb Filtering for Harmonic Signal Enhancement," IEEE Transactions on Acoustics, Speech, and Signal Processing **34**(5), 1124–1138 (1986).

104. M. Vondra and R. Vích, *Adaptive Comb Filtering in Speech Enhancement* (n.d.).

105. Erin E Flater, Arya C Mugdha, Saurabh Gupta, William A Hudson, Abbigail A Fahrenkamp, Jason P Killgore, and Jesse W Wilson, "Error estimation and enhanced stiffness sensitivity in contact resonance force microscopy with a multiple arbitrary frequency lock-in amplifier (MAFLIA)," Measurement Science and Technology **31**(11), (2020).

106. M. G. L. Gustafsson, *Nonlinear Structured-Illumination Microscopy: Wide-Field Fluorescence Imaging with Theoretically Unlimited Resolution* (2005).

107. National Research Council, *Guide for the Care and Use of Laboratory Animals: Eighth Edition* (The National Academies Press, 2011).

108. L. C. Li Puma, M. Hedges, J. M. Heckman, A. B. Mathias, M. R. Engstrom, A. B. Brown, and A. J. Chicco, "Experimental oxygen concentration influences rates of mitochondrial hydrogen peroxide release from cardiac and skeletal muscle preparations," American Journal of Physiology-Regulatory, Integrative and Comparative Physiology **318**(5), R972–R980 (2020).

109. D. Pesta and E. Gnaiger, "High-Resolution Respirometry: OXPHOS Protocols for Human Cells and Permeabilized Fibers from Small Biopsies of Human Muscle," in *Mitochondrial Bioenergetics: Methods and Protocols*, C. M. Palmeira and A. J. Moreno, eds. (Humana Press, 2012), pp. 25–58.

110. B. Glancy, L. M. Hartnell, D. Malide, Z.-X. Yu, C. A. Combs, P. S. Connelly, S. Subramaniam, and R. S. Balaban, "Mitochondrial reticulum for cellular energy distribution in muscle," Nature **523**(7562), 617–620 (2015).

111. R. M. Barbosa, R. M. Santos, C. Pereira, C. F. Lourenço, A. J. Lopes Jesus, C. L. Pereira, C. F. Marques, B. S. Rocha, N. R. Ferreira, A. Ledo, and J. Laranjinha, *Preparation, Standardization and Measurement of Nitric Oxide Solutions Nitrate-Nitrite-NO Pathway View Project Living with Intention, Fullness and Engagement with Inflammatory Bowel Disease: The Impact of a Group Intervention and an ICT-Based Transcultural Intervention on Physical and Mental Health View Project GLOBAL JOURNAL OF ANALYTICAL CHEMISTRY Preparation, Standardization and Measurement of Nitric Oxide Solutions* (2011), **2**(6).

112. R. Tauler, A. Izquierdo-Ridorsa, and E. Casassas, *Simultaneous Analysis of Several Spectroscopic Titrations with Self-Modelling Curve Resolution* (1993), **18**.

113. A. de Juan, J. Jaumot, and R. Tauler, "Multivariate Curve Resolution (MCR). Solving the mixture analysis problem," Analytical Methods **6**(14), 4964–4976 (2014).

114. F. E. Robles, J. W. Wilson, M. C. Fischer, W. S. Warren, T. E. Matthews, J. W. Wilson, S. Degan, M. J. Simpson, J. Y. Jin, J. Y. Zhang, and W. S. Warren, *Image Processing; (180.4315) Nonlinear Microscopy; (300.6420) Spectroscopy, Nonlinear; (190.7110) Ultrafast Nonlinear Optics; (170.3880) Medical and Biological Imaging* (2008), **13**(4).

115. A. Thompson, F. E. Robles, J. W. Wilson, S. Deb, R. Calderbank, and W. S. Warren, "Dual-wavelength pump-probe microscopy analysis of melanin composition," Scientific Reports **6**(October), 36871 (2016).

116. D. Zhang, P. Wang, M. N. Slipchenko, D. Ben-Amotz, A. M. Weiner, and J.-X. Cheng, "Quantitative Vibrational Imaging by Hyperspectral Stimulated Raman Scattering Microscopy and Multivariate Curve Resolution Analysis," Analytical Chemistry **85**(1), 98–106 (2013).

117. I. J. Pence, B. A. Kuzma, M. Brinkmann, T. Hellwig, and C. L. Evans, "Multi-window sparse spectral sampling stimulated Raman scattering microscopy," Biomedical Optics Express **12**(10), 6095–6114 (2021).

118. E. Wang, K. S. Specht, A. J. Chicco, and J. W. Wilson, "High-Repetition-Rate Transient Absorption Spectroscopy of Respiratory Supercomplexes," The Journal of Physical Chemistry B **126**, 1404–1412 (2022).

119. A. E. Yagle, "Regularized Matrix Computations," https://web.eecs.umich.edu/~aey/recent/regular.pdf.

120. W. J. Tomlinson, R. H. Stolen, and C. v Shank, *Compression of Optical Pulses Chirped by Self-Phase Modulation in Fibers* (1984), **1**(2).

121. A. M. Heidt, A. Hartung, G. W. Bosman, P. Krok, E. G. Rohwer, H. Schwoerer, H. Bartelt, J. Herrmann, U. Griebner, N. Zhavoronkov, A. Husakou, D. Nickel, J. C. Knight, W. J. Wadsworth, P. S. J Russell, and G. Korn, *Supercontinuum Generation in Photonic Crystal Fiber* (Cambridge University Press, 2010), **78**(4).

122. A. M. Heidt, J. S. Feehan, J. H. v. Price, and T. Feurer, "Limits of coherent supercontinuum generation in normal dispersion fibers," Journal of the Optical Society of America B **34**(4), 764 (2017).

123. M. Klimczak, B. Siwicki, P. Skibiński, D. Pysz, R. Stępień, A. Heidt, C. Radzewicz, and R. Buczyński, "Coherent supercontinuum generation up to 23 μm in all-solid soft-glass photonic crystal fibers with flat all-normal dispersion," Optics Express **22**(15), 18824 (2014).

124. W. J. Tomlinson, R. H. Stolen, and A. M. Johnson, *Optical Wave Breaking of Pulses in Nonlinear Optical Fibers* (1985), **10**(9).

125. D. Grischkowsky and A. C. Balant, *Optical Pulse Compression Based on Enhanced Frequency Chirping* (n.d.).

126. Govind Agrawal, *Nonlinear Fiber Optics* , 5th ed. (n.d.).

127. Keigo Iizuka, "Modes and Dispersion in Optical Fibers," in *Elements of Photonics* (A John Wiley & Sons, Inc., publication, 2002), **II**.

128. S. Coen, H. G. Randle, T. Sylvestre, and M. Erkintalo, *Modeling of Octave-Spanning Kerr Frequency Combs Using a Generalized Mean-Field Lugiato-Lefever Model* (2007), **38**(1).

129. T. Hansson and S. Wabnitz, "Dynamics of microresonator frequency comb generation: Models and stability," Nanophotonics **5**(2), 231–243 (2016).

130. T. R. Taha and M. J. Ablowitz, *Analytical and Numerical Aspects of Certain Nonlinear Evolution Equations. II. Numerical, Nonlinear Schradinger Equation* (1984), **55**.

131. A. B. Matsko, A. A. Savchenkov, W. Liang, v. S. Ilchenko, D. Seidel, and L. Maleki, "Mode-locked Kerr frequency combs," Optics Letters **36**(15), 2845–2847 (2011).

132. S. G. Leon-Saval, T. A. Birks, W. J. Wadsworth, P. StJ Russell, M. W. Mason, J. K. Ranka, R. S. Windeler, A. J. Stentz, S. Coen, A. Chau, R. Leonhardt, J. D. Harvey, and J. C. Knight, *Supercontinuum Generation in Tapered Fibers* (2000), **25**.

133. A. M. Heidt, *Pulse Preserving Flat-Top Supercontinuum Generation in All-Normal Dispersion Photonic Crystal Fibers* (2010).

134. D. Kopf, H. Tu, J. Lægsgaard, M. Siegel, S. A. Boppart, U. Sharma, and Y. Liu, "Scalar generalized nonlinear Schrödinger equation-quantified continuum generation in an all-normal dispersion photonic crystal fiber for broadband coherent optical sources," Optics Express, Vol. 18, Issue 26, pp. 27872-27884 **18**(26), 27872–27884 (2010).

135. H. Tu, Y. Liu, X. Liu, D. Turchinovich, J. Laegsgaard, S. A. Boppart, H. Tu, Y. Liu, J. Laegsgaard, U. Sharma, M. Siegel, D. Kopf, S. A. Boppart, P. J. Mosley, A. C. Muir, W. J. Wadsworth, and J. C. Knight, "Nonlinear polarization dynamics in a weakly birefringent

all-normal dispersion photonic crystal fiber: toward a practical coherent fiber supercontinuum laser," Express **18**(26), 27872–27884 (2010).

136. H. Tu, Y. Liu, D. Turchinovich, M. Marjanovic, J. K. Lyngsø, J. Lægsgaard, E. J. Chaney, Y. Zhao, S. You, W. L. Wilson, B. Xu, M. Dantus, and S. A. Boppart, "Stain-free histopathology by programmable supercontinuum pulses," Nature Photonics **10**(8), 534–540 (2016).

137. Y. Liu, H. Tu, and S. A. Boppart, *Wave-Breaking-Extended Fiber Supercontinuum Generation for High Compression Ratio Transform-Limited Pulse Compression* (2012).

138. H. Tu and S. A. Boppart, "Coherent fiber supercontinuum for biophotonics," Laser and Photonics Reviews **7**(5), 628–645 (2013).

139. H. Tu, Y. Liu, X. Liu, D. Turchinovich, J. Laegsgaard, S. A. Boppart, H. Tu, Y. Liu, J. Laegsgaard, U. Sharma, M. Siegel, D. Kopf, S. A. Boppart, P. J. Mosley, A. C. Muir, W. J. Wadsworth, and J. C. Knight, "Nonlinear polarization dynamics in a weakly birefringent all-normal dispersion photonic crystal fiber: toward a practical coherent fiber supercontinuum laser," Express **18**(26), 27872–27884 (2010).

140. Y. Jung, B. H. Lee, and K. Oh, *Tunable Bandpass Filter Using the Short-and Long-Wavelength Bend Loss Edges of a Hollow Optical Fiber and a Micro-Structured Optical Fiber ICMAT 2007 Symposium on Microstructured and Nanostructured Optical Fibers* (n.d.).

141. A. M. Heidt, A. Hartung, G. W. Bosman, P. Krok, E. G. Rohwer, H. Schwoerer, H. Bartelt, J. Herrmann, U. Griebner, N. Zhavoronkov, A. Husakou, D. Nickel, J. C. Knight, W. J.

Wadsworth, P. S. J Russell, and G. Korn, *Supercontinuum Generation in Photonic Crystal Fiber* (Cambridge University Press, 2010), **78**(4).

142. A. M. Heidt, *Pulse Preserving Flat-Top Supercontinuum Generation in All-Normal Dispersion Photonic Crystal Fibers* (2010).

143. Y. Arosa and R. de la Fuente, "Refractive index spectroscopy and material dispersion in fused silica glass," Optics Letters **45**(15), 4268 (2020).

144. E. B. Treacy, "Optical Pulse Compression with Diffraction Gratings," IEEE Journal of Quantum Electronics **5**(9), 454–458 (1969).

145. E. Martinez, J. P. Gordon, and R. L. Fork, *Negative Group-Velocity Dispersion Using Refraction* (1984), **1**(10).

146. O. E. Martínez, "Matrix Formalism for Pulse Compressors," IEEE Journal of Quantum Electronics **24**(12), 2530–2536 (1988).

147. H. Kogelnik and T. Li, *Laser Beams and Resonators* (n.d.).

148. A. E. Siegman, *Lasers* (University Science, 1986).

149. C. Froehly, B. Colombeau, and M. Vampouille, *E. WOLF, PROGRESS IN OPTICS XX @ NORTH-HOLLAND 1983 SHAPING AND ANALYSIS OF PICOSECOND LIGHT PULSES* (n.d.).

150. A. Lombardini, V. Mytskaniuk, S. Sivankutty, E. R. Andresen, X. Chen, J. Wenger, M. Fabert, N. Joly, F. Louradour, A. Kudlinski, and H. Rigneault, "High-resolution multimodal flexible coherent Raman endoscope article," Light: Science and Applications **7**(1), (2018).

151. M. Balu, G. Liu, Z. Chen, B. J. Tromberg, E. O. Potma, F. Henry, D. Côté, M. A. Randolph, E. A. Z Rust, R. W. Redmond, I. E. Kochevar, C. P. Lin, and J. M. Wino, *Laser Microbeam and Medical Program (LAMMP), Beckman Laser Institute and Medical Clinic, 1002 Health Sciences Road East* (2010).

152. M. Minsky, "Memoir on inventing the confocal scanning microscope," SCANNING **10**, 128–138 (1988).

153. v. Wilke, "Optical scanning microscopy—The laser scan microscope," SCANNING **7**, 88–96 (1985).

154. J. G. White, W. B. Amos, and M. Fordham, *An Evaluation of Confocal Versus Conventional Imaging of Biological Structures by Fluorescence Light Microscopy* (n.d.).

155. X. Zhang, C. Duan, L. Liu, X. Li, and H. Xie, "A non-resonant fiber scanner based on an electrothermally-actuated MEMS stage," Sensors and Actuators, A: Physical **233**, 239–245 (2015).

156. X. Zhang, L. Zhou, and H. Xie, "A large range micro-XZ-stage with monolithic integration of electrothermal bimorph actuators and electrostatic comb drives," in *Proceedings of the IEEE International Conference on Micro Electro Mechanical Systems (MEMS)* (Institute of Electrical and Electronics Engineers Inc., 2016), **2016-February**, pp. 71–74.

157. H.-C. Park, X. Zhang, W. Yuan, L. Zhou, H. Xie, and X. Li, "Ultralow-voltage electrothermal MEMS based fiber-optic scanning probe for forward-viewing endoscopic OCT," Optics Letters **44**(9), 2232 (2019).

158. C. M. Lee, C. J. Engelbrecht, T. D. Soper, F. Helmchen, and E. J. Seibel, "Scanning fiber endoscopy with highly flexible, 1 mm catheterscopes for wide-field, full-color imaging," Journal of Biophotonics **3**(5–6), 385–407 (2010).

159. E. J. Seibel and Q. Y. J. Smithwick, "Unique features of optical scanning, single fiber endoscopy," Lasers in Surgery and Medicine **30**(3), 177–183 (2002).

160. L. E. Kinsler, A. R. Frey, A. B. Coppens, and J. V. Sanders, *Fundamentals of Acoustics*, 3rd ed. (1982).

161. X. Liu, M. J. Cobb, Y. Chen, M. B. Kimmey, and X. Li, *Rapid-Scanning Forward-Imaging Miniature Endoscope for Real-Time Optical Coherence Tomography* (2004), **29**(15).

162. R. van Beers, B. Aernouts, M. M. Reis, and W. Saeys, "Anisotropic light propagation in bovine muscle tissue depends on the initial fiber orientation, muscle type and wavelength," Optics Express **25**(18), 22082 (2017).

163. A. Currà, R. Gasbarrone, A. Cardillo, F. Fattapposta, P. Missori, L. Marinelli, G. Bonifazi, S. Serranti, and C. Trompetto, "In vivo non-invasive near-infrared spectroscopy distinguishes normal, post-stroke, and botulinum toxin treated human muscles," Scientific Reports **11**(1), (2021).

164. W. F. Cheong, S. A. Prahl, and A. J. Welch, "A Review of the Optical Properties of Biological Tissues," IEEE Journal of Quantum Electronics **26**(12), 2166–2185 (1990).

165. "Evolution of Flat, PC, UPC and APC Fiber Connectors," .

166. N. Zhang, T.-H. Tsai, O. O. Ahsen, K. Liang, H.-C. Lee, P. Xue, X. Li, and J. G. Fujimoto, "Compact piezoelectric transducer fiber scanning probe for optical coherence tomography," Optics Letters **39**(2), 186 (2014).

167. H.-J. Shin, M. C. Pierce, D. Lee, H. Ra, O. Solgaard, R. Richards-Kortum, W. M. Petroll, A. Boyde, L. Martin, P. Corcuff, J. L. Leveque, M. A. Lemp, H. D. Cavanagh, and J. v Jester, *Fiber-Optic Confocal Microscope Using a MEMS Scanner and Miniature Objective Lens* (2007).

168. L. Liu, E. Wang, X. Zhang, W. Liang, X. Li, and H. Xie, "MEMS-based 3D confocal scanning microendoscope using MEMS scanners for both lateral and axial scan," Sensors and Actuators, A: Physical **215**, 89–95 (2014).

169. P. M. Lane, *Terminal Reflections in Fiber-Optic Image Guides* (2009).

170. C. Liang, M. R. Descour, K.-B. Sung, and R. Richards-Kortum, *Fiber Confocal Reflectance Microscope (FCRM) for in-Vivo Imaging* (2001).

171. Y. Jiang, Y. Gong, J. H. Rubenstein, T. D. Wang, and E. J. Seibel, "Toward real-time quantification of fluorescence molecular probes using target/background ratio for guiding biopsy and endoscopic therapy of esophageal neoplasia," Journal of Medical Imaging **4**(02), 1 (2017).

172. M. N. Slipchenko, R. A. Oglesbee, D. Zhang, W. Wu, and J. X. Cheng, "Heterodyne detected nonlinear optical imaging in a lock-in free manner," Journal of Biophotonics **5**(10), 801–807 (2012).

173. M. A. Taylor and W. P. Bowen, "Quantum metrology and its application in biology," Physics Reports **615**, 1–59 (2016).

174. C. A. Casacio, L. S. Madsen, A. Terrasson, M. Waleed, K. Barnscheidt, B. Hage, M. A. Taylor, and W. P. Bowen, "Quantum-enhanced nonlinear microscopy," Nature **594**(7862), 201–206 (2021).

175. M. A. Taylor and W. P. Bowen, "Quantum metrology and its application in biology," Physics Reports **615**, 1–59 (2016).

176. D. F. Walls, *Squeezed States of Light* (1983).

177. M. J. Rust, M. Bates, and X. Zhuang, "Sub-diffraction-limit imaging by stochastic optical reconstruction microscopy (STORM)," Nature Methods **3**(10), 793–795 (2006).

178. S. W. Hell and J. Wichmann, *Breaking the Diffraction Resolution Limit by Stimulated Emission: Stimulated-Emission-Depletion Fluorescence Microscopy* (1994), **19**(11).

179. M. Heilemann, S. van de Linde, M. Schüttpelz, R. Kasper, B. Seefeldt, A. Mukherjee, P. Tinnefeld, and M. Sauer, "Subdiffraction-resolution fluorescence imaging with conventional fluorescent probes," Angewandte Chemie - International Edition **47**(33), 6172–6176 (2008).

180. Eric Betzig, George H. Patterson, Rachid Sougrat, O. Wolf Lindwasser, Scott Olenych, Juan S. Bonifacino, Michael W. Davidson, Jennifer Lippincott-Schwartz, and Harald F. Hess, "Imaging Intracellular Fluorescent Proteins at Nanometer Resolution," Science (1979) **313**(5793), (2006).

181. P. Wang, M. N. Slipchenko, J. Mitchell, C. Yang, E. O. Potma, X. Xu, and J. X. Cheng, "Far-field imaging of non-fluorescent species with subdiffraction resolution," Nature Photonics **7**(6), 449–453 (2013).

182. C. Lee, E. Z. Xu, Y. Liu, A. Teitelboim, K. Yao, A. Fernandez-Bravo, A. M. Kotulska, S. H. Nam, Y. D. Suh, A. Bednarkiewicz, B. E. Cohen, E. M. Chan, and P. J. Schuck, "Giant nonlinear optical responses from photon-avalanching nanoparticles," Nature **589**(7841), 230–235 (2021).

183. E. S. Levy, C. A. Tajon, T. S. Bischof, J. Iafrati, A. Fernandez-Bravo, D. J. Garfield, M. Chamanzar, M. M. Maharbiz, V. S. Sohal, P. J. Schuck, B. E. Cohen, and E. M. Chan, "Energy-Looping Nanoparticles: Harnessing Excited-State Absorption for Deep-Tissue Imaging," ACS Nano **10**(9), 8423–8433 (2016).

184. D. Denkova, M. Ploschner, M. Das, L. M. Parker, X. Zheng, Y. Lu, A. Orth, N. H. Packer, and J. A. Piper, "3D sub-diffraction imaging in a conventional confocal configuration by exploiting super-linear emitters," Nature Communications **10**(1), (2019).

185. A. Bednarkiewicz, E. M. Chan, A. Kotulska, L. Marciniak, and K. Prorok, "Photon avalanche in lanthanide doped nanoparticles for biomedical applications: Super-resolution imaging," Nanoscale Horizons **4**(4), 881–889 (2019).

186. J. J. Field, K. A. Wernsing, S. R. Domingue, A. M. A. Motz, K. F. DeLuca, D. H. Levi, J. G. DeLuc, M. D. Young, J. A. Squier, and R. A. Bartels, "Superresolved multiphoton microscopy with spatial frequency-modulated imaging," Proc Natl Acad Sci U S A **113**(24), 6605–6610 (2016).

187. H. Kim, Y.-H. Seo, J. Jeon, and K.-H. Jeong, "Lissajous scanning structured illumination microscopy," Biomedical Optics Express **11**(10), 5575 (2020).

188. I. J. Pence, B. A. Kuzma, M. Brinkmann, T. Hellwig, and C. L. Evans, "Multi-window sparse spectral sampling stimulated Raman scattering microscopy," Biomedical Optics Express **12**(10), 6095 (2021).

189. D. Zhang, P. Wang, M. N. Slipchenko, D. Ben-Amotz, A. M. Weiner, and J. X. Cheng, "Quantitative vibrational imaging by hyperspectral stimulated raman scattering microscopy and multivariate curve resolution analysis," Analytical Chemistry **85**(1), 98–106 (2013).

190. R. Trebino, K. W. DeLong, D. N. Fittinghoff, J. N. Sweetser, M. A. Krumbügel, B. A. Richman, and D. J. Kane, "Measuring ultrashort laser pulses in the time-frequency domain using frequency-resolved optical gating," Review of Scientific Instruments **68**(9), 3277–3295 (1997).

191. R. Gerchberg and W. Saxton, "A Practical Algorithm for the Determination of Phase from Image and Diffraction Plane Pictures," Optik **35**, 237–246 (1972).

192. Q. v Le, A. Karpenko, J. Ngiam, and A. Y. Ng, *ICA with Reconstruction Cost for Efficient Overcomplete Feature Learning* (n.d.).

Appendices

A.1 Adaptive filter

This section is a reformatted and version of content I previously published in *Journal of Biomedical Optics*[59].

The pump-probe signal of the setup in Chapter 5 is at 1 MHz. The sample structural information is carried within a specific bandwidth centered at 1MHz, which is extracted by a lock-in amplifier (LIA). However, the laser RIN buried within the bandwidth degrade the SNR. Moreover, the signal amplitude is only 10^{-5} to 10^{-6} of the DC offset. Thus, the adaptive filter is needed to suppress the laser RIN within the lock-in band. After the adaptive filter, we apply an LIA algorithm to extract the 1MHz signal, which is used to reconstruct the transient absorption image.

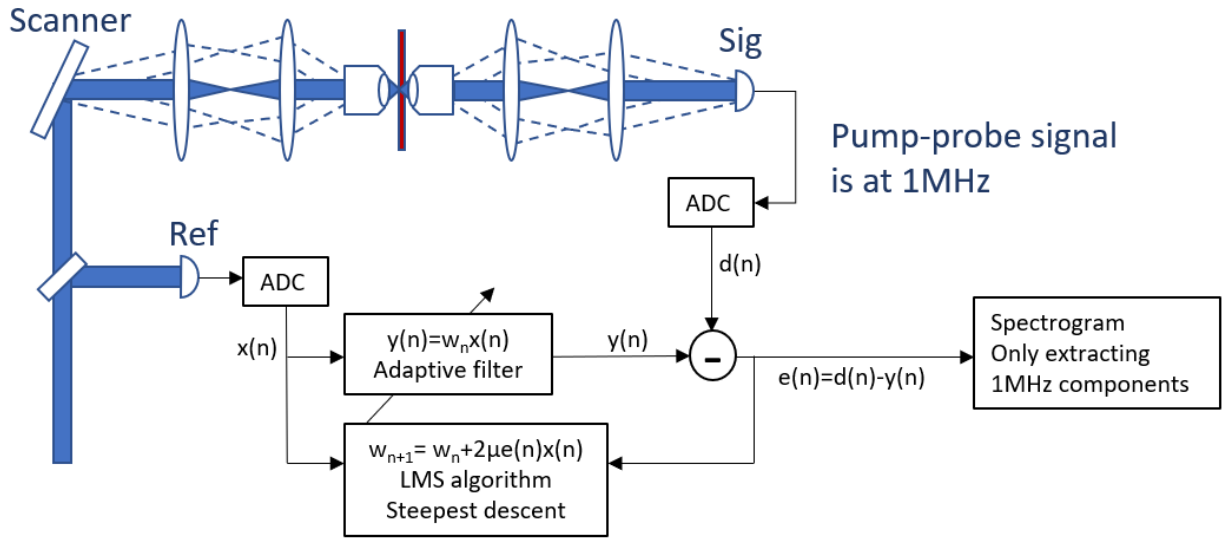

Figure A.1: experimental setup and block diagram of adaptive filter.

The adaptive filter is a finite impulse response (FIR) filter. The experimental setup and the block diagram of the adaptive filter are shown in Figure A.1. The adaptive filter consists of two ADC channels to digitize the signal and reference arm respectively. The signal arm detects the probe beam that scans through the sample. Thus, the time-discrete probe signal data, $d[n]$, contains a DC offset constant, the laser RIN, $\sigma_{\mathrm{RIN}}[n]$, the white electronic noise, $\sigma_{es}[n]$, the 1MHz pump-probe signal, $s[n]$, and the transmitted intensity variation, $T[n]$, due to the sample structures. The reference arm detects the probe beam before passing through the sample. So the reference, $x[n]$, contains a constant DC offset, the laser RIN noise $\sigma_{\mathrm{RIN}}[n]$, and the white electronic noise $\sigma_{er}[n]$. The adaptive filter can cancel the correlated laser RIN between the probe and reference. However, the electronic noise in these arms are not correlated, and therefore, they cannot be canceled.

The basic structure of the current software-based adaptive filter is a multiple-tap FIR filter. The noise estimation, y(n), can be expressed by

$$y[n] = \sum_{i=0}^{N-1} w_n[i]x[n-i] = w_n[0]x[n] + w_n[1]x[n-1] + \cdots + w_n[N-1]x[n-N+1] \quad (\mathrm{A.1})$$

where $x[n-i]$ is the $n-i^{\mathrm{th}}$ data point measured from the reference ADC, $w_n[i]$ is the weight applied to$x[n-i]$, $y[n]$ is the n^{th} noise estimation. Equation appx 1. states that the n^{th} noise estimation is the sum of previous *N* reference input data points, $x[n-N+1]$ to $x[\mathrm{n}]$, scaled by weight, $w_n[0]$ to $w_n[N-1]$. The weight vector or the filter adjustable coefficient w_{n+1} is derived based on the LMS algorithm,

$$w_{n+1}[i] = w_n[\mathrm{i}] + 2\mu \times e[n]x[n-i] \quad (\mathrm{A.2})$$

$$e[n] = d[n] - y[n] \qquad (\mathrm{A.3})$$

where μ controls convergence speed and N is the filter length. The filter coefficient w_n is a one-dimensional vector whose size equals the filter length. In our experiment, we set $N = 16$. The weight vector w_0 can be randomly chosen at the start, or set to zero. We then take the difference between the sum-of-products, y, and the first 16 element of d to form the error vector e. At the beginning of the next cycle of adaption, a new set of the 16-element weight vector is generated through the feedback determined by the initial error vector (Eqn. A.2). Then, for both x and d, we shift the window on the data sample to the right by one pixel, to get another set of 16-element x and d, then go through another cycle of adaption. After several cycles of adaption, the error output will have a mean value of zero and a minimum std., meaning the laser RIN carried inside the $e[n]$ is minimized. In our case, the adaptive filter converged after 33 cycles.

A.2 Lock-in amplifier (LIA)

This section is a reformatted and version of content I previously published in *Journal of Biomedical Optics* [59].

After being cleaned by the adaptive filter, a LIA algorithm down-converts the signal to DC and the structural information to the sideband centered at DC. In the process, the original DC component and residual $1/f$ noise are up-converted to the 1MHz region. Then a CIC filter is built as a lowpass filter to attenuate the region centered at 1MHz and pass the downsampled low-frequency signal components. The cutoff frequency can be tuned by adjusting the parameters of the digital filter. The maximum cutoff frequency f_c should be selected at the pixel Nyquist frequency f_s according to $f_c = f_s/2$. But in our case, the selected passband cutoff is much lower than the maximum f_c just to lower the accumulated noise within the passband.

The following equations can describe the principle of an LIA:

$$s(t) \times \cos(\omega t) \times \cos(\omega t) = \frac{1}{2} s(t)[\cos(2\omega t) + \cos(0 \times t)] \quad (A.4)$$

$$\mathrm{DC} \times \cos(0 \times t) \times \cos(\omega t) = \mathrm{DC} \times \cos(\omega t) \quad (A.5)$$

The precondition for the above equation set is to assume the signal takes the form of the product of the signal amplitude, $s(t)$, and a cosine wave with a certain frequency ω. For convenience, the 1/*f* noise is neglected here. Equation A.4 states that multiplying the acquired signal by a cosine with frequency of ω will produce two terms, a second harmonic and a DC term. The amplitudes of both terms are equal to one-half of the original signal amplitude. The low-pass filter then passes the DC term, which is proportional to $s(t)$. Equation A.5 shows that, after multiplying by a cosine, the original DC component is upconverted to a frequency range centered at ω and rejected by the low-pass filter.

A.3 Split-step Fourier method

The split-step Fourier method specifically solves the NLSE, which is a partial differential equation that does not always have an analytic solution. We can firstly use the linear operator $\widehat{D}$ and nonlinear operator $\widehat{N}$ to rewrite the NLSE:

$$\frac{\partial A}{\partial z} = \left(\widehat{D} + \widehat{N}\right)A \quad (A.6)$$

Where A is the slowly carrying envelope representing the pulse shape along the propagation direction z. the operator $\widehat{D}$ accounts for linear dispersion and loss, $\widehat{N}$ accounts for nonlinear dispersion, such as SPM, self-steepening, and Raman scattering. These two operators have the following forms:

$$\widehat{D} = -\frac{i\beta_2}{2}\frac{\partial^2}{\partial T^2} + \frac{\beta_3}{6}\frac{\partial^3}{\partial T^3} - \frac{\alpha}{2} \quad (A.6)$$

$$\widehat{N} = i\gamma\left(|A|^2 + \frac{i}{\omega_0}\frac{1}{A}\frac{\partial}{\partial T}(|A|^2 A) - T_R\frac{\partial|A|^2}{\partial T}\right) \quad \text{(A. 7)}$$

The basic idea of the method is to discretize the continuous NLSE, so the NLSE's solution would have the following form:

$$A(z+h,T) \approx \exp\left(h\widehat{D}\right)\exp\left(h\widehat{N}\right)A(z,T) \quad \text{(A. 8)}$$

The discretion solution states that the dispersion and the nonlinearity act independently over a small propagation distance, h, inside the fiber. Suppose we focus on solving the output pulse of an input pulse initially at z and propagate for a very small distance of h in a nonlinear medium. This is done in two steps. Firstly, the pulse propagates for a distance of h in a purely linear medium. Secondly, pulse propagates in a pure nonlinear medium for the same distance. The above two steps are equivalent to introducing two temporal phases, $h\widehat{D}$ and $h\widehat{N}$, due to linearity and nonlinearity, respectively.

Even though the NLSE is greatly simplified after the discretization, solving the two temporal phases is still not straightforward. Because the partial derivatives with respect to T are present in both $\widehat{D}$ and $\widehat{N}$. Luckily, based on the Fourier transform properties, derivatives with respect to T can be transformed into simple products. For instance, $\frac{\partial^2}{\partial T^2} \rightarrow (i\omega)^2$

$$\begin{aligned} A(z+h,\omega) \approx \exp&\left[h\left(-\frac{i\beta_2}{2}(i\omega)^2 + \frac{\beta_3}{6}(i\omega)^3 - \frac{\alpha}{2}\right)\right] \\ &\times \exp\left[h \times i\gamma\left(|A|^2 + \frac{i}{\omega_0}\frac{1}{A}(i\omega)(|A|^2A) - T_R(i\omega)|A|^2\right)\right] \\ &\times A(z,\omega) \end{aligned} \quad \text{(A. 9)}$$

If M segments of such distance h compose the total nonlinear fiber length, we can multiply M in successive steps together to achieve the output pulse from the entire fiber with length of $L = M\ h$:

$$A(L,\omega) \approx \prod_{m=1}^{M} \left\{ \exp\left[h\left(-\frac{i\beta_2}{2}(i\omega)^2 + \frac{\beta_3}{6}(i\omega)^3 - \frac{\alpha}{2} \right) \right] \right.$$
$$\left. \times \exp\left[h \times i\gamma \left(|A|^2 + \frac{i}{\omega_0}\frac{1}{A}(i\omega)(|A|^2 A) - T_R(i\omega)|A|^2 \right) \right] \right\} \times A(z,\omega) \qquad (A.10)$$

A.4 Multivariate curve resolution (MCR)

This section is a reformatted and version of content I previously published in *Journal of Physical Chemistry B* [63].

We noticed that multiple Raman microscopy research groups have already demonstrated that MCR works best if the a priori knowledge of Raman spectra of pure compounds exists[188,189]. Here we apply MCR to unmixing TA signals. The MCR-ALS algorithm,[76] which we note has parallels to iterative phase retrieval algorithms used in optics,[190,191] alternates between the estimation of the underlying coefficients and the concentrations, alternately enforcing constraints to match the known dye measurement and the assumption of nonzero mixing coefficients:

1. Let the first row of X, x_1, be the known dye response and the second row, x_2, be a randomly initialized guess at the heme component.

2. Estimate the mixing matrix using the Moore-Penrose pseudoinverse: $\widehat{M} = Y\ X^{+}$.

3. Enforce the non-negativity constraint on the mixing matrix by setting all negative elements of $\widehat{M}$ to zero.

4. Estimate the sources by unmixing the measurements: $X = \widehat{M}^{+}\ Y$.

5. Replace x_1 with the known dye response.

6. Repeat steps 2−5 until convergence.

In practice, this converges within ten iterations. We simulated random mixtures of heme and dyed TA signals and compared the results with conventional ICA, specifically reconstruction ICA[192] using MATLAB's `rica()` function to validate our modified approach. We varied the maximum fraction of dye contribution to the mixture and the amount of added noise for each case. For the sake of these simulations, the dye signal was taken from a single measurement, and the heme signal was taken from the average of all TA spectra from the respiratory chain gels. MCR was run for 100 iterations for each case and was restarted if a NaN was detected in the mixing matrix. ICA was run repeatedly for each case until it yielded a heme component with the correct sign. The results are shown in Figure A.2. For relatively small concentrations of the dye, both MCR and ICA produce similar results. But in cases where the dye signal is strong enough to alter the overall decay time of the mixture, MCR and ICA converge, with MCR producing more reliable estimates of the heme signal.

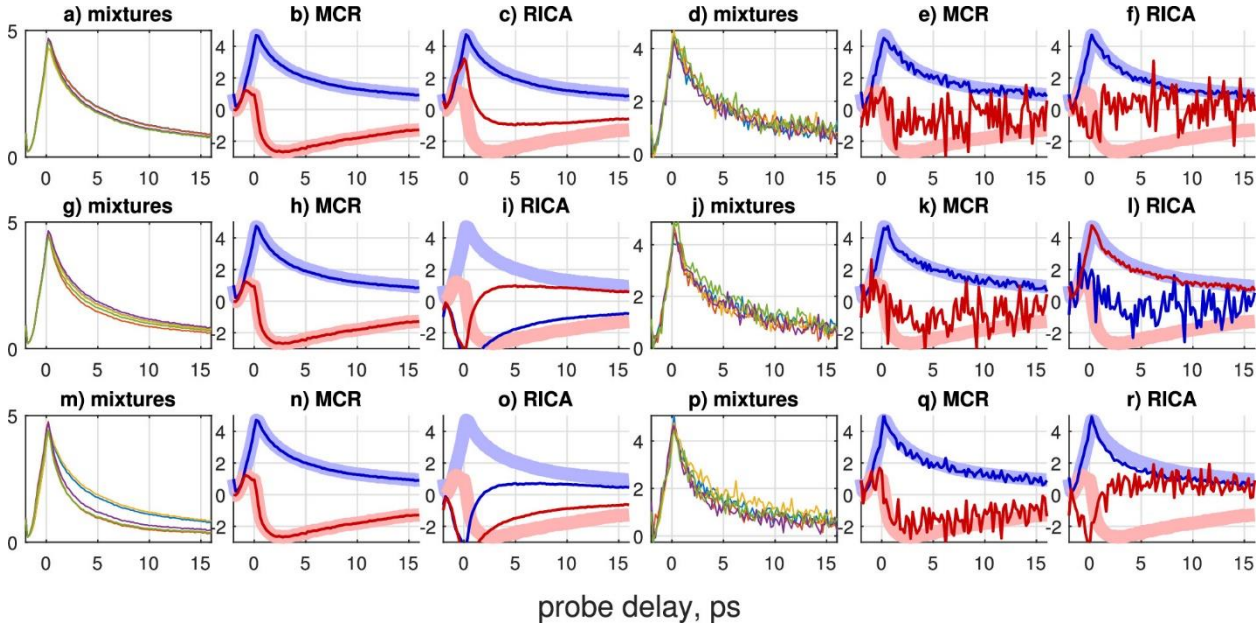

Figure A.2: MCR and RICA two-source recovery for synthetic mixtures of heme and dye signals. For each case, the left panel shows synthetic mixtures, and the center panel shows MCR recovered components, and the right panel shows RICA recovered components. The recovered heme signal is shown as thin blue lines, and the recovered dye signal is shown as thin red lines. The corresponding ground truth is shown as light-shaded thick lines. (a) Artificial mixtures, (b) MCR-recovered components, and (c) RICA-recovered components for a maximum 10% dye signal, with no noise. (d–f) Same as above, for a maximum 20% dye signal, no noise. (g–i) Same as above, for maximum 50% dye signal, no noise. (j–l) Same as above, maximum 10% dye signal, 20% additive white Gaussian noise. (m–o) Same as above, for a maximum 20% dye signal. (p–r) Same as above, for a maximum 50% dye signal, 20% additive white Gaussian noise